

**ISTANBUL TECHNICAL UNIVERSITY ★ GRADUATE SCHOOL OF SCIENCE**  
**ENGINEERING AND TECHNOLOGY**

**COMPRESSIVE STRENGTH  
AND CHARACTERISATION OF ADDITIVELY  
MANUFACTURED DOUBLE GYROID LATTICE STRUCTURES**



**M.Sc. THESIS**

**Bariş KAVAS**

**Department of Metallurgical and Materials Engineering**

**Materials Engineering Programme**

**JUNE 2019**



**ISTANBUL TECHNICAL UNIVERSITY ★ GRADUATE SCHOOL OF SCIENCE**  
**ENGINEERING AND TECHNOLOGY**

**COMPRESSIVE STRENGTH  
AND CHARACTERISATION OF ADDITIVELY  
MANUFACTURED DOUBLE GYROID LATTICE STRUCTURES**



**M.Sc. THESIS**

**Bariř KAVAS**  
**(506151431)**

**Department of Metallurgical and Materials Engineering**  
**Materials Engineering Programme**

**Thesis Advisor: Dr. řeref Sönmez**  
**Thesis Co-Advisor: Dr. Evren Yasa**

**JUNE 2019**



**İSTANBUL TEKNİK ÜNİVERSİTESİ ★ FEN BİLİMLERİ ENSTİTÜSÜ**

**KATMANLI İMALAT İLE ÜRETİLMİŞ ÇİFT GYROID KAFES YAPISININ  
BASMA DAYANIMI VE KARAKTERİZASYONU**



**YÜKSEK LİSANS TEZİ**

**Barış KAVAS  
(506151431)**

**Metalurji ve Malzeme Mühendisliği Anabilim Dalı**

**Malzeme Mühendisliği Programı**

**Tez Danışmanı: Dr. Şeref SÖNMEZ  
Eş Danışman: Dr. Evren YASA**

**HAZİRAN 2019**



Barış Kavas, a M.Sc. student of İTÜ Graduate School of Science Engineering and Technology student ID 506151431, successfully defended the thesis entitled “Mechanical Behavior and Characterization of Additively Manufactured Double Gyroid Lattice Structures”, which he prepared after fulfilling the requirements specified in the associated legislations, before the jury whose signatures are below.

**Thesis Advisor:**      **Dr. Şeref SÖNMEZ**      .....

Istanbul Technical University

**Co-advisor:**      **Dr. Evren YASA**      .....

Eskişehir Osmangazi University

**Jury Members:**      **Prof. Dr. Hüseyin Çimenoğlu**      .....

Istanbul Technical University

**Prof. Dr. İsmail Lazoğlu**      .....

Koç University

**Dr. Cevat Fahir Arısoy**      .....

Istanbul Technical University

**Date of Submission: 02.05.2019**

**Date of Defense: 11.06.2019**





*Felix, qui potuit rerum cognoscere causas*



## FOREWORD

First of all, I would like to express my sincere gratitude to my advisor Dr. Şeref Sönmez and my co-advisor Dr. Evren Yasa for their endless support and guidance.

Secondly, I would like to thank to my manager Onur Önder for his support through all of the study, my colleagues Banu Berme and Onur Tazegül for their assistance for characterization and testing of the specimens, to Dr. Erdem Kundakçioğlu for his guidance, to Murat Erdim, Emre Aytan and Birol Turan for teaching me the necessary details of computer aided design and measurement, to Ozan Emre for his assistance in micro-scanning, to Hakan Yılmaz and Menderes Sayarsoy for their hands on support, to Bora İşlier for his guidance and friendship and to Alessandro Stanca for encouraging me to work with triply periodic minimal surfaces.

Furthermore, I want to thank to my friends İdil Özcan, Barış Akok and Zeynep Oğuzhan, who have assisted me many hours during the completion of this thesis, to Furkan Dodurka for always being there to help me out whenever I get into trouble with numbers and to Dilşad Dağtekin for her constant encouragement for my academic endeavors.

Very special thanks to Prof. Dr. Allan Schoen, who have inspired and encouraged many scientists and engineers around the world including myself by passionately discovering and enthusiastically introducing the gyroid surface model to literature.

Finally, I would like to express my utter gratitude to my father Ömer Kavas and my mother Lütfiye Kavas for raising me patiently and lovingly to be a curious person and my brother Berkay Kavas for his guidance through my life.

This study was carried out using TUBITAK Technology and Innovation Support Program.

June 2019

Barış Kavas

Metallurgical & Materials Engineer



## TABLE OF CONTENTS

<b>FOREWORD</b> .....	<b>ix</b>
<b>TABLE OF CONTENTS</b> .....	<b>xi</b>
<b>ABBREVIATIONS</b> .....	<b>xiii</b>
<b>SYMBOLS</b> .....	<b>xv</b>
<b>LIST OF TABLES</b> .....	<b>xvii</b>
<b>LIST OF FIGURES</b> .....	<b>xix</b>
<b>1.INTRODUCTION</b> .....	<b>1</b>
1.1 Additive Manufacturing .....	1
1.2 Cellular Structures.....	3
1.3 Triply Periodic Minimal Surfaces .....	9
1.4 Haynes 188.....	14
1.5 Problem Statement .....	17
<b>2.EXPERIMENTAL SETUP AND CHARACTERIZATION</b> .....	<b>19</b>
2.1 Modelling and Build File Preparation.....	20
2.2 Additive Manufacturing and Preperation of Specimens .....	21
2.2.1 Direct metal laser melting .....	21
2.2.2 Preperation of specimens .....	22
2.3 Characterization .....	24
2.3.1 Compression test .....	25
2.3.2 Stereo microscope .....	26
2.3.3 Inverted microscope .....	26
2.3.3.1 Microstructure.....	27
2.3.3.2 Porosity .....	27
2.3.4 Optical 3D micro measurement .....	28
2.3.5 Scanning electron microscope.....	29
<b>3.EXPERIMENTAL PROCEDURE</b> .....	<b>31</b>
3.1 Design of Experimental Work .....	31
3.1.1 Specimen design.....	31
3.1.1.1 Preliminary modeling trial basic surface modeling .....	32
3.1.1.2 The second modeling trial based on mathematical surface definition .....	34
3.1.2 Manufacturing of specimens .....	37
3.2 Compression Testing.....	42
<b>4.RESULTS AND DISCUSSIONS</b> .....	<b>43</b>
4.1 Microstructure .....	43
4.1.1 3mm unit cell size .....	43
4.1.2 4 mm unit cell size .....	45

4.1.3	6 mm unit cell size .....	49
4.1.4	8 mm unit cell size .....	51
4.1.5	12 mm unit cell size .....	54
4.2	Surface Topology and Quality .....	56
4.2.1	3 mm unit cell specimen.....	58
4.2.2	4 mm unit cell specimen.....	58
4.2.3	6 mm unit cell specimen.....	59
4.2.4	8 mm unit cell specimen.....	61
4.2.5	12 mm unit cell.....	63
4.3	Compression Testing.....	67
<b>5.</b>	<b>CONCLUSION.....</b>	<b>79</b>
	<b>REFERENCES .....</b>	<b>83</b>
	<b>CURRICULUM VITAE.....</b>	<b>91</b>

## **ABBREVIATIONS**

<b>AM</b>	: Additive Manufacturing
<b>CAD</b>	: Computer Aided Design
<b>DMLM</b>	: Direct Metal Laser Melting
<b>DG</b>	: Double Gyroid
<b>HS188</b>	: Haynes 188 <sup>®</sup>
<b>SEM</b>	: Scanning Electron Microscope
<b>TPMS</b>	: Triply Periodic Minimal Surface



## SYMBOLS

<b>W</b>	: Absorbed energy by the specimens under compression
<b>W<sub>v</sub></b>	: Normalized absorbed energy under compression
<b>V<sub>latt</sub></b>	: Volume of the solid in lattice specimen
<b>E<sub>latt</sub></b>	: Modulus of elasticity of the lattice structure
<b>E<sub>sol</sub></b>	: Modulus of elasticity of the solid material used in lattice structure
<b>ρ<sub>latt</sub></b>	: Density the lattice structure
<b>ρ<sub>sol</sub></b>	: Density of the solid used in lattice structure
<b>σ<sub>pl. latt</sub></b>	: Plateau stress of the lattice structure
<b>σ<sub>y. sol</sub></b>	: Yield stress of the material used in lattice structure
<b>C<sub>1</sub></b>	: Empirical coefficient for modulus of elasticity comparison of lattice structures
<b>C<sub>5</sub></b>	: Empirical coefficient for the yield stress comparison of lattice structures
<b>n</b>	: Empirical coefficient for the modulus of elasticity comparison
<b>m</b>	: Empirical coefficient for the yield stress comparison of lattice structures



## LIST OF TABLES

<b>Table 1</b> : Chemical composition of HS188 .....	<b>15</b>
<b>Table 3.1</b> : Theoretical specimen values .....	<b>38</b>
<b>Table 3.2</b> : Measured first manufactured specimen values .....	<b>39</b>
<b>Table 3.3</b> : Final specimen values from CAD model and measured after manufacturing .....	<b>40</b>
<b>Table 4.1</b> : Strain and energy absorption values for 6, 8 and 12 mm specimens .....	<b>71</b>
<b>Table 4.2</b> : Yield stress and Modulus of elasticity for each unit cell size specimen.	<b>77</b>
<b>Table 4.3</b> : C1 and C5 values .....	<b>78</b>





## LIST OF FIGURES

	<u>Page</u>
<b>Figure 1.1</b> : Powder bed additive manufacturing (Farid et al., n.d.).....	2
<b>Figure 1.2</b> : Cellular structure examples(Gibson, L. J., Ashby, 1997). .....	4
<b>Figure 1.3</b> : a) open cell foam b) closed cell foam c) strut lattice structure d) honeycomb lattice structure(H. N.G. Wadley et al., 2010).....	5
<b>Figure 1.4</b> : Truss lattice unit cell type examples a) BCC b) BCCz c) FCC d) FBCC e) S-FCC f) S-FCCz g) S-FBCC h) S-FBCCz (Panesar, Abdi, Hickman, & Ashcroft, 2018) .....	7
<b>Figure 1.5</b> : Heat exchanger application example for lattice structures (Haydn N.G. Wadley & Queheillalt, 2009) .....	8
<b>Figure 1.6</b> : Soap film is the most common example of minimal surfaces.....	10
<b>Figure 1.7</b> : Diamond TPMS structured shell of Lamprocyphus augustus.....	11
<b>Figure 1.8</b> : Teinopalpus imperialis with gyroid-like layer on their wings to reflect green light only. ....	11
<b>Figure 1.9</b> : a) Primitive (P), b) Diamond (D) c) Gyroid (G) surface models with eight unit cells (Han, Choi, Liu, & Kang, 2017).....	12
<b>Figure 1.10</b> : HS188 is used in military jet engine components and enables higher combustion temperatures. ....	16
<b>Figure 1.11</b> : HS188 is used in liquid fuel rocket nozzles. ....	17
<b>Figure 2.1</b> : Flow chart for specimen manufacturing.....	19
<b>Figure 2.2</b> : Concept Laser M2 Cusing. ....	22
<b>Figure 2.3</b> : Solukon <sup>®</sup> Powder Evacuation System.....	23
<b>Figure 2.4</b> : Klaege <sup>®</sup> Bitron300 3D Cut band saw. ....	23
<b>Figure 2.5</b> : Metallographic preparation steps. ....	24
<b>Figure 2.6</b> : Struers Secotom <sup>®</sup> .....	25
<b>Figure 2.7</b> : Struers CitoPress <sup>®</sup> (left) and Tegramin <sup>®</sup> (right).....	25
<b>Figure 2.8</b> : Shimadzu ag-ic 100kN <sup>®</sup> compression test device. ....	26
<b>Figure 2.9</b> : MA200 <sup>®</sup> inverted light microscope.....	27
<b>Figure 2.10</b> : Alicona InfiniteFocus. ....	28
<b>Figure 3.1</b> : Space group representation of I a-3d.....	33
<b>Figure 3.2</b> : Manually drawn gyroid surface trial. ....	34
<b>Figure 3.3</b> : Matlab code used to generate gyroid surface model. ....	35
<b>Figure 3.4</b> : Surface representation in Matlab.....	36
<b>Figure 3.5</b> : Triangulated surface detail of gyroid as extracted from Matlab. ....	37
<b>Figure 3.6</b> : DG modelling steps in UG. ....	37
<b>Figure 3.7</b> : Thickness vs cell size relation for constant volume. ....	38
<b>Figure 3.8</b> : VF change to unit cell size plot for prediction. ....	39
<b>Figure 3.9</b> : Preliminary trial measured versus modelled. ....	40
<b>Figure 3.10</b> : Secondary trial measured versus modelled. ....	41

<b>Figure 3.11</b> : Additively manufactured HS188 DG samples from left to right with 12, 8 and 6 mm unitcell sizes repectively. ....	<b>41</b>
<b>Figure 3.12</b> : Isometric view of additively manufactured HS188 DG samples from left to right with 12, 8 and 6 mm unit cell sizes. ....	<b>41</b>
<b>Figure 4.1</b> : 3mm unit cell paralel cross-section. ....	<b>44</b>
<b>Figure 4.2</b> : 3 mm unit cell convex overhang surfaces. ....	<b>45</b>
<b>Figure 4.3</b> : 3 mm unit cell concave overhang surfaces. ....	<b>45</b>
<b>Figure 4.4</b> : 4mm unit cell paralel cross-section. ....	<b>46</b>
<b>Figure 4.5</b> : 4mm unit cell perpendicular cross-section. ....	<b>47</b>
<b>Figure 4.6</b> : 4mm unit cell convex overhangs. ....	<b>48</b>
<b>Figure 4.7</b> : 4 mm unit cell concave overhangs. ....	<b>48</b>
<b>Figure 4.8</b> : 6mm unit cell paralel cross-section. ....	<b>49</b>
<b>Figure 4.9</b> : 6mm unit cell perpendicular cross-section. ....	<b>50</b>
<b>Figure 4.10</b> : 6mm unit cell hangover areas. ....	<b>51</b>
<b>Figure 4.11</b> : 6 mm unit cell less porous regions. ....	<b>51</b>
<b>Figure 4.12</b> : 8 mm unit cell paralel cross-section. ....	<b>52</b>
<b>Figure 4.14</b> : 8mm unit cell hangover areas. ....	<b>52</b>
<b>Figure 4.13</b> : 8 mm unit cell perpendicular cross-section. ....	<b>53</b>
<b>Figure 4.15</b> : 12mm unit cell paralel cross-section. ....	<b>55</b>
<b>Figure 4.17</b> : 12 mm unit cell near surface defects are changing from open to surface to enclosed as the build orientation changes. ....	<b>55</b>
<b>Figure 4.16</b> : 12 mm unit cell perpendicular cross-section. ....	<b>56</b>
<b>Figure 4.18</b> : 12 mm unit cell near surface defects size decrement in overhang areas as the build orientation changes. ....	<b>56</b>
<b>Figure 4.19</b> : 3 mm unit cell top surface profile. ....	<b>58</b>
<b>Figure 4.20</b> : 4 mm unit cell top surface profile. ....	<b>59</b>
<b>Figure 4.21</b> : 6 mm unit cell specimen top surface profile. ....	<b>59</b>
<b>Figure 4.22</b> : 6 mm unit cell specimen down facing surface profile. ....	<b>60</b>
<b>Figure 4.23</b> : 6 mm up facing (left) and down facing (right) areas micro scanning. ....	<b>60</b>
<b>Figure 4.24</b> : 6 mm unit cell specimen side facing surface profile. ....	<b>61</b>
<b>Figure 4.25</b> : 8 mm unit cell specimen top surface profile. ....	<b>62</b>
<b>Figure 4.26</b> : 8 mm unit cell specimen down facing surface profile. ....	<b>62</b>
<b>Figure 4.27</b> : 8 mm up facing (left) and down facing (right) areas micro scanning. ....	<b>63</b>
<b>Figure 4.28</b> : 8 mm unit cell specimen side facing surface profile. ....	<b>63</b>
<b>Figure 4.29</b> : 12 mm unit cell specimen up facing surface profile. ....	<b>64</b>
<b>Figure 4.30</b> : 12 mm unit cell specimen down facing surface profile. ....	<b>64</b>
<b>Figure 4.31</b> : 12 mm up facing (left) and down facing (right) areas micro scanning. ....	<b>65</b>
<b>Figure 4.32</b> : 12 mm unit cell specimen side facing surface profile. ....	<b>65</b>
<b>Figure 4.33</b> : SEM micrograph of 12 mm unit cell size specimen. ....	<b>66</b>
<b>Figure 4.34</b> : Higher magnification SEM micrograph showing unmelted powder residues inside surface voids. ....	<b>67</b>
<b>Figure 4.35</b> : Plastic and brittle compressive deformation behavior of cellular solids (I Maskery et al., 2016). ....	<b>68</b>

<b>Figure 4.36</b> : Sharp points in the specimens. ....	<b>69</b>
<b>Figure 4.37</b> : Compressive stress-strain curves of 12, 8 and 6 mm unit cell specimens with three replicates for each case. ....	<b>69</b>
<b>Figure 4.38</b> : 8mm unit cell specimen after compression test with cracks marked. .	<b>70</b>
<b>Figure 4.39</b> : Areas under the curve until densification strain: a) 12 mm unit cell, b) 8 mm unit cell, c) 6 mm unit cell. ....	<b>70</b>
<b>Figure 4.40</b> : Normalized energy absorption per volume. ....	<b>71</b>
<b>Figure 4.41</b> : Normalized energy absorption per modulus of elasticity.....	<b>72</b>
<b>Figure 4.42</b> : The relative density dependency of energy absorption in the ductile cellular structures (Gibson, L. J., Ashby, 1997). ....	<b>73</b>
<b>Figure 4.43</b> : Compressive stress-strain behavior comparison of elastic solids and foams(Gibson, L. J., Ashby, 1997). ....	<b>74</b>
<b>Figure 4.44</b> : 12 mm unit cell size compression test footage with strain values: a) 0, b) 0.2, c) 0.5, d) 0.7 before spring back. ....	<b>74</b>
<b>Figure 4.45</b> : 8 mm unit cell size compression test footage with strain values: a) 0, b)0.2, c) 0.41, d) 0.7 before spring back. ....	<b>75</b>
<b>Figure 4.46</b> : 6 mm unit cell size compression test footage with strain values: a) 0 b)0.2, c) 0.35, d) 0.7 before spring back. ....	<b>75</b>
<b>Figure 4.47</b> : SEM image of a crack near the edges after compression test. ....	<b>75</b>
<b>Figure 4.48</b> : Crushed DG specimens. From left to right: 12 mm, 8 mm and 6 mm.	<b>76</b>
<b>Figure 4.49</b> : Yield and modulus of elasticity of 12 mm unit cell specimen. ....	<b>76</b>
<b>Figure 4.50</b> : Yield and modulus of elasticity of 8 mm unit cell specimen. ....	<b>77</b>
<b>Figure 4.51</b> : Yield and modulus of elasticity of 6 mm unit cell specimen. ....	<b>77</b>



# **COMPRESSIVE STRENGTH AND CHARACTERISATION OF ADDITIVELY MANUFACTURED DOUBLE GYROID LATTICE STRUCTURE**

## **SUMMARY**

Lattice structures are gaining more importance to be utilized in structural part design due to their high strength to weight ratio, customizable relative density and loading-specific design opportunities, especially in the fields of aerospace, biomedical and automotive. Various unit cell designs have been studied in the literature inspired by the crystallographic unit cell structures such as FCC, BCC, etc. Mathematical surface model called “triply periodic minimal surface” also known as double gyroid (DG) is found to be a promising unit cell design for load bearing structural applications for its isotropy, continuous surface profile and homogeneity. The aim of this study is to understand the DG’s compressive strength mechanism in relation to its unit cell size and relative density to be employed for aerospace applications. Cubic specimens containing different sizes of unit cells were manufactured using Direct Metal Laser Melting (DMLM) process on a Concept Laser M2 equipment using HAYNES® alloy powder. DMLM of this material combining excellent high-temperature strength with very good resistance to oxidizing environments up has almost never been addressed in the literature until now. Specimens were subjected to compressive testing and compressive stress-strain plots were obtained. Along with mechanical testing, witness specimens of the same configuration were printed and metallographically examined by investigating microstructural characteristics such as porosity, phases and surface roughness. Moreover, micro hardness testing was carried out on various locations of the specimens. Results and discussion are mainly focused on the relationship between microstructural properties and compressive test results. Double gyroid specific mechanical properties of HAYNES®188 produced by DMLM such as elastic moduli, specific stiffness and plateau region characteristics are among the reported outcomes.



## KATMANLI İMALAT İLE ÜRETİLMİŞ ÇİFT GYROİD KAFES YAPISININ BASMA DAYANIMI VE KARAKTERİZASYONU

### ÖZET

Kafes yapılarıyla oluşturulmuş malzeme tasarımları gün geçtikçe daha çok önem kazanmaktadır. Bu yapıların geometrileri, değiştirilebilir ve uygulama alanına göre uyarlanabilir mekanik özelliklere sahip olmalarını sağlamaktadır. Özellikle taşımacılık, havacılık ve uzay sanayii, ulaşım, kişisel koruyucu donanımlar ve zırh malzemesi gibi alanlarda kafes yapılı hücresel tasarımlı malzemeler değerlendirilmektedir. Katmanlı imalat yöntemlerinin gelişmesiyle birlikte, geleneksel üretim yöntemleriyle üretilmesi verimsiz, zorlu veya imkansız olan karmaşık geometri kafes yapılarının üretilebilirliği mümkün kılınmıştır.

Kafes yapıları temel olarak birim hücrelerden oluşmaktadır. Birim hücrelerin üç boyutta kendilerini tekrar etmeleri neticesinde istenen hacmi doldururlar. Birim hücre geometrileri ve bütün hacmin katı hacmine oranı yani doluluk oranı, bütün yapının davranışlarını belirleyen parametrelerdendir. Yapıdaki yüksek oranda yüzey alanı, boşluk miktarı ve bu parametrelerin değiştirilebilmesi kafes yapılarının ısı aktarımı veya yalıtımı gerektiren birçok uygulamada kullanılmasına olanak tanımıştır.

Kafes yapısıyla üretilmiş bir tasarımın mekanik özellikleri de bahsedilen parametrelerle ayarlanabilmektedir. Farklı birim hücrelerin farklı mekanik özellikler sağladıklarını şimdiye kadar yapılan çalışmalarla belirlenmiştir. Özellikle darbe dayanımı gerektiren uygulamalarda, yapıdaki yüksek boşluk oranı sayesinde darbeden aktarılan enerji, yapının içindeki birim hücrelerin plastik deformasyona uğramasıyla soğurulmaktadır. Bu şekilde enerji sönmülmesi gerçekleştirilir ve parçanın diğer tarafına aktarılması engellenir. Tasarım parametrelerinin kafes yapılarının mekanik özelliklerini nasıl etkilediğinin anlaşılması, bu yapıların mühendislik uygulamalarında daha yaygın bir şekilde kullanılmaları için önem arz etmektedir.

Özellikle medikal alanda kafes yapıları yoğunlukla kullanılmaktadırlar. Aynı zamanda kemik yapısının da bir hücresel yapı olması, doğayı taklit edip tasarımların oluşturulması açısından örnek oluşturmaktadır. Tasarlanacak protezler, üzerinde kullanımları sırasında oluşacak yüklenme koşullarına göre özel birim hücre boyları ve geometrileri ile oluşturulmaktadır. Bu şekilde, kafes yapılarının en avantajlı özelliklerinden birisi olan tasarım uzayı içerisinde farklı mekanik özelliğe sahip bölgelerin oluşturulması sağlanmaktadır. Aynı zamanda, farklı boyut ve dağılımlarda organize edilen boşluklar, protezin vücutta bulunduğu bölgeye bağlı olarak dokuların protez içine büyümesi sağlanabilmektedir.

Literatürde, birçok farklı kafes yapısının analiz yahut test ile mekanik özelliklerinin anlaşılması üzerine çalışmalar mevcuttur. Katmanlı imalat üretim yönteminin olgunlaşmasıyla yoğunlukla metalik malzemelerin atom dizilimlerinden yani

kristallograflerinden etkilenilerek önerilmiş birim hücre tasarımları denenmeye başlanmıştır. Yüzey merkezli kübik veya hacim merkezli kübik gibi birim hücre modelleri, atomların hücredeki pozisyonları arasına bağlantı elemanları yerleştirilerek payanda tipi birim hücre modelleri geliştirilmiştir. Bu modellerin çok düşük hacim oranlarında üretilebilmeleri ve çok büyük yüzey alanlarına sahip olmalarının avantaj teşkil etmesinin yanı sıra, tasarımların çoğunlukla keskin bağlantı noktaları içermesi stres konsantrasyonu oluşmasına sebebiyet vermektedir.

Alternatif bir yaklaşım olarak payanda tipi birim hücreler yerine yüzey modelleri önerilmiştir. “Triply periodic minimal surface” (TPMS) ismiyle tabir edilen yüzey grubu, birim hücre geometrisi içerisinde farklı analitik ifadeler referans alınarak neticede yüksek performanslı malzeme tasarımları oluşturacak şekilde konumlandırılabilmiştir. Bu yüzey modelleri, her yönde aynı döngüsel tekrarları yapmaktadırlar, bu sebeple bu yüzey modelleri referans alınarak oluşturulan geometriler izotropiktir. Tüm yüzey geçişleri sinüzoidal hatlar takip edilerek sağlandığı için aynı zamanda köşe içermeyen TPMS’ler, stres konsantrasyonu oluşturmazlar. Aynı zamanda, bu yüzeylerin boşluk bölgeyi ayrı tanımlanabilen hacimlere ayırmaları sayesinde akışkan geçişi gerektiren, ısı transferi için ideal yapıların üretilmesi literatürde önerilmiş ve patentlenmiştir. TPMS’ler arasında yapılan hücresel tasarımlı malzeme geliştirme çalışmaları sırasında, 1969’da tanımlanan gyroid adı verilen yüzey tasarımından oluşturulan malzemeler, mekanik avantajlarıyla öne çıkmıştır.

Gyroid yüzey modeli kullanılarak farklı katı oluşturma stratejileri önerilmiştir. Uzayı ikiye ayıran gyroid yüzey modeliyle oluşturulan çift gyroid yapısı, tasarım yüzeyinin bölgesel normallerinin pozitif ve negatif yönlerinde iki ayrı yüzey oluşturulması ve bu yüzeylerin arasındaki bölgenin katıyla doldurulması yoluyla oluşturulmuştur. Bu çalışmada üretilen ve test ve karakterize edilen numune yapının birimlerini çift gyroid yapısı oluşturmaktadır.

Bu çalışmada, Haynes188 ticari isimli kobalt bazlı alaşımdan oluşan toz hammadde kullanılarak katmanlı imalat yöntemiyle üretilen DG yapılarının basma mekanik özelliklerinin birim hücre boyu ve et kalınlığından nasıl etkilendiğinin anlaşılması amaçlanmıştır. Bu amaçla, 24 mm birim ölçüye sahip küp geometrili numuneler, 6, 8 ve 12 mm birim ölçülü bitim hücre DG yapılarıyla tasarlanmıştır. Numunelerin tamamının aynı yahut kabul edilebilir bir hata ile aynı ağırlıkta üretilebilmesi için et kalınlıkları değiştirilmiş olup, nihai olarak test edilen geometrilerde aynı hacim oranına ulaşılmıştır.

Tekrarlanabilirliğin sağlandığından emin olabilmek için her geometrideki numuneden basma testi için üçer tane üretilmiştir. Bunun yanı sıra, diğer hasarlı ve hasarsız muayenelerin numuneler üzerine uygulanması için test numunelerinin yanı sıra şahit numuneler de üretilmiştir. Stereo ve ters ışık mikroskobu, üç boyutlu mikro yüzey taraması, ağırlık ölçümü uygulanan hasarsız muayeneler arasındadır. Numunelerin metalografik yapıları, numunelerin metalografik olarak hazırlanması sonrası ters ışık mikroskobunda incelenmiştir. Elde edilen sonuçlar katmanlı imalat üretim yönteminin DG yapılarının üretilmesiyle ilgili gereken ilişkilerin yorumlanmasını sağlamıştır. Basma testine tabi tutulan numuneler kamera ile test boyunca görüntülenmiş ve görüntüler elde edilen grafiklerle eş zamanlı değerlendirilerek yorumlanmıştır.

Basma testinden elde edilen sonuçlar, hücresel yapıların mekanik analizleri için literatürde önerilmiş yöntemlere göre yorumlanmıştır. DG yapılarının basma

dayanımları, yoğunlaşma öncesi yük kapasiteleri, toplam sönümleyebildikleri enerji miktarı ve bu niceliklerin DG birim hücre boyuyla nasıl değiştikleri belgelenmiştir.





## **1. INTRODUCTION**

In this study, additively manufactured lattice cellular structure comprising of one of the triply periodic minimal surface (TPMS) models called gyroid unit cells made of Haynes 188<sup>®</sup> (HS188) alloy powder is characterized and compressively tested. For manufacturing the samples, one of the additive manufacturing modalities called direct metal laser melting (DMLM) system is used. Capability of DMLM with its advantages and disadvantages, literature search on state of the art on cellular structures and more specifically TPMS unit cell models and finally fundamental metallurgical properties of HS188 with its fields of application are covered in this chapter.

### **1.1 Additive Manufacturing**

Additive manufacturing (AM) is a type of manufacturing parts by adding material layer-by-layer as opposed to obtaining the final shape by traditionally removing material from a substrate or forming a raw material into its final form. It gained noteworthy popularity in many businesses owing to its much more limitless capability to manufacture complex parts and design features (Herzog, Seyda, Wycisk, & Emmelmann, 2016).

There have been many diverse AM processes industrialized in the last two decades, each with different opportunities and limitations. In all of the processes, the main common aspect is to slice a computer aided design (CAD) model to create each layer's data. The AM system uses the sliced data to gather the material layer-by-layer by suitable fusing techniques according to the used material. For metals, there are many modalities industrialized and many more are still under development. The selection of the correct modality plays a critical role in achieving the desired final part characteristics (Frazier, 2014; Jasiuk et al., 2018).

Powder bed fusion systems, also as known as selective laser sintering (SLS), selective laser melting (SLM) or DMLM, is the most widely researched AM modality up to now. In the process, the metallic powder is spread onto a metal base plate resulting

with a flat powder surface, which is called the powder bed. Then a laser selectively scans the desired area by using the data of the sliced layer and melts the powder particles locally as it passes through. Melted metal immediately solidifies as the heat input from the laser moves further. Prior to the solidification, the melt pool penetrates through the base plate by creating a metallurgical bonding. Following the completion of the laser's exposure on one layer, plate is lowered equal to a layer thickness and for the next layer, powder is coated on top of the solidified layer. As the laser scans the next layer, the melt pool penetrates into the previously solidified layer. Repeating the same process for each layer, at last the part is completely manufactured with the desired geometry (see Figure 1.1) (Farid, Shirazi, Gharekhani, & Mehrali, n.d.; Frazier, 2014; Herzog et al., 2016).

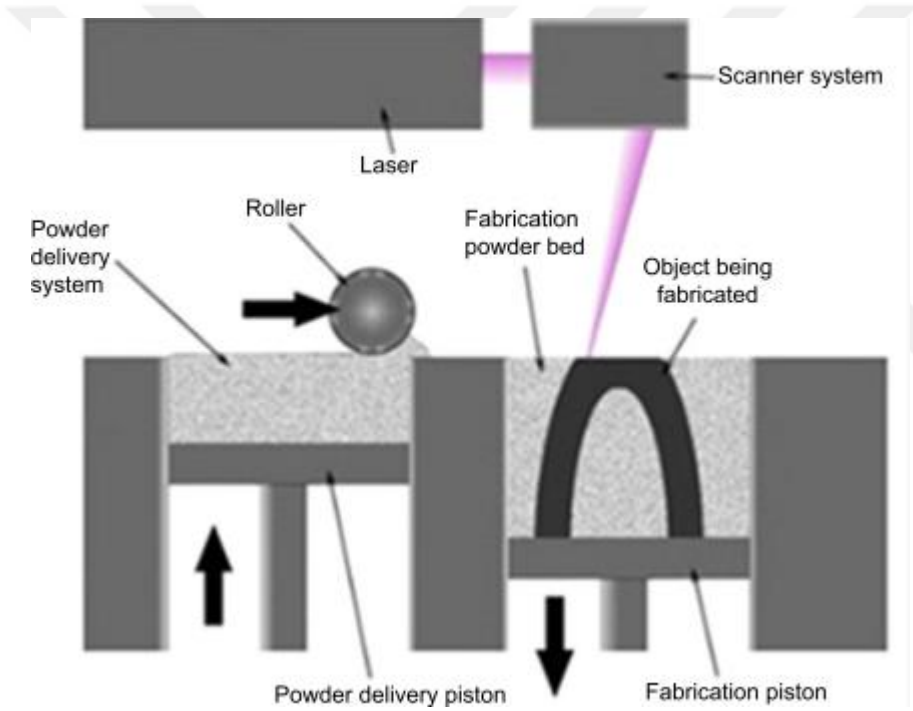


**Figure 1.1 :** Powder bed additive manufacturing (Farid et al., n.d.).

The main advantage of DMLM is its high precision and quality manufacturing capability. Part designs that are impractical or impossible to be manufactured by conventional methods have become possible and feasible with this technology. The DMLM Technology enables the designers to think beyond the boundaries of traditional manufacturing methods and design much lighter and yet stronger systems. Since the modality is matured to some extent, there have been many successful attempts reported on manufacturing parts with novel design features. DMLM also maximizes the potential of topology optimization by enabling the designers to position

material in exact necessary places in three dimensional design space only wherever required. Furthermore, re-designing parts to high functional systems as a single component by the capabilities of DMLM comes with the advantage of combining different parts into a single combined model (Adedeji, 2013; Gao et al., 2015; Gaynor, 2015).

On the other side, there are still numerous aspects requiring development for the complete industrialization of the process. Material properties and additively manufacturability of some alloy systems possesses challenges. Build orientation dependent material characteristics and surface quality must be considered for the function of parts (Driessen, 2016; Stanković, Mueller, & Shea, 2017). Distortion caused by thermal stresses requires special attention for obtaining the desired geometry. (Farid et al., n.d.; Frazier, 2014; Herzog et al., 2016)

One of the highly functional novel material classes that DMLM has enabled is meta-materials. “Meta” prefix stands for “beyond” in Greek by referring the enhanced properties that these material designs possess regardless to their chemical contents, manufacturing methods and strengthening post-processes. Belonging to this type, additively manufactured cellular structures promise an exceptional potential for future material application areas such as transportation, health care, aerospace and personal protective equipment.

## **1.2 Cellular Structures**

Humankind has long been using a variety of materials for specific tools and structures. Materials with different properties are employed accordingly to the application requirements. Specifically, weight-critical applications such as transportation, aviation, personal protection and packaging require as low material as possible to withstand the mechanical stress loading conditions in component designs. Components in such applications may withstand tensile and compressive loads and the combination of these, in torsion, tension, and bending. In order to achieve such efficient designs, distribution of material over the design space becomes critical by promises of carrying the properties of the whole structure far beyond the bulk properties of the used material. For this purpose, cellular structures have long been used in many engineering applications because of their highly configurable

mechanical properties together with light weights. (Axel S. Herrmann, Pierre C. Zahlen, 2005; Gibson, L. J., Ashby, 1997; Rupani, 2017)

A cellular structure is composed of small solid units combined together to form the whole structure (see Figure 1.2. Each of these units is called unit cells and designs aspects of each unit cell combined with the strategy to stack them finally defines the properties of the whole structure. There are many examples of cellular structures in nature. Wood and animal bones are cellular structures with consists fibers and pores covered by a hard shell to provide higher mechanical strength with lighter weights. (Gibson, L. J., Ashby, 1997)

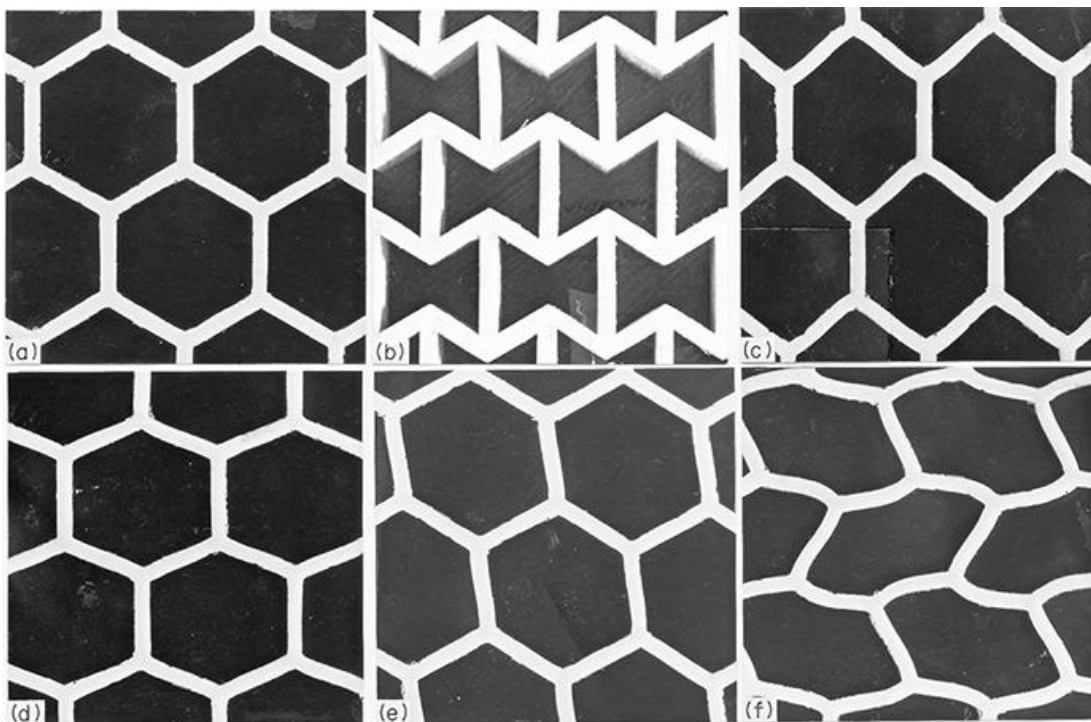


**Figure 1.2** Cellular structure examples (Gibson, L. J., Ashby, 1997).

Cellular structures are designed with various strategies. Metal and polymer foams, honeycombs and lattices are among most popularly used cellular materials (see Figure 1.3). Foams consist of irregularly dispersed stochastic voids inside the structure and relative density of the whole arrangement is the key effecting parameter on the mechanical properties. Foams are mainly considered as closed cell cellular structures because of their enclosed voids inside. There are several manufacturing methods for the polymer and metal foam materials which can be classified by the ability to control foams densities(A, 2006; Fleck, Deshpande, & Ashby, 2010; D. Lee, Khan, & Jasiuk, 2016). Honeycombs are made of sheets fused together in the shape of hexagons. They

have been employed in many engineering applications due to their high efficiency and ease of manufacturing (Harris, Winter, & McShane, 2017; Rupani, 2017).

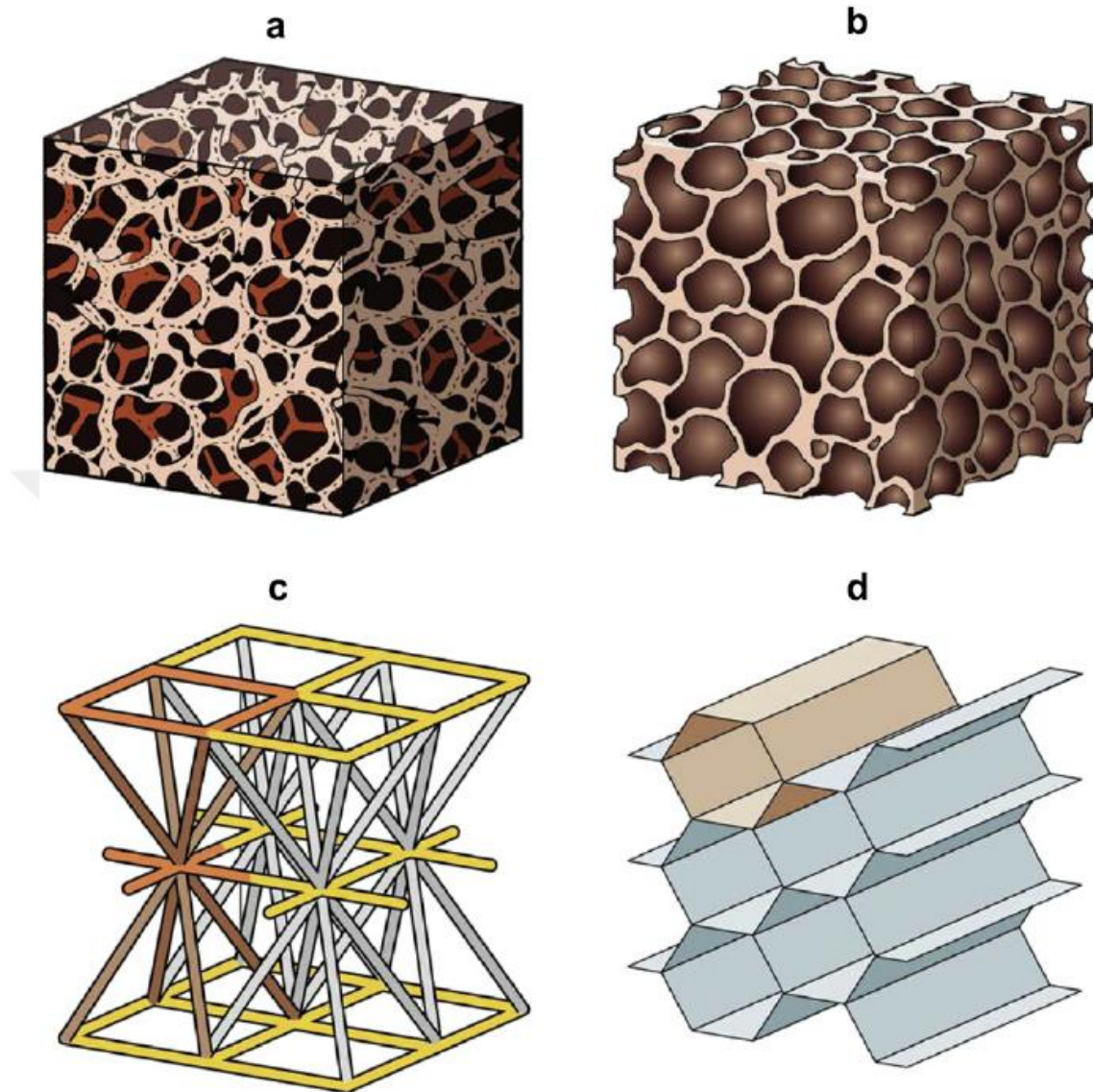


**Figure 1.3 :** a) open cell foam b) closed cell foam c) structural lattice structure d) honeycomb lattice structure(H. N.G. Wadley et al., 2010).

Structures composed of network of trusses and beams with different size and arrangement is called lattices. The unit cells of lattice structures are mostly well defined and homogeneously distributed. Design freedom and highly adjustable dimensional parameters make them superior in comparison to more stochastic cellular structures. Lattices can either be studied as a complex network of trusses, beams and connections by traditional means or they can be regarded as meta-materials (Bauer et al., 2017; Fleck et al., 2010; Gümrük, Mines, & Karadeniz, 2013).

The advantage of lattice structures over the other cellular structures comes at the price of manufacturing. Such complex structures have been expensive and inefficient to manufacture with traditional methods (Rashed, Ashraf, Mines, & Hazell, 2016). With the help of additive manufacturing, lattices have started gain considerable attention. Unit cells with a very wide variety of designs have started to be investigated especially in order to understand their mechanical behavior (Delpero, Bergamini, Ermanni, & Kochmann, 2014; Ullah, Elambasseril, Brandt, & Feih, 2014).

In the recent years, many lattice structures are proposed, mainly inspired by the atomic distribution of space groups and their combinations. Face centered cubic (FCC), base centered cubic (BCC), FCC with a truss placed in the direction of loading(FCCZ) and octet truss lattices are among the widely studied examples (see in Figure 1.4) (Xiong et al., 2015; Yan, Hao, Hussein, Young, & Huang, 2015). Besides the unit cell examples inspired by nature, various studies are focused especially on novel unit cell designs. Building analytic models for designing lattice structures for an optimized topology and obtaining the desired characteristics have been studied in multiple publications. (McMillan, Jurg, Leary, & Brandt, 2015; Seifi, Rezaee Javan, Xu, Zhao, & Xie, 2018; Tang, Kurtz, & Zhao, 2015) Although additive manufacturing enables many novel unit cell geometries to be manufactured, due to the powder size and build orientation issues there are still some limits especially for the truss diameter and unit cell size for lattices. Tanlak, N. *et al.* has developed a numerical approach on predicting the final part density for lattice structures.(Tanalak, De Lange, & Van Paepegem, 2017)

Characterizing the mechanical properties of lattice structures is required. There have been many reported studies on understanding mechanical properties of different unit cell designs, sizes materials under various failure modalities. Due to their high potential of energy absorption, energy absorption and compressive strength behaviors are widely investigated (Delpero et al., 2014; Mohsenizadeh, Gasbarri, Munther, Beheshti, & Davami, 2018). Fangfang, S. *et al.* have studied the compression behavior and energy absorption characteristics of triangular lattice structures. (Sun, Lai, & Fan, 2016) Amer, B. *et al.* compared the dynamic impact response of sandwich structures with different core lattice unit cell designs (Beharic, Rodriguez Egui, & Yang, 2018). In the study of Yi Tang, K. *et al.*, a promising low impact velocity response of additively manufactured lattice structures with foam reinforcements was shown. This study points out the substantial potential for using additively manufactured complex

lattice structures for metal-polymer composite material designs. (Kao, Amin, Payne, Wang, & Tai, 2018) Other mechanical tests such as torsion, three-point bending and tensile are also performed on different lattice structures. As a result, different unit cells are found to have different properties that could represent an advantage in a failure modality while could represent a disadvantage in another failure modality.(Du, Li, Luo, & Tian, 2017; Gümrük et al., 2013; Rahman Rashid, Mallavarapu, Palanisamy, & Masood, 2017; Xiong et al., 2015; Yan et al., 2015; Zargarian, Esfahanian, Kadkhodapour, & Ziaei-Rad, 2016)

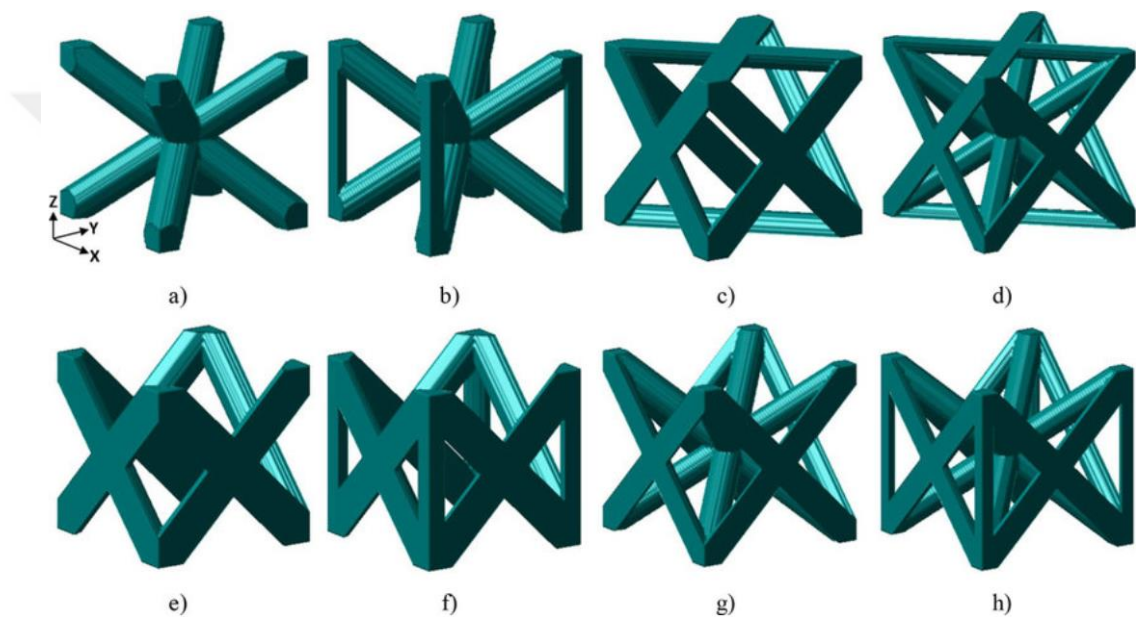


**Figure 1.4 :** Truss lattice unit cell type examples a) BCC b) BCCz c) FCC d) FBCC e) S-FCC f) S-FCCz g) S-FBCC h) S-FBCCz (Panesar, Abdi, Hickman, & Ashcroft, 2018).

Another great enhancement that AM brings in manufacturing of lattices is the capability of changing the unit cell design parameters relative to the loading conditions and structural requirements. This type of lattice structures is called functionally graded lattice structures. Since the loading conditions, critical failure modalities and stress critical locations are neither homogenous nor repetitive along the structure, changing the unit cells in relation to requirements has the potential of weight reduction. Functionally graded lattices are perfect examples of lattice structures with a great ability of adjustable mechanical properties such as elastic moduli (Al-Saedi, Masood, Faizan-Ur-Rab, Alomarah, & Ponnusamy, 2018; Choy, Sun, Leong, & Wei, 2017; Dumas, Terriault, & Brailovski, 2017; Kadkhodapour, 2016; Li et al., 2018; Ian

Maskery et al., 2016; Panesar et al., 2018; Terriault & Brailovski, 2018; Y. Wang et al., 2018). Moreover, changing density in the direction of dynamic impact loading has proven to increase to energy absorption capacity of the structure (Al-Saedi et al., 2018; L. Chen et al., 2018; Panesar et al., 2018).

In industrial applications, there are many fields of opportunity for lattice structures. High energy absorption values in relative to their weights and promising dynamic impact responses make them perfect candidates for personal protection equipment, armors and packaging; structural parts for transportation, aviation and aeronautics. Since their surface area is significantly high, they can be employed for heat transfer requiring applications such as heat exchangers as seen in Figure 1.5 (Ferro, Varetto, De Pasquale, & Maggiore, 2018; Ryan, 2014; Science, Issn, & Publications, 2007; Wen, Tian, & Lu, 2006). Owing to their adjustable stiffness and variable truss diameters, lattice structures are also proposed and proven to show functionality as support structures for metal additive manufacturing (Hanzl, Zetková, & Daňa, 2017).

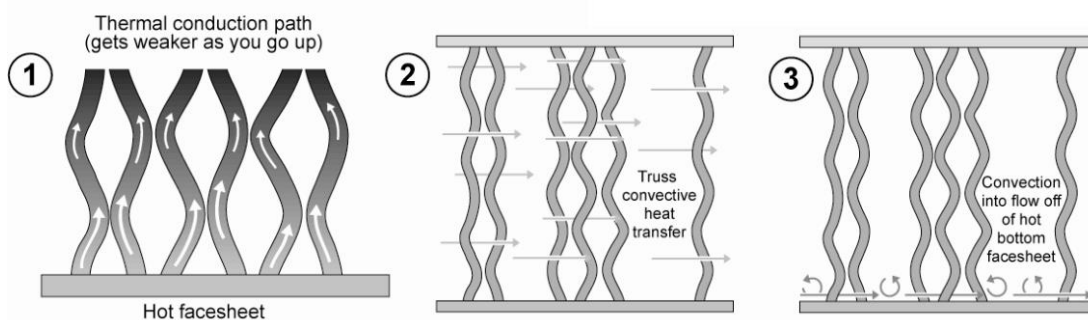


**Figure 1.5 :** Heat exchanger application example for lattice structures (Haydn N.G. Wadley & Queheillalt, 2009).

Prior to fully industrialization of structural lattices, effect of design parameters of lattice structures on their mechanical properties should be well understood. Furthermore, the current state of the art in unit cell design is yet to reach its limit for efficiency. By numerical proofs, computational models and bio-mimics, there is a huge potential for inventing and implementing novel advanced unit cell designs. Among the promising unit cell design ideas, periodic structure model of minimal surfaces steps out by taking the attention of researchers recently.

### 1.3 Triply Periodic Minimal Surfaces

Mathematical advances especially in group theories are essentially significant for explaining and analytically modeling the repetitive occurrences observed in nature. Following the progressions in science and instrumentation in the field of crystallography in the mid-19<sup>th</sup> cc., classification and identification of crystal structures gained considerable importance. In the following decades, solid state physics enabled the scientists to develop novel group models which would proceed beyond the area of fundamental research and take a significant place in engineering applications in the future. Among the historically studied repetitive models, the class of infinite surfaces represents the background of the model of interest of this study.

Initial infinite analytical surface expressions are dating back to the 19<sup>th</sup> cc. German mathematician Schwarz, H. A. has published the first widely approved discovery of infinite minimal surface model and called “Schwarz surface” in the literature (Schoen, 1970). In his study, he describes various infinite surface models that grow in all dimensions without any self-interaction. Later in 1968, Luzatti *et al.* discovered the surface pattern in lipid polymorphs that can be related to the triply periodic surface (TPMS) model and regarded as single gyroid (SG) (Luzzati, V., Spegt, 1967). In 1970, NASA scientist Alan H. Schoen published a study concerning various TPMS models.

Minimal surfaces are defined as surface models which have a local area minimizing in every location. That means, the sum of the principle curves passing through the location is always zero. From another point of view, for a surface to enclose the same volume, minimal surface is the one that has the least amount of surface area. There are many examples in the nature, where the surface tension plays the major role in shaping the surface of liquid to solid or gas phases such as soap bubbles and water drops. Energy of the soap bubble film equals the surface area times the surface tensions. Since the film thermodynamically tends to minimize its energy, area of the film is autogenously minimized. This efficiency observed in nature is a great value to be benefited for the engineering applications by arranging matter in the most efficient way possible (H. Chen & Thornton, 2009; Kapfer, Hyde, Mecke, Arns, & Schröder-turk, 2011; Rossi, 2017; Schoen, 1970, 2012; Torquato, Donev, & A, 2004; Yang, Lee, & Kim, 2010).

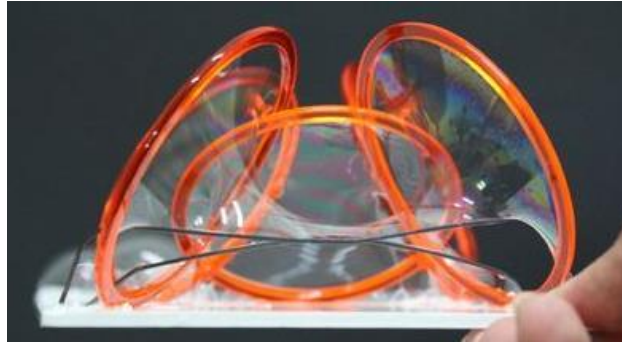


**Figure 1.6 :** Soap film is the most common example of minimal surfaces (URL-1).

Minimal surfaces mentioned in Schoen's study are considered triply periodic since the surfaces expand in all dimensions periodically and without any self-interactions. The lack of self-interaction ensures the continuity of the surface as well as dividing the space into two separate regions. Besides, as a result of periodicity, each TPMS can be considered to have a space group symmetry. (Jung & Torquato, 2005)

There are spectacular examples in nature of TPMS structures. Study of Michielsen and Stavenga showed the gyroid like TPMS surface model exist in the nano-structures that composes the outer layer of number of different butterfly species wings. According to their study, voids in the gyroid nano structure reflects, interferes and absorbs specific wavelengths in the visible spectrum of sun light so that remaining reflected light's wavelength lies in the specific color ranges in the visible spectrum. (Michielsen & Stavenga, 2008) Galusha *et al.* showed that there are cuticular diamond-like microstructure in the armor scales of the beetle called *Lamprocyphus augustus* as seen in Figure 1.7 (Galusha, Richey, Gardner, Cha, & Bartl, 2020). In the recent years, there has been numerous studies performed especially about gyroid-like patterns found on the butterfly wings (see Figure 1.8) (Apeleo Zubiri et al., 2017; Dieker et al., 2015). Furthermore, the mitochondria located at the inner segment of the retinal cones of a specific tree species' shrew contain unique patterns that are geometrically associated with several TPMS models (Almsherqi, Margadant, & Deng, 2012).



**Figure 1.7 :** Diamond TPMS structured shell of *Lamprocyphus augustus* (URL-2).



**Figure 1.8 :** *Teinopalpus imperialis* with gyroid-like layer on their wings to reflect green light only (URL-3).

Using dividing surface designs are very beneficial for manufacturing composites with unique and application specific properties. Different phases can be utilized in a very efficient manner to superior the desired characteristics. Wang *et al.* manufactured glassy and elastomer co-continuous polymers by using TPMS design and obtained specimens with enhanced mechanical properties, especially in energy absorption (L. Wang, Lau, Thomas, & Boyce, 2011). Lattice structures can be modified and arranged in specific orders accordingly for individual applications. TPMS models exhibit higher surface to volume ratio in comparison to those of truss-lattice structures and this aspect can be benefitted in different applications (D. Lee et al., 2016; Park & Lee, 2017; Yoo, 2014).

Several TPMS models are given in Figure 1.9.

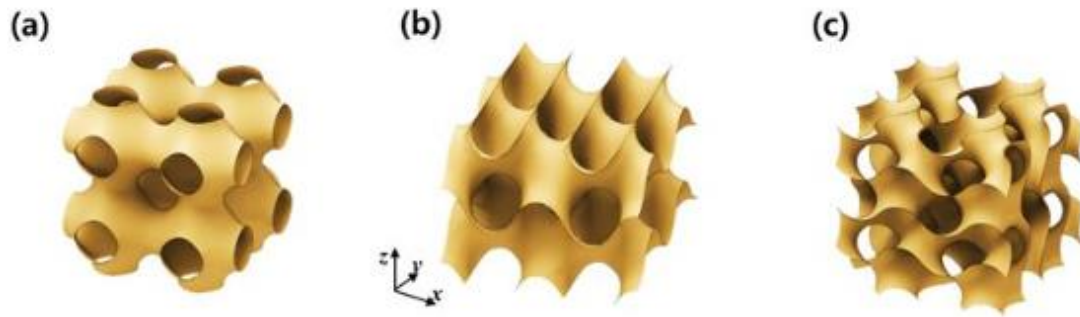


**Figure 1.9 :** a) Primitive (P), b) Diamond (D) c) Gyroid (G) surface models with eight unit cells (Han, Choi, Liu, & Kang, 2017).

Belonging to the TPMS family, there are more surface models designed. Studied examples for such surfaces include Schwarz crossed layers of parallels (CLP), Diamond, Neovius, Schoen I graph and wrapped package-graph (IWP) and Fischer-Koch S models. These models have been numerically characterized by various methods in previous studies (Abueidda, Jasiuk, & Sobh, 2018; D. Lee et al., 2016; W. Lee, Kang, Song, Moon, & Kim, 2016).

There is a plurality of strategies to create solid representative structures by using TPMS models. Since they are space dividing surfaces, solid volume could be arranged to be around the 2D surface itself. In this case, a sheet like solid volume aligned with the surface is created and called matrix phase. In another example, if one of the divided spaces is filled with solid and the other remains empty, network phase structure is obtained. According to each specific TPMS model and its phase, properties would vary (I. Maskery, Aboulkhair, Aremu, Tuck, & Ashcroft, 2017; I. Maskery, Sturm, et al., 2017).

Besides the fact that they are considered under the same family, critical application-specific properties may vary in each distinct structure. In the comprehensive study of Maskery *et al.*, the mechanical performance of aforementioned specific TPMS types is examined. According to their results, primitive structure exhibits higher modulus of elasticity while demonstrating strut stretching and buckling deformation characteristics opposed to bending dominated behavior observed in other TPMS models. (I. Maskery, Sturm, et al., 2017) According to many previous studies especially focusing on the mechanical behavior of TPMS models, matrix phase structures exhibited higher modulus of elasticity in comparison to network phases

(Jung & Torquato, 2005; W. Lee et al., 2016; I. Maskery, Sturm, et al., 2017; Park & Lee, 2017; Torquato et al., 2004).

Owing to additive manufacturing, TPMS models were able to go beyond computational analysis and to be manufactured. As the gravity on the lattice structures has shifted towards to surface models of which offers a potential for being superior against truss lattices, there have been many reported studies of employing additive manufacturing for printing TPMS models and testing (Li et al., 2018; Vaezi, Seitz, & Yang, 2013). Polymeric micro TPMS models have been manufactured and tested for compressive behavior examination by Al-Ketan *et al.* (Al-ketan, Rezgui, et al., 2018). Additionally, Khan *et al.* studied Primitive, Neovius and IWP TPMS models in order to document their mechanical properties such as visco-elastic behavior with addition to their bulk, uniaxial and shear storage and loss of modulus of elasticity. They also published stiffness values in relation to relative densities (Khan & Al-rub, 2017, 2018; Khan, Al-rub, & Asce, 2018).

Accompanying the method of manufacturing, there have been numerous materials used with TPMS lattice structures. Using stainless steel, Zhang *et al.* published the mechanical properties of P, D and G surfaces by compressive testing. Their energy absorption diagrams have been published in the study and reported values of TPMS structures considerably outperforms BCC truss lattice structures (Zhang, Feih, & Daynes, 2018). In the study of Al-Ketan *et al.* different examples of skeletal-TPMS, network phase TPMS and truss lattice structures have been additively manufactured by using maraging steel. According to the tests performed on the structures, valuable comparison results have been published. It is shown that network TPMS structures exhibit better mechanical properties than truss lattices. However, in between various TPMS structures, relative density plays a critical role in mechanical properties (Al-ketan, Rowshan, & Al-rub, 2018).

Representing another valuable advantage of lattice structures, functionally grading the unit cells in order to provide the application-specific requirements is of great interest in engineering applications. Han *et al.* customized P surface lattice structure design with elongating the unit cells in the direction of expected loading (Han, Lee, & Kang, 2015; M. G. Lee, Lee, Han, & Kang, 2016). Functionally grading TPMS structures have been gaining attention recently. Multiple studies especially focusing on grading

the unit cell sizes and shell thicknesses in order to adjust the relative density has been performed both by modelling, manufacturing and testing. These studies show that functionally grading the relative density over the structure in accordance with the mechanical requirements may be beneficial for the efficiency of the entire part design and enables topological optimization by using TPMS unit cell structures. (Li et al., 2018; Terriault & Brailovski, 2018).

Besides the studies with metals, there have been numerous publications concerning ceramic and polymeric TPMS structures. Restrepo *et al.* manufactured ceramic TPMS structure for bone tissue scaffolds (Werner & Pieranski, 2017). Furthermore, polymeric additive manufacturing modalities have been employed for the manufacturing of TPMS structures, mainly for examining manufacturability and building correlations between FEM models and test results (Abueidda et al., 2017; Giannitelli, Accoto, Trombetta, & Rainer, 2013; Kadkhodapour, 2016; Li et al., 2018; Melchels et al., 2010).

Up to date, there are already patented inventions concerning triply periodic minimal surfaces. Slaughter, V. B., claimed to use minimal surface models for heat exchanger components by benefiting from the high surface area of minimal surfaces (Slaughter, 2011). Ryan, R. C., proposed to use periodic minimal surface structures for heat and mass transfer by using two separate networks inside. In the proposed application, two separate fluids can pass through the channels without merging and heat transfer can be achieved in between them through the long network of passages (Ryan, 2014). Moreover, owing to their high surface area, Al-Rub, A. *et al.* invented a design approach for catalytic converters by TPMS and a composite material structure by leveraging from gyroid's dividing surface model (Abu Al-Rub, Rashid Kamel, Al-Ketan, 2016; Rashid Abu Al-Rub, 2017).

#### **1.4 Haynes 188**

Haynes<sup>®</sup> 188 (HS188) is a commercially available super-alloy under registered trademark of Haynes International Inc.'s Haynes<sup>®</sup> alloy group. HS188's main advantage is its very high oxidation resistance up to 1095°C while maintaining strength for prolonged exposures (URL-4). Development of the alloy dates back to

1966 for its high temperature capability is leveraged for turbine blades, combustor liners and afterburner tail-pipes (Klarstrom, 1993).

The chemical composition of HS188 is given in the Table 1(Klarstrom, 1993).

**Table 1 :** Chemical composition of HS188.

<b>Element</b>	<b>Min</b>	<b>Max</b>
Chromium	21.0	23.0
Nickel	20.0	24.0
Tungsten	13.0	15.0
Carbon	0.05	0.15
Boron	-	0.015
Manganese	-	1.25
Silicon	0.20	0.50
Phosphorus	-	0.02
Lanthanum	0.03	0.12
Iron	-	3.0
Cobalt	Bal.	Bal.
Sulfur	-	0.015

Chromium improves the oxidation and hot corrosion resistance and also produces  $M_6C$  carbides for strengthening following to aging heat treatment. Nickel stabilizes FCC form of matrix and improves workability. Relatively high tungsten content enables solid solution strengthening by producing  $M_6C$  carbide (Odabasi, A., N. Unlu, G.Goller, E.S. Kayalı, 2013). This formation makes the cross-slip and climb of glide dislocations more difficult by lowering the stacking fault energy. Carbon content ensures strengthening by carbide formation during crystallization. Boron provides strengthening by affecting the grain boundaries and possibly by forming precipitates. Finally, as a rare-earth element, lanthanum provides high temperature corrosion resistance. Other reported carbide phase formations in HS188 are  $M_{12}C$  and  $M_{23}C_6$  (Klarstrom, 1993; Rothman, M. F., Zordan, R. D., Muzyka, 1984).

The majority of the Co-based alloys are not as oxidation resistant as Ni-based alloys. Non-protective CoO layer formation in elevated temperatures is the main cause of

oxidation. HS188 has a superior corrosion resistance compared to many other Co based alloys, similar to those of Ni-based alloys. This superiority is mainly provided by the addition of La. However, as the temperature exceeds the level of 1100 °C, corrosion resistance of HS188 decreases drastically. This behavior is mainly related with the formation of  $\text{Co}_2\text{WO}_4$  phases in the matrix (Rothman, M. F., Zordan, R. D., Muzyka, 1984).

HS188 is mainly used in hot section parts of gas turbine engines. Application areas such as aerospace, power, commercial and military aviation have long been considered for this alloy significantly. By enabling higher combustion temperatures, efficiency and performance of engines are increased by the use of HS188 (see Figure 1.10). It is also used in aeronautical and space based applications requiring high thermal-shock resistance such as liquid oxygen posts of space shuttle main engines as seen in Figure 1.11 (Bonacuse, 2016; Odabasi, A., N. Unlu, G.Goller, E.S. Kayalı, 2013; Rae, Castelli, & Ellis, 1995; Yilbas & Akthar, 2011).



**Figure 1.10** : HS188 is used in military jet engine components and enables higher combustion temperatures (URL-5).



**Figure 1.11 :** HS188 is used in liquid fuel rocket nozzles (URL-6).

High temperature super alloys are not considered as lightweight metals. Due to the higher density of their alloying elements, they do not offer a substitution for their lightweight alternatives such as titanium or aluminum based alloys from weight perspective. Considering high strength to weight ratio and aforementioned heat transfer component applications of structural lattices, combining structural lattice designs with high temperature super alloys embodies considerable potential especially for light weight and performance requiring high temperature applications.

### **1.5 Problem Statement**

In this study, unit cell size's effect on DG structure's compression behavior is aimed to be documented. Specimens for compression testing are to be additively manufactured and besides these, witness specimens for other destructive and non-destructive testing are modelled. DG structure's mechanical performances relationship with unit cell size and additive manufacturing modality are among the most important outcomes.



## 2. EXPERIMENTAL SETUP AND CHARACTERIZATION

In this chapter, the equipment and software used throughout the study are described including design, build preparation, manufacturing, testing and characterization (see Figure 2.1). Unfortunately, characterization of lattice structures is neither standardized nor well documented in the literature. For different types of lattice structures and different challenging lattice applications, novel methods for characterizing the geometry and material are required to enable the engineers to choose the most convenient application specific lattice design parameters.

Process followed to obtain the specimens are detailed in the following sections of 2.1 and 2.2 and also be seen in Figure 2.1.

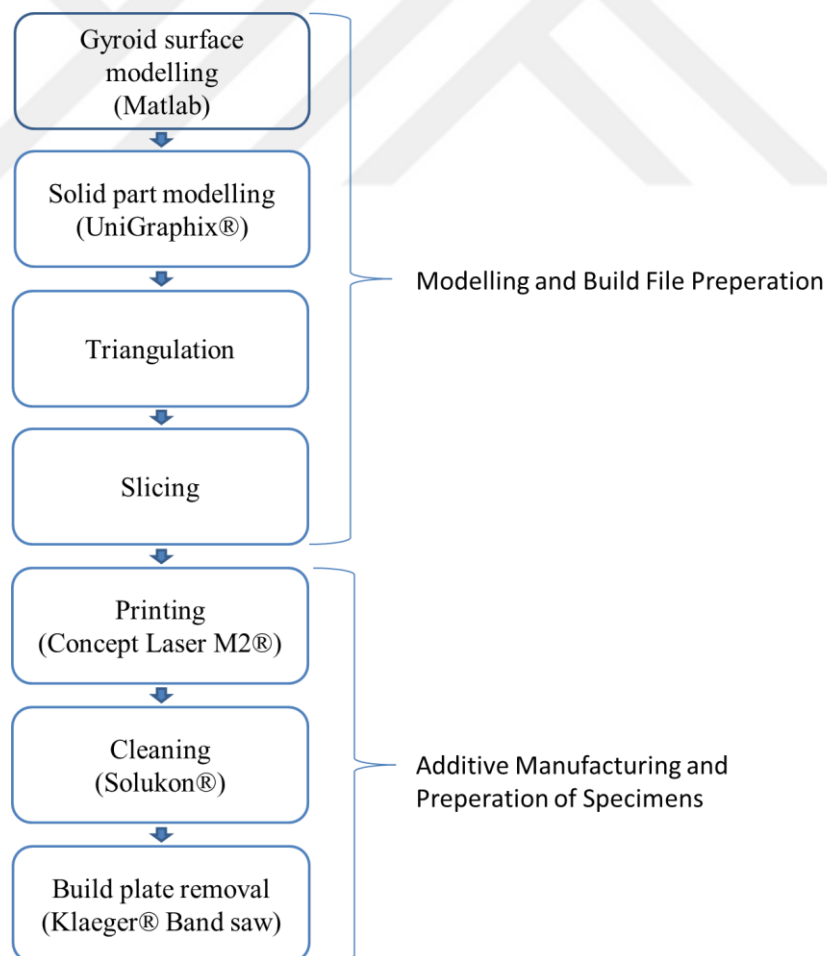


**Figure 2.1 :** Flow chart for specimen manufacturing

## 2.1 Modelling and Build File Preparation

The file containing the necessary information for an additive manufacturing system to build a part or multiple parts is called the build file. Creating the build file can be divided into 3 steps: Part modeling, triangulation (stl conversion) and slicing.

The solid part model can be created by using various computer aided design (CAD) modeling software. Then the solid model is converted to a triangulated surface model. Since each software has their specific vectoral analytical model for representing part's bodies and surfaces, a standardized method for data conversion is required to maintain the software and data compatibility in between the build files and different additive manufacturing systems.

Standard tessellation language (STL) data format is created for this purpose (Frazier, 2014). Surfaces of parts are tessellated by using two-dimensional triangular elements. Triangles merely carry the information of their plane normal and negative normal directions. In all STL files, part's bodies are represented only by the volume that the triangles encircle with their plane normal directions aligned outwards. Similar to the meshed models of finite element analysis, printed part's geometry and surface characteristics are intensely affected by the quality of triangulation. Therefore, various software solutions were created to fix the errors which occur during triangulation. Majority of the up to date computer aided design software have built in triangulation capabilities.

Once the triangulation is completed and fixed, exported .stl file should be sliced to be sent to the printer. Following the identification of the part's interior area by taking the opposite direction of the triangles' normals, related software generates the path that the laser will scan through during the process. Hence, sliced file mainly contains the laser scan path for each layer and layer thickness.

In this study, a complex surface model is generated in Matlab and exported in faced body format, then Unigraphics 12.0.4 (UG) is used for solid modelling of the faced body. Following the triangulation of the solid model, it slice file is generated and sent to the M2 Cusing machine for initiating the build job.

## **2.2 Additive Manufacturing and Preparation of Specimens**

Among the additive manufacturing modalities and hardware available, technology readiness level is the highest in powder bed fusion. Ability to manufacture small part features with high precision, resulting solid material integrity and reduced lead times make this modality very convenient for manufacturing micro, mezzo and macro scale lattice structures. Considering the advantages of manufacturing specimens of interest as well as the powder and machine availability, direct metal laser melting system is used in the study.

### **2.2.1 Direct metal laser melting**

Specimens are additively manufactured in Concept Laser M2 Cusing machine (see Figure 2.2). M2 Cusing is a direct metal laser melting machine containing 2 x 400 W fiber laser system. The build envelope's dimensions are 250 x 250 x 350 mm<sup>3</sup> in x, y and z axis, relatively. The layer thickness can be adjusted in between 20 to 80  $\mu\text{m}$ . The focus diameter of the lasers is 50  $\mu\text{m}$  with an optional variable focus move ranging from 50 to 500  $\mu\text{m}$ . The maximum scan scan speed available is 7 m/s and 4.5 m/s for variable focus move. The machine supports 2 separate inert gas supplies.

In the manufacturing of specimens, slicing is performed with 50  $\mu\text{m}$  of slice thickness which directly defines the layer thickness of the process. N<sub>2</sub> is used as the protective gas for shielding the laser melting process. The rest of the process parameters are determined by a comprehensive series of previous studies and set to obtain the minimum porosity.

HS188 powder with spherical morphology is used. Specialized HS188 powder for powder bed additive manufacturing systems are not wide-spread and parameter sets for processing this material is found not to be commercially available. Acceptable powder size distribution of the Concept Laser M2 is recommended to be in the interval of 10-70  $\mu\text{m}$ .



**Figure 2.2** : Concept Laser M2 Cusing (URL-7).

### **2.2.2 Preperation of specimens**

Following the completion of the process, specimens are welded to a steel plate and all of the process chamber is completely filled with powder. This powder is required to be evacuated from the chamber and the parts must be cleaned of powder residues. Brushes and vacuum cleaners are employed for initial cleaning. However, due to the rough surface characteristics of the printed parts and small size of the powder particles, powder residues are left on most of the surfaces and in small cavities of which especially exist in smaller unit cell size specimens.

Solukon<sup>®</sup> Powder Evacuation system is used for cleaning the powder (see in Figure 2.3). It is a closed unit for evacuating and thus cleaning the powder residues left in additively manufactured parts by vibration and manual compressed air blowing. It should be remarked that lattice structures especially with small unit cell sizes imposes a concern for powder cleaning since it is harder for the powder particles to mobilize when they are trapped in small cavities. In the 6, 8 and 12 mm unit cell size specimens of this study, cavities were sufficiently large to enable the powder to be removed. Cleanness is evaluated visually by holding the specimens against light since light was visible through the specimens in all directions.



**Figure 2.3 :** Solukon® Powder Evacuation System (URL-8).

After the powder is cleaned, specimens must be removed from the build plate. For this operation, KlaeGER® Bitron300 3D Cut band saw is used (see Figure 2.4). It is a continuous band saw system specialized for part removal from various sized build plates. Band saw's blade thickness is considered when the breakaway support structure is being designed. Following the cutting operation of the specimens, these breakaway supports are removed from the structure manually by using a chisel and a hammer.



**Figure 2.4 :** KlaeGER® Bitron300 3D Cut band saw (URL-9).

### 2.3 Characterization

Since it is expected and desired for lattice structures, mechanical properties of the double gyroid structures are determined by the material used, process variables and lattice design. The choice of characterization methods is based on the method's ability to identify the build errors, design and material properties as well as hardware availability. The relationship between the material, design and mechanical properties of the resulting structure is desired to be documented. In the scope of this study, the most suitable methods available to characterize DG lattices are chosen and described below.

During the manufacturing of specimens, four specimens are modelled with the same design parameters. Three of these are used in compression testing to ensure the statistical conformity and repeatability of the process. One specimen is considered as a “witness specimen” to be examined non-destructively and destructively upon sample preparation.

The samples are prepared with the following process steps as can be seen in Figure 2.5: each cube is cut by using Struers Secotom<sup>®</sup> first parallel to the build direction and then one of the pieces again cut in two, perpendicular to the build direction. One of the pieces is used to observe the microstructure in Z-Y plane whereas the other piece is employed to observe in X-Y plane. Afterwards, pieces are mounted in Struers CitoPress<sup>®</sup> mounting machine by using Struers MultiFast<sup>®</sup> bakelite. Molded pieces are grinded and then polished in multiple steps in Struers Tegramin<sup>®</sup> sample preparation machine (see Figure 2.6 and Figure 2.7). After cleaning the molds with isopropyl alcohol, specimens are ready for microscopic examination. Although there some regions in the molds where bakelite powder is failed to reach due to specimens with small unit cell sizes during molding, cross-sections are visible therefore decided to be used as is.

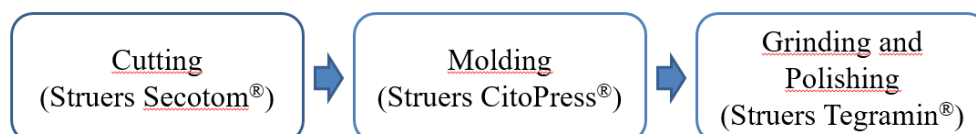


**Figure 2.5 :** Metallographic preparation steps.



**Figure 2.6 :** Struers Secotom® (URL-10).



**Figure 2.7 :** Struers CitoPress® (left) (URL-11) and Tegramin® (right) (URL-12).

Besides the optical imaging of the specimen, all the remaining methods are destructive. As very complex structures, lattices are in great need for structure specific characterization methods including non-destructive methods.

### 2.3.1 Compression test

Lattice structures have recently been started to be investigated for their mechanical properties to understand how they behave under certain loading conditions. As it is previously mentioned, design parameters of lattices such as unit cell types and geometrical aspects are found to have significant effect on the collapse mechanisms of lattices. Fundamental mechanical properties such as yield stress, ultimate stress and energy absorption prior to densification and elasticity modulus of lattice structures are required to be documented for design assessments. In the scope of characterizing the mechanical properties of DG structure for proposing it in aforementioned engineering applications, the compression behavior is chosen to be inspected. For compression testing, Shimadzu ag-ic 100kN® compression test device is used (see Figure 2.8). 100

kN upper force boundary represented a constraint for the size and volume ratio of the specimens. Compression test is recorded by Sony Alpha a6000<sup>®</sup> mirrorless camera with 60 fps and footage is used for examining compression characteristics at different strain levels.



**Figure 2.8** : Shimadzu ag-ic 100kN<sup>®</sup> compression test device (URL-13).

### **2.3.2 Stereo microscope**

Stereo microscope is an optical magnifying device which contains two separate optical paths with lenses to magnify objects with three dimensional features. Light is reflected from the surface instead of transmitting through it. Stereo microscope is mainly used for low magnification but high depth of focus requiring tasks. For characterizing the additively manufactured lattice structures, stereo microscope plays a critical role for examining the surface topology, satellite powders, open-to-surface defects and build orientation related features on the surface.

### **2.3.3 Inverted microscope**

Inverted microscope is used for higher level of magnification requiring tasks. Sample is placed on to a multi axis moving platform which is positioned above the changeable microscope lenses. Light is transmitted from below and reflected from the surface for illumination. Due to the high levels of magnification and wide aperture opening, depth of focus is very narrow. This requires the sample to be perfectly levelled and results in imaging only in two dimension.

Microscope used in the micro metallurgical examinations is Nikon Eclipse MA200<sup>®</sup> inverted light microscope with lenses to magnification factors of 50x, 100x, 200x, 500x, 1000x and 1500x (see Figure 2.9).



**Figure 2.9** : MA200<sup>®</sup> inverted light microscope (URL-14).

### **2.3.3.1 Microstructure**

The microstructure of additively manufactured HS188 is mainly inspected in the inverted microscope. It is chosen to examine the surface topology from cross-section, microstructural features such as grain formation, crystallization patterns, phase formations and additive manufacturing defects such as lack of fusion, gas porosity, down facing surface hang-overs. For capturing different unit cell sizes and microstructural aspects, different levels of magnification are used.

### **2.3.3.2 Porosity**

One of the major concerns about material integrity is the remaining porosity of DMLM parts. Porosity may occur during the process because of melting and solidification mechanisms. Gas generation in the melt pool, poor wetting or penetration in between the layers and laser passes, lack of fusion, deformations caused by residual stresses are considered as the main reasons for porosity (Vaezi et al., 2013). The porosity plays a critical role in the obtained mechanical properties of the additively manufactured parts. Hence, porosity inspection is very critical for characterizing both the process and material conformity.

Polished and cleaned samples are examined by the inverted microscope for type, size, ratio and distribution of porosities. The total amount of porosity cannot be measured since in any of the magnification levels the thin surface of DG does not allow a porosity measurement compliant with the investigated specs. Literature unfortunately lacks an appropriate standard specification for measuring porosity in lattice structures.

### **2.3.4 Optical 3D micro measurement**

Another important characteristics of additive manufacturing is varying surface roughness upon build orientation. Traditionally, there are various methods specified for measuring the roughness of the surface. However, these measurements require a flat surface to measure the roughness on to comply with specifications. In lattice structures and especially in gyroid surface model, there are no flat regions to perform such measurements. Since it is well known that surface quality is a significant factor in defining surface properties, mechanical properties and failure mechanisms of additively manufactured structures, the roughness measurement on the curved surfaces is performed for further characterizing the specimens.

3D optical micro measurement machine named InfiniteFocus by the company Alicona is used for optical roughness and surface topology measurements (See Figure 2.10). The device is armed with 8 interchangeable lenses with magnification factors of 25x, 50x, 100x, 200x, 500x and 1000x. It offers surface modelling by 3D scanned data through the lenses with a significant resolution. After the curve surfaces are scanned and modelled, scanned model is best fitted with the CAD model in GOM® software to evaluate the geometrical differences in between CAD model and the manufactured part. This gives an important insight on topologies of different surfaces and edges of the DG lattice structure.



**Figure 2.10 :** Alicona InfiniteFocus (URL-15).

### **2.3.5 Scanning electron microscope**

Optic and electronic systems with high magnification are used in scanning electron microscopy (SEM), together. When examining the working principle of SEM, the electrons which were accelerated by high voltage have a significant role to obtain micrographs.

First of all, these electrons are focalized on the surface of specimen. After that, these electrons and electrons of specimen are interacted between them. These interactions are transformed to digital signals and these digital signals are transferred on the screen of computer.





### **3. EXPERIMENTAL PROCEDURE**

In this chapter, the design of the experimental work, details of execution and challenges experienced through specimen modelling and manufacturing of the specimens are explained. Although there are several sources available on modelling of triply periodic minimal surfaces and double gyroid solid model in the open literature, dimensional and gravimetric accuracy of the manufactured specimens are not documented sufficiently. Following the first trials during the study, error factors are identified in both modelling and manufacturing of specimens. In order to obtain an acceptable level of accuracy in the resulting specimens, multiple modelling approaches and build trials are performed prior to testing and documented in this chapter.

#### **3.1 Design of Experimental Work**

Compression testing on DG specimens having different design parameters is performed for examining mechanical characteristics of DG structure. Besides the compression testing, understanding the design methodology, manufacturability and resulting geometry is required. Using aforementioned characterization techniques, manufactured specimens are investigated before and after compression testing both by destructive and non-destructive methods.

##### **3.1.1 Specimen design**

The design of a double gyroid (DG) structure can be manipulated by the thickness of the surface that is defined by the DG's equation and the unit cell size. The volume fraction (VF) is the ratio of volume of the solid and the volume of the enclosing cube. The purpose of this study is to understand the effect of unit cell size on the compression behavior of the resulting structure. Hence, unit cell size is changed and the thickness is changed accordingly to keep VF constant.

There are two major constraints that limit the upper and lower boundaries of the unit cell size of a gyroid lattice structure from manufacturing process perspective: smallest gap size and maximum allowable radius of unsupported regions. As the unit cell size

gets smaller, the void in between the surfaces gets narrower and approaches to the value of smallest void that is possible to be manufactured by additive manufacturing process of interest. Additionally, hangovers on down facing surfaces and satellite powder residues tend to fill the void in between the surfaces. These aspects define the lower boundary of the unit cell size. On the other side, as the unit cell size gets higher, the average radius of the gyroid gets higher and its unsupported down facing surface cannot be built with acceptable dimensions and surface profile.

The gyroid has a cubic unit cell so the geometry of sample coupon is also decided to be a cube since the unit cell is required to fully repeat itself in all dimensions. This ensures that unit cell size is the major effecting parameter on the compression test results. This way, results of the study is also comparable with the examples of previous studies (I. Maskery, Aboulkhair, et al., 2017). The sample cube dimension is determined to be 24x24x24 mm because the number of integers which can divide 24 is highest. The unit cell size is to be determined among the following sizes in millimeters for complete unit cell repeatability since all these values are divider integers of 24: 1, 2, 3, 4, 6, 8, 12, 24.

### **3.1.1.1 Preliminary modeling trial basic surface modeling**

The techniques for modeling of gyroid structures are investigated and reviewed in the work of Monkova, K. *et al.* (Monkova, Monka, Zetkova, Hanzl, & Mandulak, 2017). There are three methods described in that study. First, basic surface modeling is proposed. One-eighth of a gyroid unit cell is modeled and multiplied according to the mirror and symmetry operations deducted by the space group representation. Second model is using gyroid's mathematical function to define and model the surface in an appropriate software such as Matlab. Third is to model the interconnected network of helices to represent the voids in DG structure. The preliminary modeling attempt in this is inspired by the first method described in their study.

As it was mentioned before, gyroid's cubic space group is identified as I a-3d (Luzzati, V., Spegt, 1967; Scientific & Scientific, 1981) (see Figure 3.1) . In UG, the edge of the sub-element of a single gyroid unit cell is generated by using ten of two dimensional sketches. By connecting the lines which represent the edges with the built-in surface generation tool in UG, surfaces are generated. Then, by performing the

related symmetry and mirroring operations of the symmetry group, sub-element can be multiplied and stitched together to represent a complete gyroid unit cell.

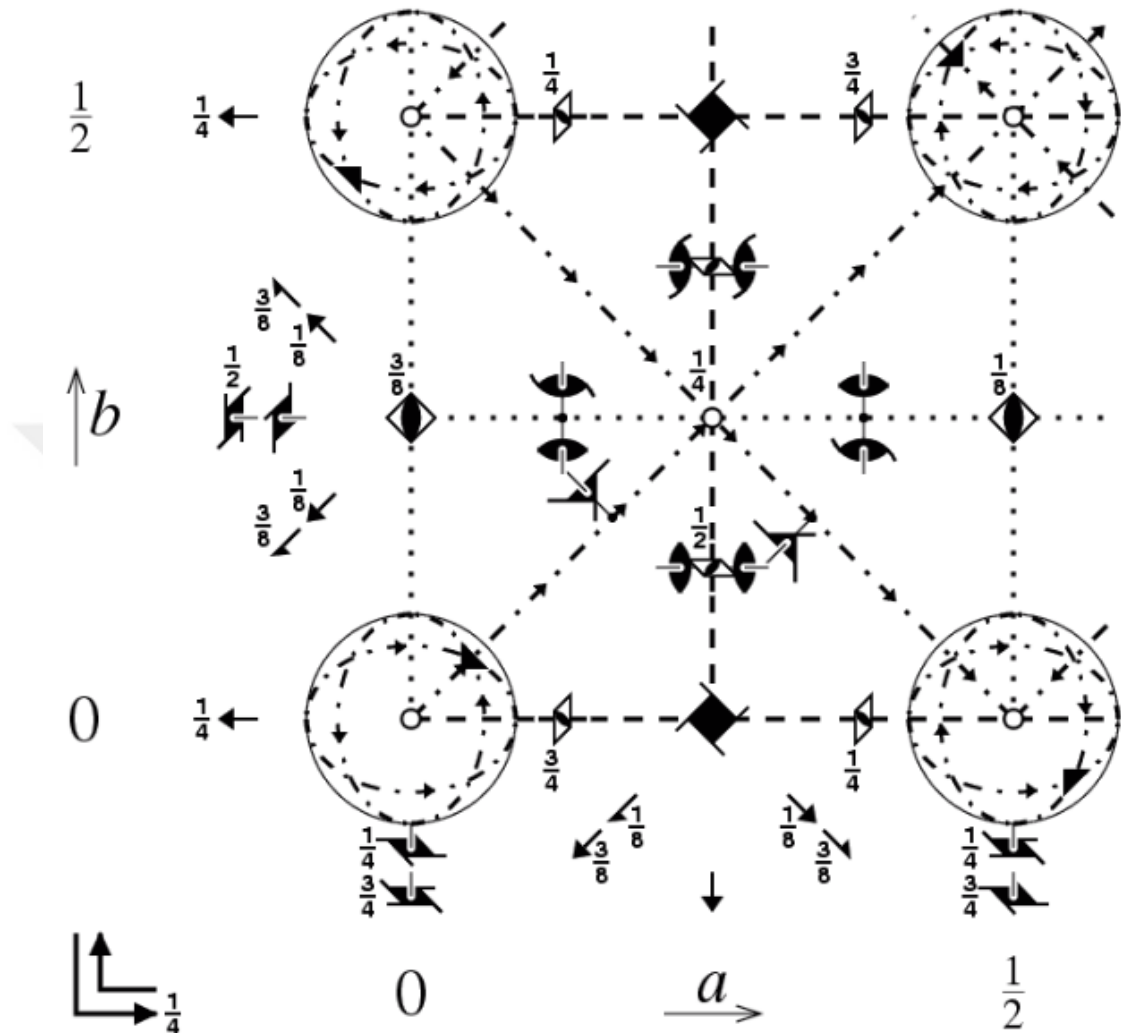


**Figure 3.1** : Space group representation of I a-3d (URL-15).

Although that the model appears to comply with the desired gyroid geometry at the outset, there are discontinuities found in between the sub-elements in a further examination.). As it can be seen in Figure 3.2, four half circles and two complete circles in the left image should have been completely circular. However, in the resulting structure, they are closer to being rectangular rather than circular. Two causes are identified for explaining these defects. First, the arcs which creates the edge representing lines could not be drawn in compliance with the mathematical function of the surface model. Secondly, built in surface generating function used in UG is principally an interpolation function which uses the enclosing lines as references to

create the surface. Thus, largely based on the UG’s surface generation function, resulting surfaces are found not to sufficiently align with the desired gyroid surface.

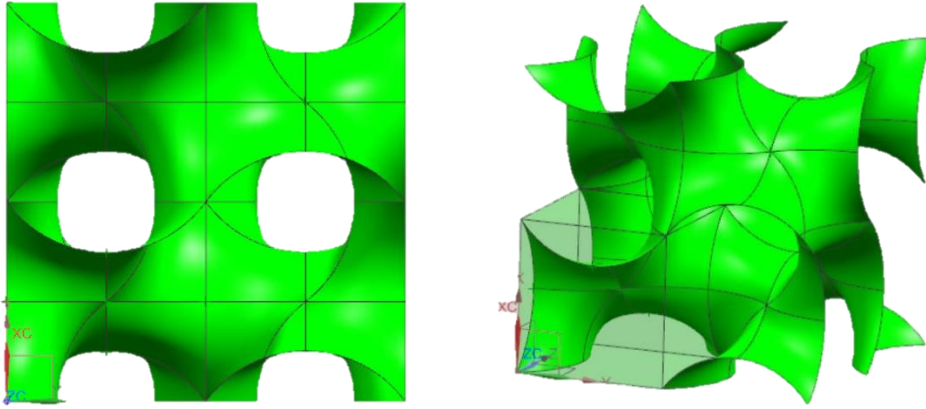


**Figure 3.2** : Manually drawn gyroid surface trial

### 3.1.1.2 The second modeling trial based on mathematical surface definition

In order to generate all the surfaces without any continuity error, whole surface of the unit cell is decided to be modelled by using the mathematical approximation formula of the gyroid structure as given in Equation 3.1. The function is generated in Matlab in the scope of this study and the surface is created by using embedded “isosurface” function. Since the specimen sizes and number of repetitive unit cells are known, complete surface model of each specimen is generated by this approach. Complete modeling of the specimens is found to be very favorable in terms of computation time for the ease of following operations performed in UG.

$$U = (\cos(k_x x) \sin(k_y y) + \cos(k_y y) \sin(k_z z) + \cos(k_z z) \sin(k_x x))^2 - t^2 \quad (3.1)$$

The Matlab code used to generate the gyroid surfaces is given in Figure 3.3. Variables defined as “n” is the number of unit cells in X, Y and Z directions and “l” is the length unit of each unit cell. In the function, value “t” describes the thickness of the DG’s model. This value is set to 0 since Matlab is not used for solid model generation, only used for two-dimensional surface model generation. The given code generates the specimen point cloud surface model with 12 mm unit cells. The resulting of this code can be seen in Figure 3.4. As it can be seen, the voids in the structure closely approximates to being circular as opposed to the voids of the preliminary trial.

```

n = 2 ;
l = 12;
zr = n*l;
n = [n n n];
le = [zr zr zr ];
k = 2*pi*n./le ;
t= 0 ;
[x,y,z] = meshgrid(linspace(0,zr,100), linspace(0,zr,100), linspace(0,zr,100));
f=@(x,y,z) (cos(k(1).*x).*sin(k(2).*y)+cos(k(2).*y).*sin(k(3).*z)+
cos(k(3).*z).*sin(k(1).*x)).^1-t^2;
as = f(x,y,z);
fv = isosurface(x,y,z,as)
stlwrite('12_24.stl',fv)

```

**Figure 3.3 :** Matlab code used to generate gyroid surface model.

The conversion of the surface from point cloud into convergent faced body in stl format is required to be able to add thickness to the surface in CAD software. A publicly available STL generation library is added to Matlab for this operation. To perform “stlwrite” function, first the space that the point cloud occupies must be discretized. This function uses the nodes of the meshed space as references for triangulating the surface. As it can be seen in the Matlab code, function “meshgrid” is used with “linspace” function for the discretization of the space with meshes separated by nodes. For the number of nodes in one dimension the value of 100 is used, resulting in total number of  $100^3$  cells for each specimen’s surface model. This value directly defines the resolution of the faced body. In order to have a manageable triangulated model size without requiring a very high performance computer hardware to perform solid modelling operations in UG, number of nodes in each direction is chosen to be 100 for faced body generation.

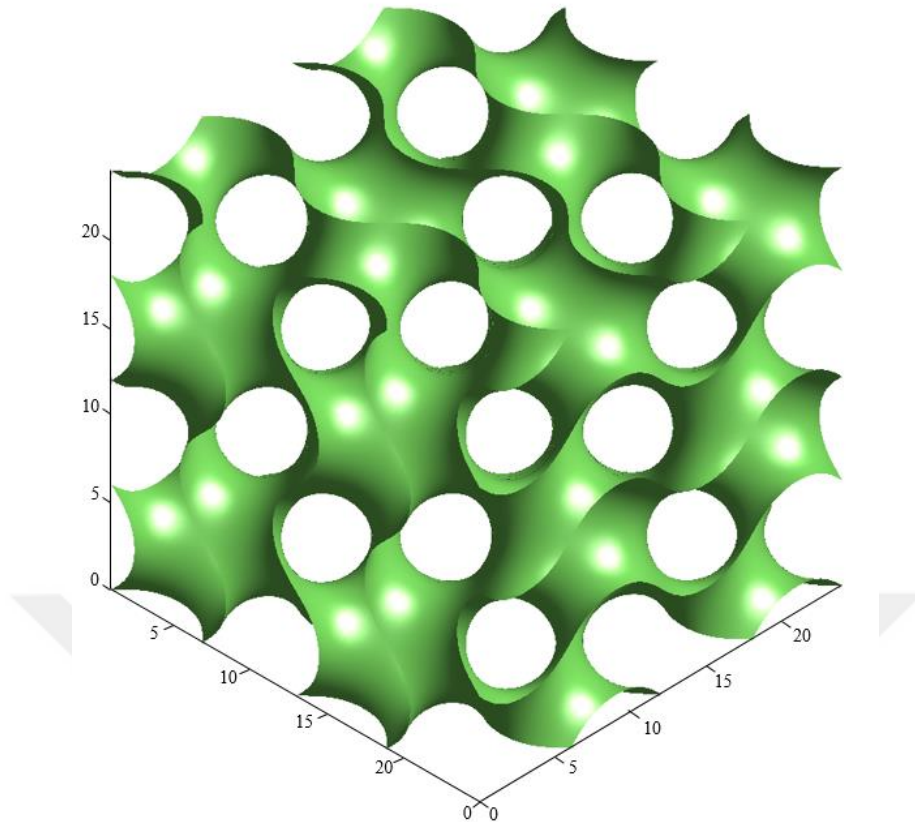


**Figure 3.4 :** Surface representation in Matlab.

After the faced body export in .stl format from Matlab, the file is imported to UG as convergent as seen in Figure 3.5. Due to the complexity of the model, UG fails to perform all of the surface modification or solid body generation functions to create the DG solid model. Therefore, an alternative approach is followed.

First, “Smooth faced body” function is performed on all of the triangles on the convergent body in order to circularize the sharp edges (see Figure 3.6 a). This enables the “offset” surface function. Then, the faced surface is given offset in both directions. The offset value is set to the half of the desired thickness of DG (see Figure 3.6 b). Later, a block is created by 24x24x24 mm and placed in the exact area that the DG model occupies. Offset surface edges extended by “extend edge” function in order to have them going out of the block’s surfaces (see Figure 3.6 c). Lastly, the solid block is trimmed by using both of the offset surfaces as a guide. The volume in between the offset surfaces can now be obtained as solid as depicted in Figure 3.6 c.

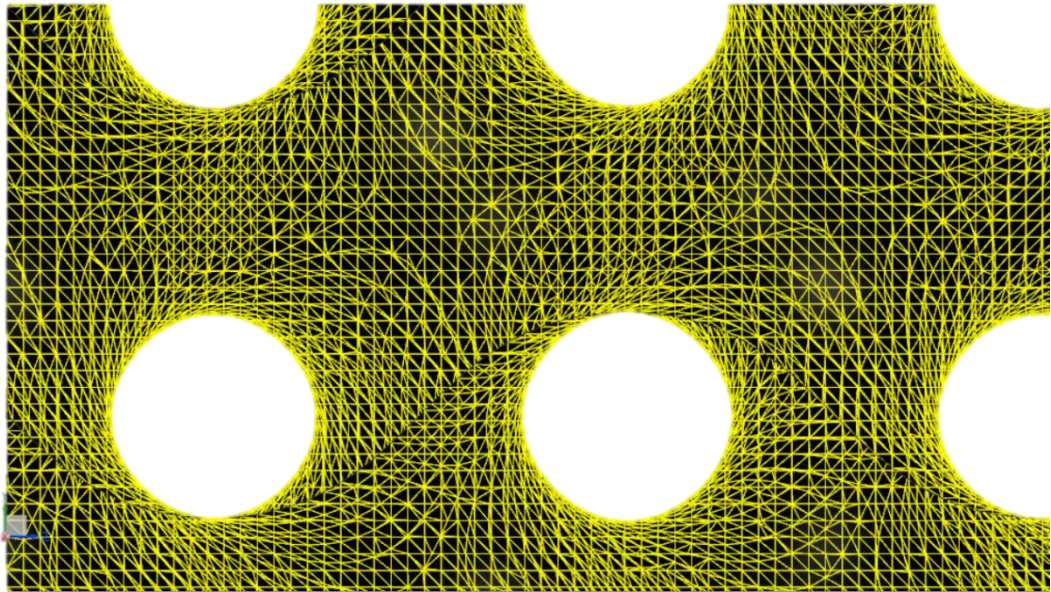


**Figure 3.5 :** Triangulated surface detail of gyroid as extracted from Matlab.

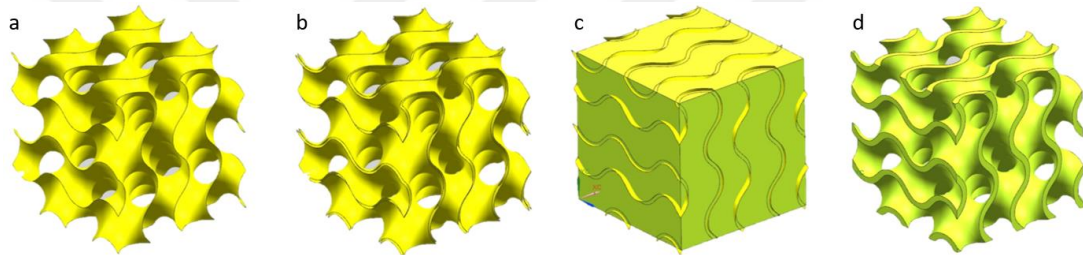


**Figure 3.6 :** DG modelling steps in UG.

### 3.1.2 Manufacturing of specimens

For additively manufacturing of the gyroid specimens, two challenges are identified which are not addressed in the literature: 1) volume to wall thickness ratio for  $VF=20\%$  and 2) the offset between the CAD and the printed part. Volume to wall thickness ratio is found to be special for each  $VF$  value and may be documented by conducting experimental trials in the CAD software. These trials consist of changing the thickness of the surface model gradually and documenting the resulting volume. However, the offset between the CAD and the printed part is directly process- and material-dependent and is required to be identified by manufacturing and measuring the specimens.

According to the preliminary assessments,  $VF$  is a parameter for unit cell size-wall thickness relationship. Therefore,  $20\%$   $VF$  is aimed and fixed for the function generation of solid volume. By conducting multiple experiments on the solid model,

volume & unit cell size plot is obtained and empirical function of the curve is documented with an approximate trend line by  $R^2=0.9998$ .

$$y = 0.0667x \tag{3.2}$$

The function found defines the desired volume (represented by “y” in the Equation 3.2) for each thickness (represented by “x” in the Equation 3.2) for each desired volume with a level of accuracy as high as >99.8% for VF=20%. Relationship of thickness and cell size is given in Figure 3.7 for constant V.

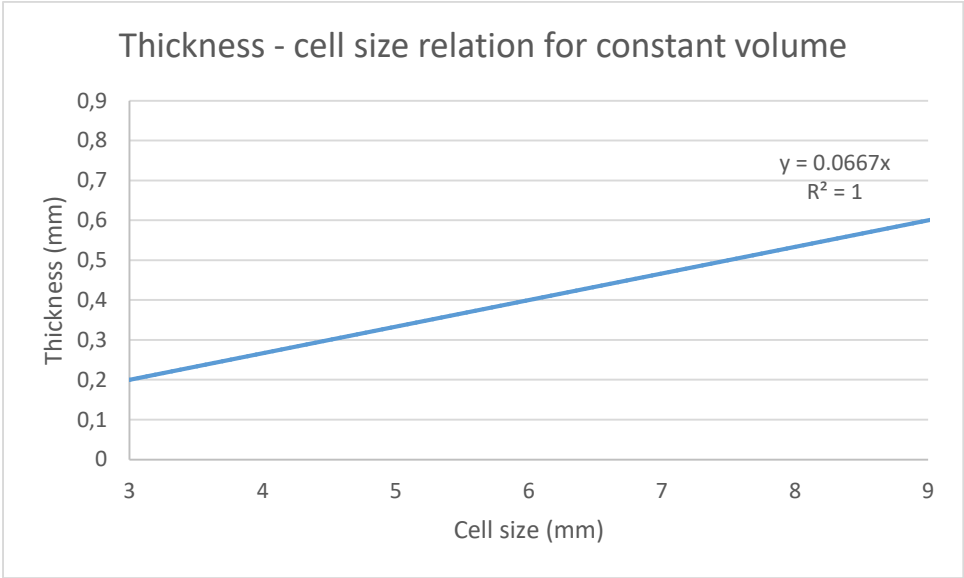


**Figure 3.7 :** Thickness vs cell size relation for constant volume.

Leveraging from this equation, specimen designs are primarily completed with the values in Table 3.1.

**Table 3.1 :** Theoretical specimen values.

Unit cell size (mm)	thickness (mm)	Volume (mm <sup>3</sup> )	Cell count	Volume fraction	Surface area (mm <sup>2</sup> )
3	0.2	2817.29	512	0.20	28516
4	0.267	2826.06	216	0.20	21250
6	0.4	2829	96	0.20	14648
8	0.533	2830.37	27	0.20	10496
12	0.8	2830	8	0.20	7596

With these values, first 3 specimens are manufactured with the unitcell sizes 3, 4 and 8 mm. Measured values can be seen in Table .2.

**Table 3.2 :** Measured first manufactured specimen values.

Unitcell size (mm)	Weight (g)	Solid volume (mm <sup>3</sup> )	Specimen cube volume (cm <sup>3</sup> )	Relative density	VF (%)	VF change (%)
3	55	6125	13.824	3.98	44.30	117.40
4	48	5345	13.824	3.47	38.67	89.14
8	36	4009	13.824	2.60	29.00	41.64

On the right most column of Table , VF difference between the CAD models and printed parts are given. These differences are concluded to be directly affected by the unit cell size of each specimen. In order to correct the VF difference in manufactured parts, debit offset for the wall thicknesses is decided to be defined. For each unit cell size, VF change differs. Since the 6 and 12 mm unit cell sized specimens are not manufactured, a prediction is required for the VF change.

For this purpose, plot seen on Figure 3.8 is generated. Data for the unit cell sizes 3, 4 and 8 mm already existed and a polynomial trend line is generated for predicted the VF change values for 6 and 12 mm unit cell sized specimens.

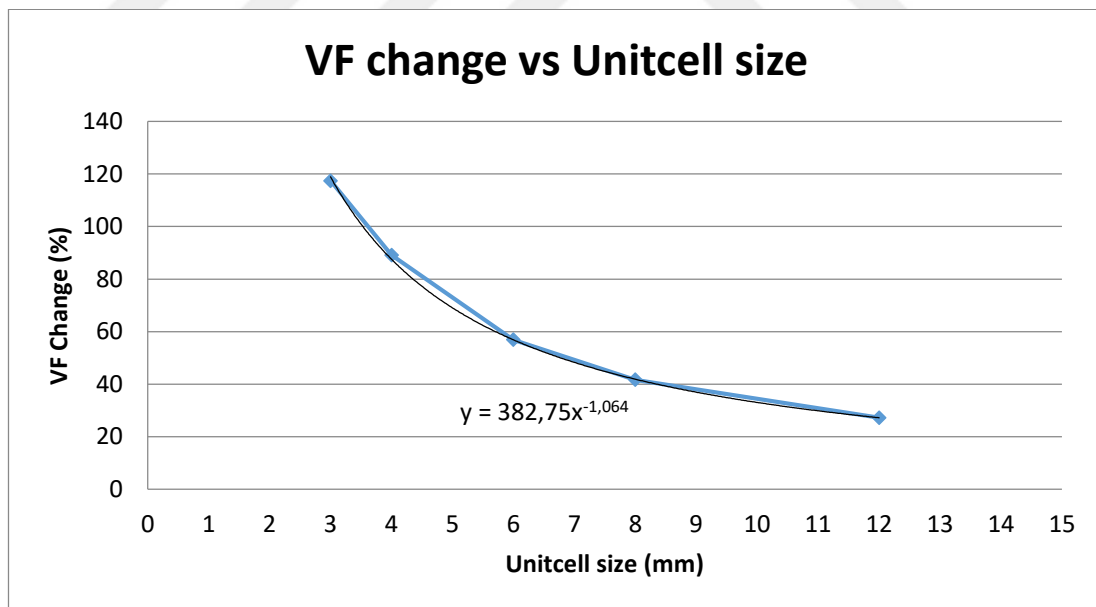


**Figure 3.8 :** VF change to unit cell size plot for prediction.

By using the predicted VF change values, 6, 8 and 12 mm specimens wall thicknesses were redesigned with offset and manufactured. Resulting specimen modelled and measured values can be seen in Table 3..

**Table 3.3** : Final specimen values from CAD model and measured after manufacturing.

Unitcell size (mm)	Weight (g)	Solid volume (mm <sup>3</sup> )	Relative density (g/cm <sup>3</sup> )	Volume Fraction(%)
6	29.96	3336	2.17	24.14
8	28.38	3161	2.05	22.86
12	26.95	3001	1.95	21.71

Accuracy enhancement in VF achieved by the wall thickness offset approach can also be seen in Figure 3.9 and Figure 3.10. In the secondary trial, resulting specimen solid volumes are significantly closer to the modelled volumes, in comparison to the preliminary trial.

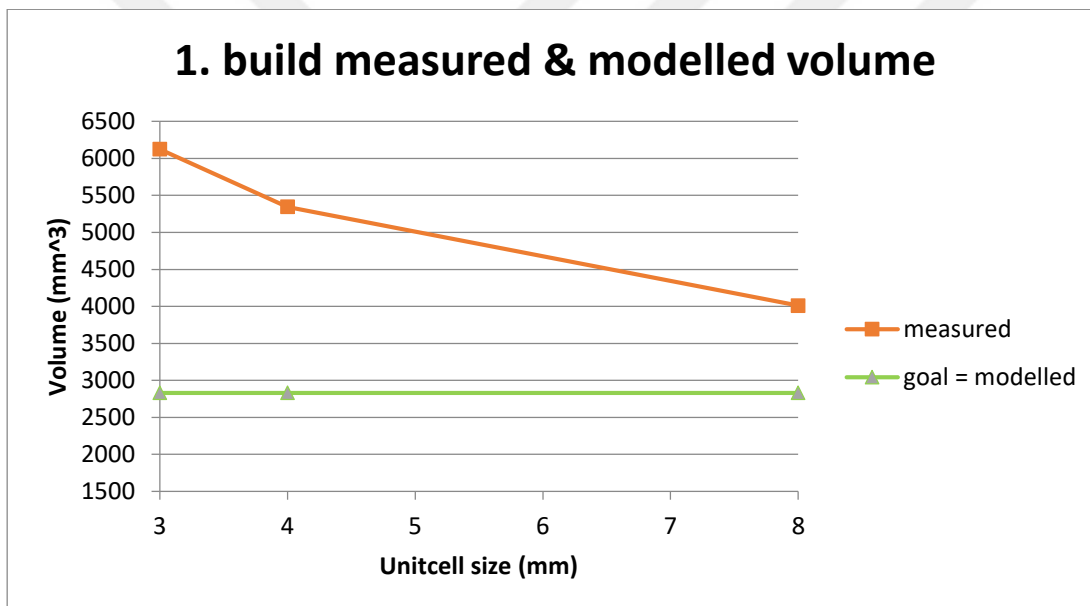


**Figure 3.9** : Preliminary trial measured versus modelled.

Resulting 6, 8 and 12 mm unit cell sized specimen close plan pictures can be seen in Figure 3.11 and Figure 3.12.

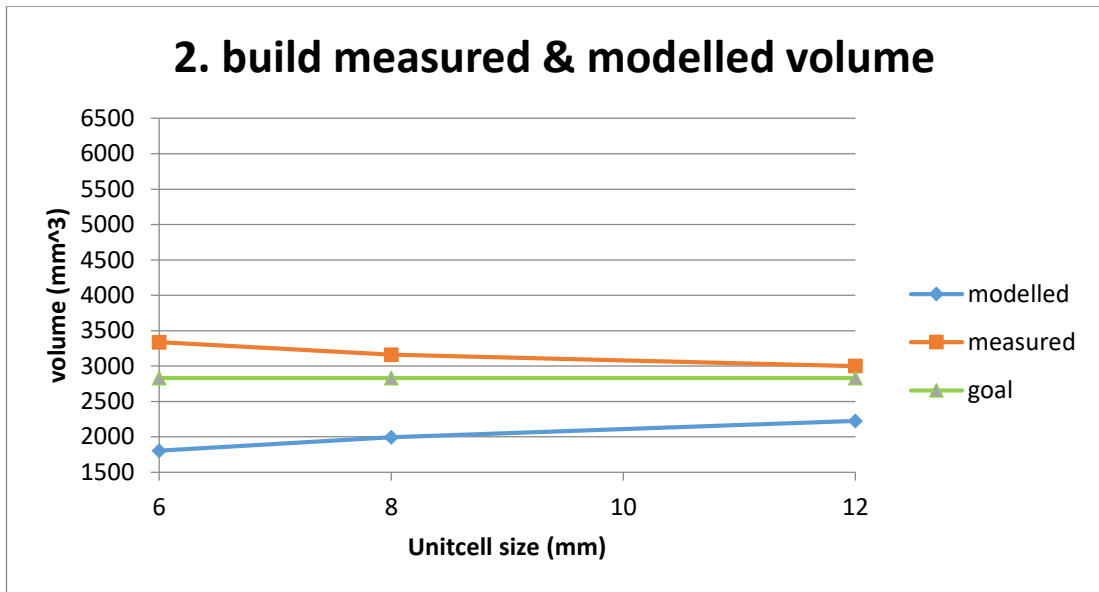


**Figure 3.10 :** Secondary trial measured versus modelled.

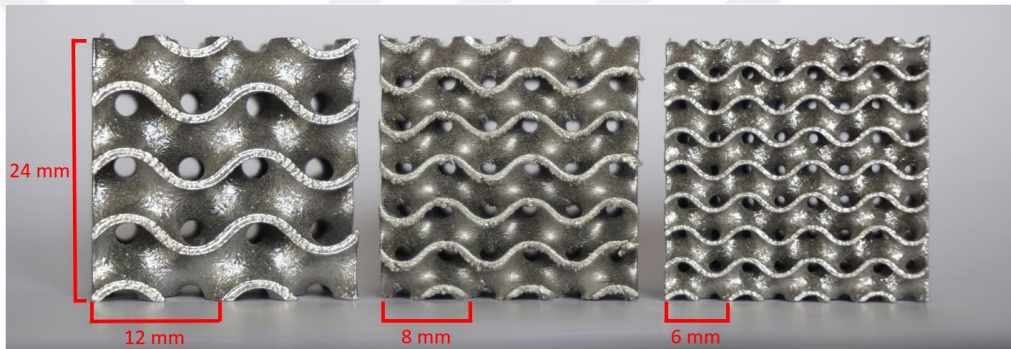


**Figure 3.11 :** Additively manufactured HS188 DG samples from left to right with 12, 8 and 6 mm unitcell sizes repectively.

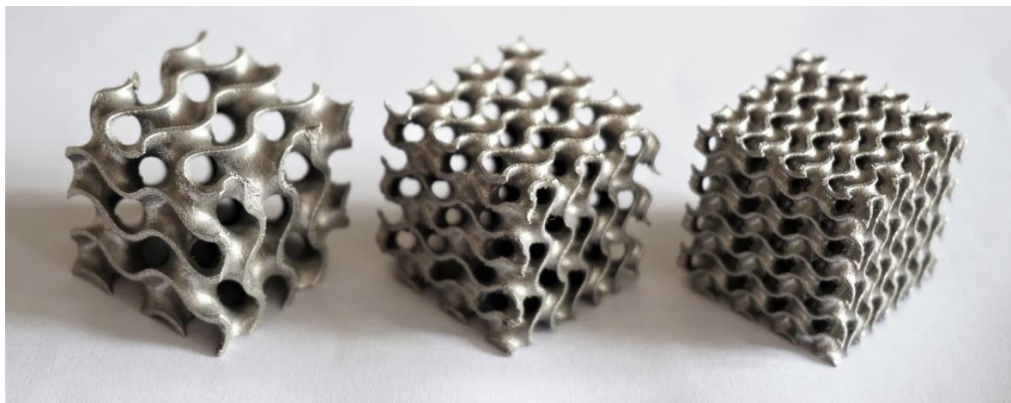


**Figure 3.12 :** Isometric view of additively manufactured HS188 DG samples from left to right with 12, 8 and 6 mm unit cell sizes.

### **3.2 Compression Testing**

The rate of compression in the compression testing is set to 1 mm per minute since it is the lowest strain rate available. Because of the test machine's highest loading capacity, the test is stopped as the load reaches the highest value of 10 kN. Each specimen is placed on the compression fixture in the build direction in order to avoid the effect of anisotropy. Test is recorded with a fixed camera in order to obtain in situ crashing footage.



## **4. RESULTS AND DISCUSSIONS**

### **4.1 Microstructure**

In this section, the results of the microstructural investigation of DG samples with 3, 4, 6, 8 and 12 mm unitcell sizes are presented. Wide area cross-section images of mounted samples are taken by 2D scan function of Alicona while close up images of defects are taken using the inverted light microscope. All samples are grinded and polished but not etched, unless it is indicated otherwise. Images have been oriented to have the build direction as down to up direction for the ease of understanding.

The wall thickness of the structures changes sinusoidally through all directions. Because of the complex shape of the DG structure, predicting the cut-up plane position is assumed to be almost impossible. Therefore, measuring the wall thickness in the grinded samples could not be correlated with any reference since exact position of the cut-up plane is unfortunately unknown. For this reason, the wall thickness is not measured in the following sample images. Owing to the same reason, each sample with different unit cell size has a different cross-section area which represents the varying sinusoidal geometry of DG structures.

Regarding the porosity, pores due to entrapment of gases in the melt pool can occur in very small (less than a micron in diameter) dimensions. These types of pores are very identical with their almost perfect spherical shapes and considered rather harmless owing to their small size and stress concentration favoring morphology. In the inverted microscope, they can be spotted with their light reflecting brighter center regions due to their sphericity.

#### **4.1.1 3mm unit cell size**

As it can be seen in Figure 4.1, Convex and concave down facing areas are two important areas in this section of the structure because the majority of the build defects are observed in these areas. DG structure is generally considered as a self-supporting structure without any discontinuity. However especially in specimens with smaller unit

sizes, there has been many overhang areas are observed. The dross formation on the overhang surfaces are mainly caused by the gravity acting on the melt pool and poor thermal conductivity of the underlying powder with respect to the one of the bulk material. Since there is insufficient solid interface in contact with the melt pool, thermal relief delays and enables the molten metal travel under the force of gravity towards the powder bed before solidification.



**Figure 4.1 :** 3mm unit cell paralel cross-section.

Above the overhang areas, significant void defects are observed. These voids are considered to be caused by the insufficient penetration of the next layers after the overhang due to the extended powder bed surface to solid part distance. After some number of layers in build direction, these voids disappear. As it can be seen in Figure 4.2, there is significant crack formation in the overhang regions where the heat dissipation could not be homogenous due to insufficient solid contact. As it can be

seen in Figure 4.3, in some concave areas there are residues of unmelted but partially sintered powder is visible.

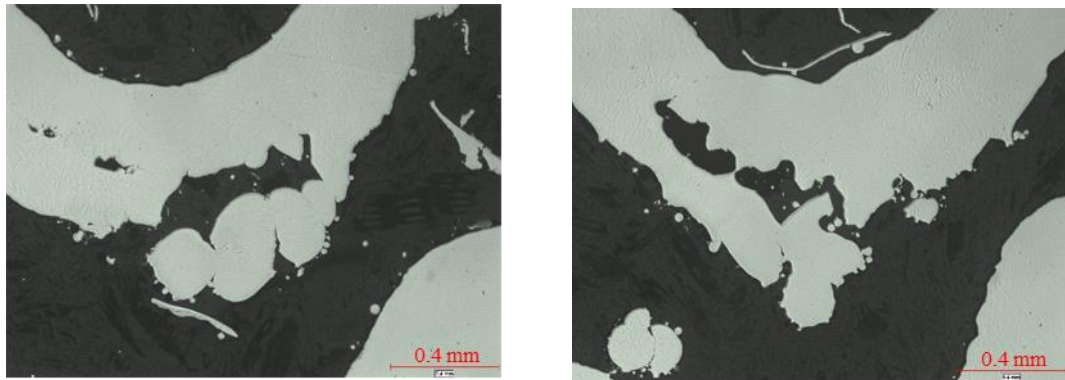


**Figure 4.2 :** 3 mm unit cell convex overhang surfaces.

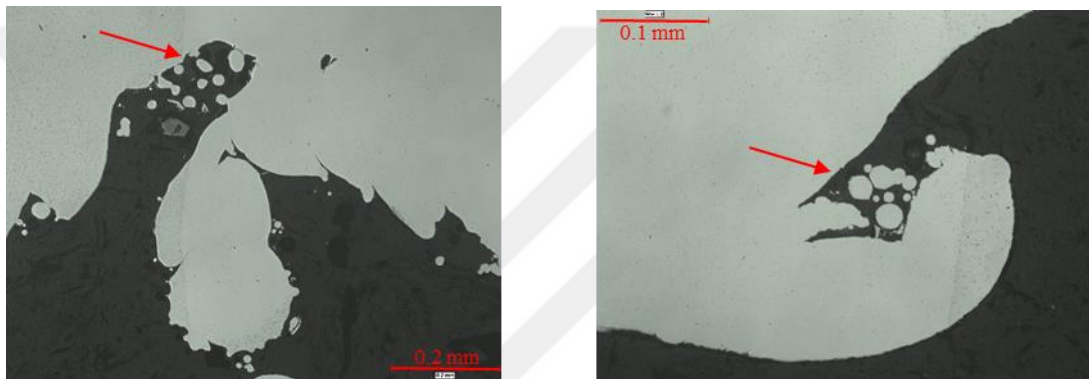


**Figure 4.3 :** 3 mm unit cell concave overhang surfaces.

#### 4.1.2 4 mm unit cell size

Cross-section in Figure 4.4, concave areas have separated from the structure. However, in the convex region, overhang surfaces which are accompanied by void defects are observed but they are not separate from the structure.

In Figure 4.5, the investigated cross-section has a normal parallel to the build direction. The visible voids are the areas where different surfaces are connecting. Due to the down facing surface characteristics, the transition of the surfaces is not smooth in this plane and it is seen as periodic defects.



**Figure 4.4 :** 4mm unit cell paralel cross-section.

As it is seen in Figure 4.6, convex down facing surfaces exhibit overhangs but not entirely torn away from the structure. The void defect formations above the overhangs more exist on the left side of the convex geometry. This is caused by the gyroid surface characteristics. Porosity difference in between the pictures of Figure 4.6 is mainly caused by the horizontality difference of two locations in DG. Also in Figure 4.6, solidification cracks are observed initiating from the lowest edge of the overhang surface and indicated with the red arrow. These crack formations are identical to those of Figure 4.2 and Figure 4.3.

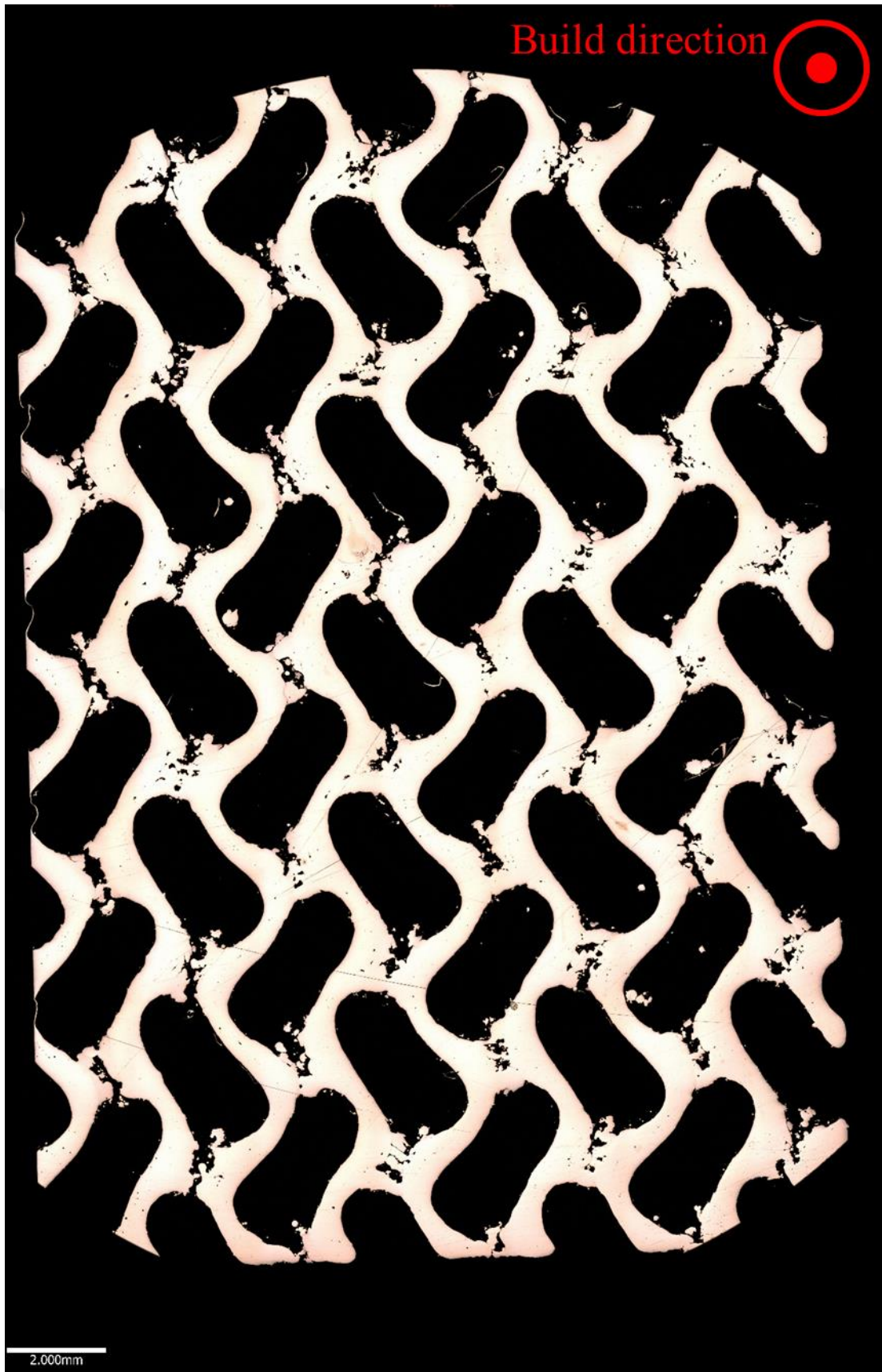


**Figure 4.5** : 4mm unit cell perpendicular cross-section.

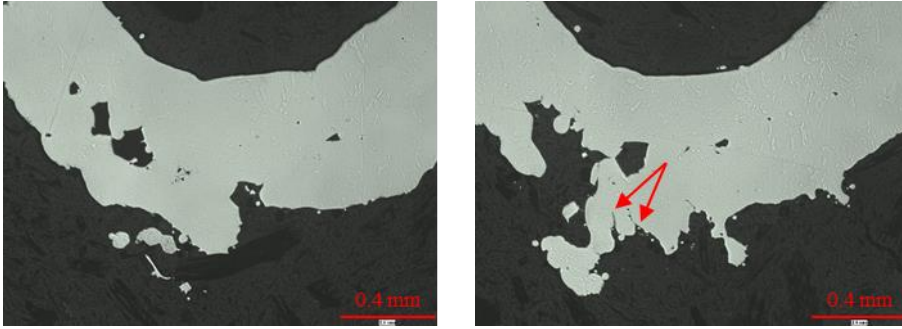


**Figure 4.6 :** 4mm unit cell convex overhangs.

In Figure 4.7 : **4 mm unit cell concave** , bulk part of the concave geometry has an indentation very similar to the shape of circular overhang standing separated from the structure. This similarity represents a significant evidence for the explanation of dropping overhang regions down after the adjacent upper layers are built. In the right hand side of Figure 4.7, the void above the hangover contains partially melted powder inside.

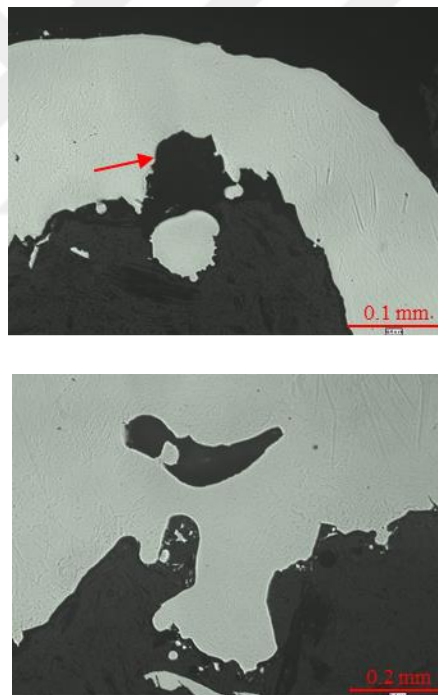


**Figure 4.7 :** 4 mm unit cell concave overhangs.

#### 4.1.3 6 mm unit cell size

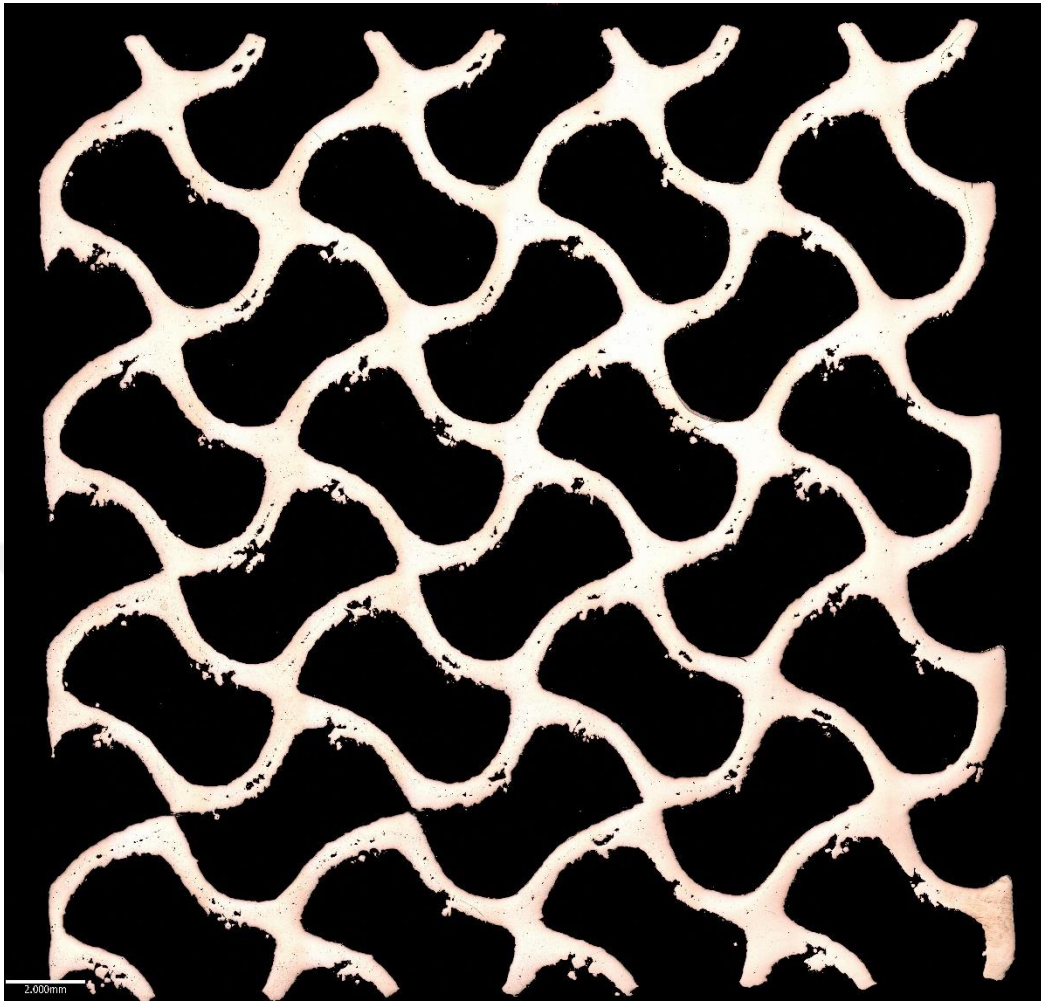


**Figure 4.8 :** 6mm unit cell paralel cross-section.

In 6 mm unit cell size, visible volume of the hangovers decreased significantly (see in Figure 4.8). An amount of hangover exists, and they cause the mid-plane aligned void defects. These void defects disappear after a short distance in Z direction. It is concluded that they are caused both by the down facing concave surface and hangover that disables the next layers to fuse properly with the previous ones.

As it can be seen in Figure 4.9, the surface roughness vary depending on the location as visible in the perpendicular cross-section. Surfaces tend to be rougher in down facing areas as expected. Mid-plane aligned voids are also visible and they correlate with the mid-plane void formations seen in Figure 4.8.

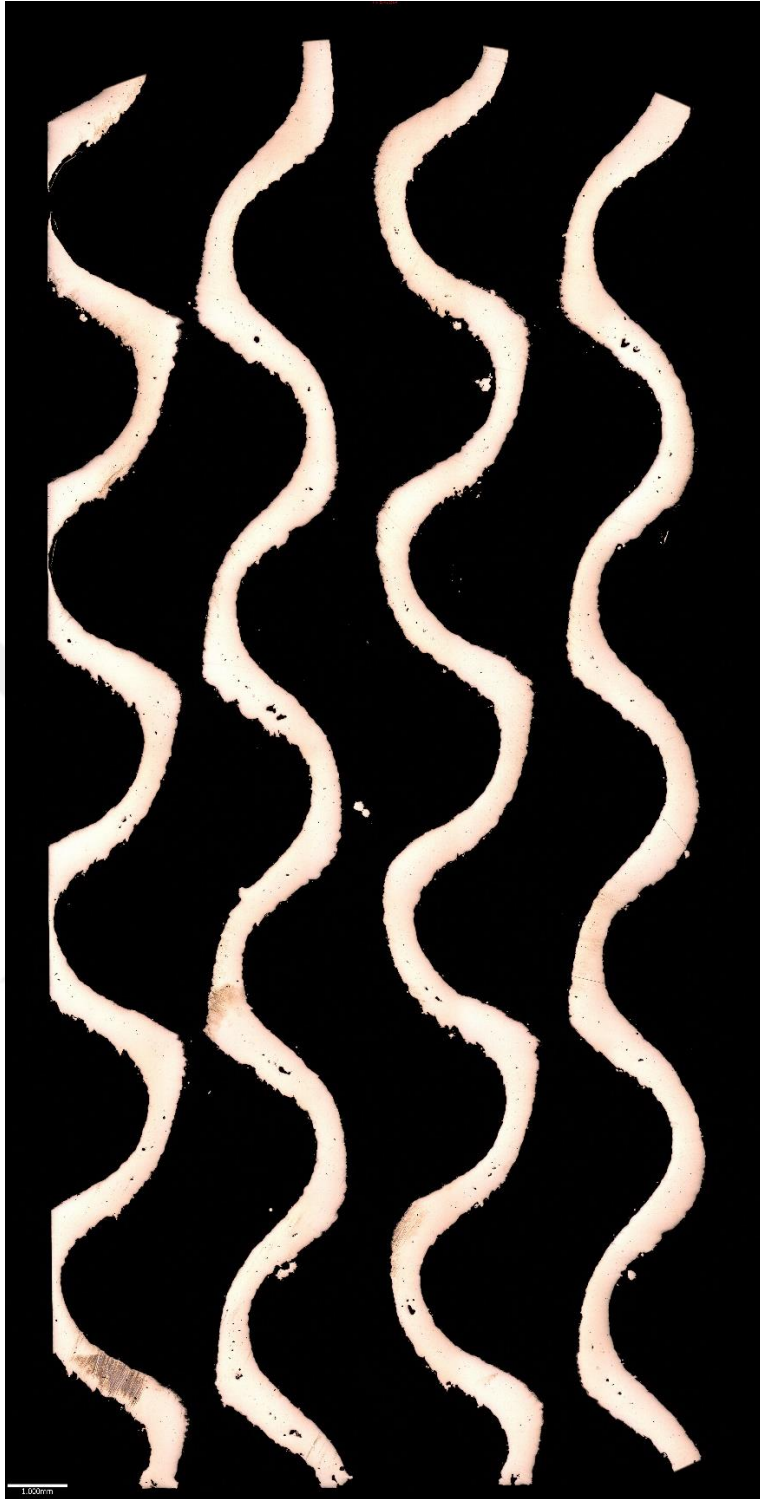


**Figure 4.9 :** 6mm unit cell perpendicular cross-section.

Formation of aforementioned mid-plane voids can be well observed in Figure 4.10.

As it can be seen in Figure 4.11; surface transition areas, side facing and up facing areas are mostly free of void defects except small gas pores. Furthermore, there are no separations from the overhang surfaces and no crack is observed.

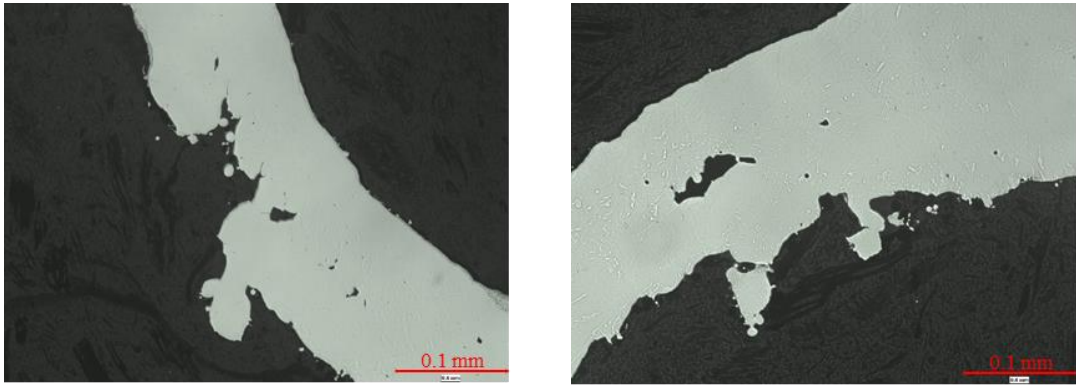


**Figure 4.10** : 6mm unit cell hangover areas.

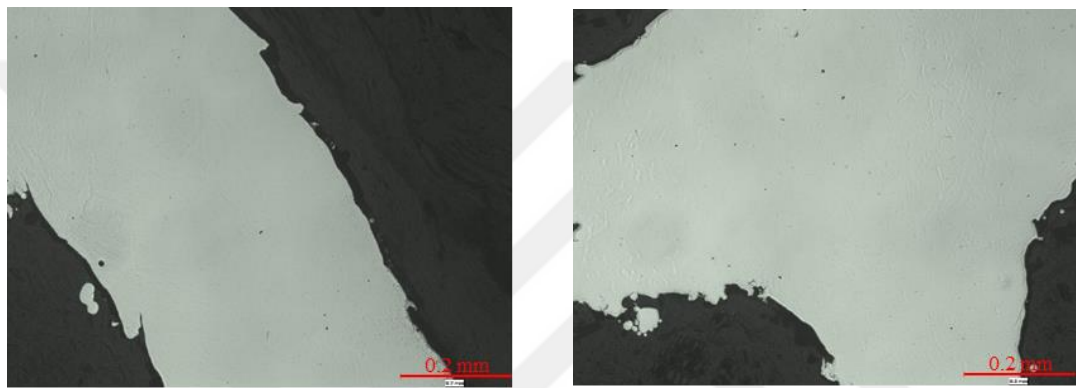


**Figure 4.11** : 6 mm unit cell less porous regions.

#### **4.1.4 8 mm unit cell size**

In the cross-sections given in Figure 4.12 and Figure 4.14, less porosity is observed near the surfaces. Although that it can be said that this enhancement is caused by the bigger unit cell size, it must be underlined that the given cross-sections might not be representative of the worst areas in the structure by the means of overhangs. In different cross-sections, more overhang features might be observed since the DG surface's angle with the build direction gradually changing over the build direction.

Figure 4.13, on the left, small satellite powders are observable. On the right side, very close to the most overhang area; inability to provide fusion of the melt pool to the previous layers can be seen.

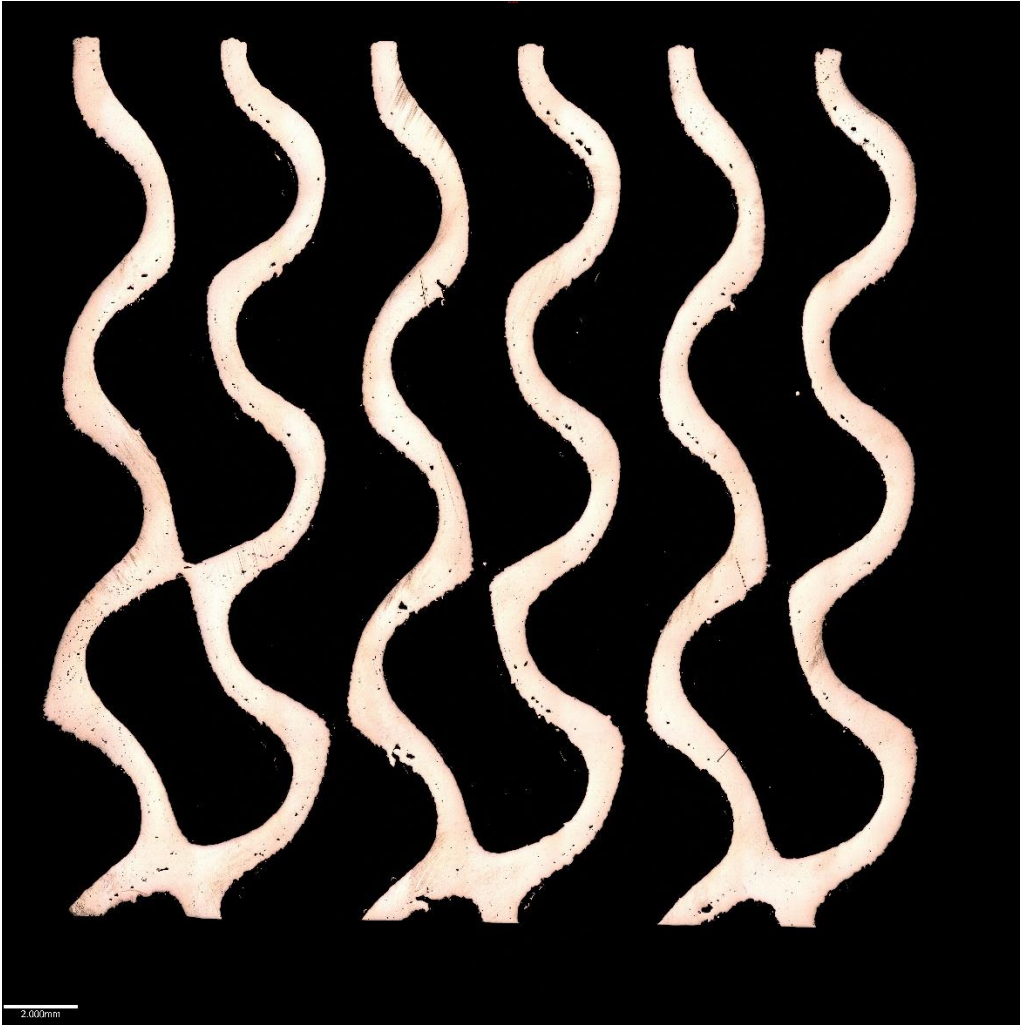


**Figure 4.12** : 8 mm unit cell paralel cross-section.

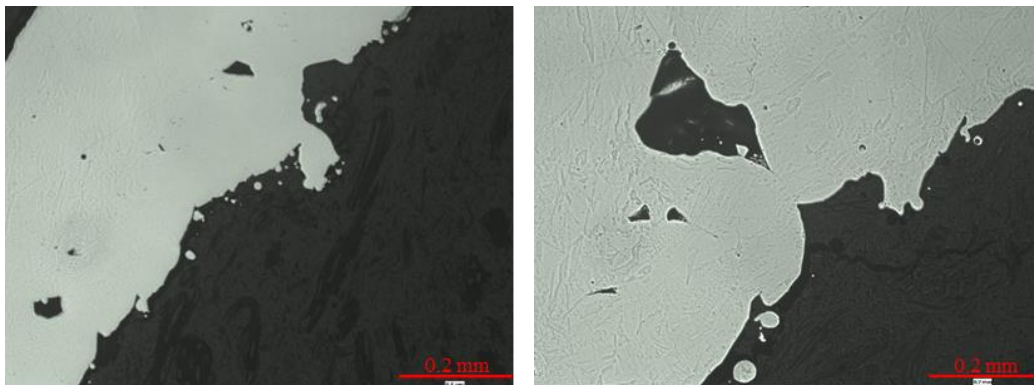


**Figure 4.13** : 8mm unit cell hangover areas.

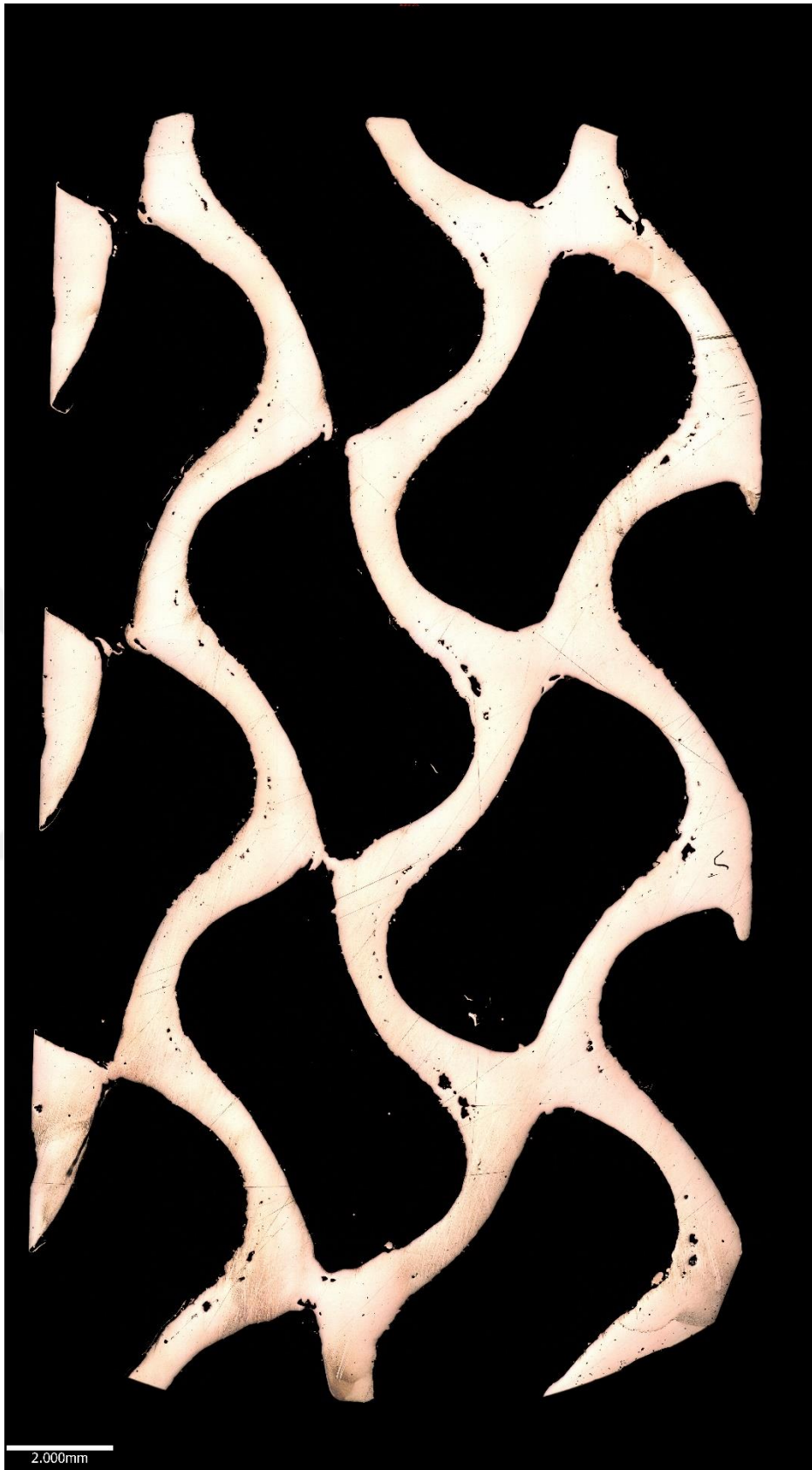


**Figure 4.14** : 8 mm unit cell perpendicular cross-section.

#### 4.1.5 12 mm unit cell size

The most significant deductions concerning the density, unit cell size and AM process relationship of DG structures are availed by the 12 mm unit cell size cross-section images as depicted in Figure 4.15 and Figure 4.17. In Figure 4.15, the cross-section is interpreted as one of the worst hangover plane of the structure due to its horizontality. Significant porosities mostly open to surface can be observed in the down-facing surfaces as well as surface aligned enclosed porosities in the less down-facing but still hangover areas.

In Figure 4.17, the perpendicular cross-section shows the dropped regions in the hangover areas. These heavily porous areas are interpreted as the hangovers of the next adjacent layers. They are also coherent with the surface profile measurements explained in the following section. In the concave areas, porous regions occupy the area under the modelled-to-be-solid region. However, in convex areas, porous regions effuse out of the CAD geometry by adding more powder into the melt pool. This results in the weight increase of the structure than the designed value. It is concluded that these regions are the main cause of mass incoherence between the CAD and manufactured specimens especially in higher unit cell sizes.

As it can be well observed in Figure 4.18, porosity reduction near the surface is proportional with the angle of build orientation. The red arrows indicate the increasing build orientation angle in microscopic images. In horizontal down-facing region shown on the upper left side the pores are open to surface and surface profile is worse than the diagonally down-facing region on the upper right side which has enclosed pores. As the build angle keeps increasing, the enclosed pores become even smaller and sparser. The effect of the build orientation on the down-facing surfaces are clearly apparent in these figures.



**Figure 4.15 :** 12mm unit cell paralel cross-section.

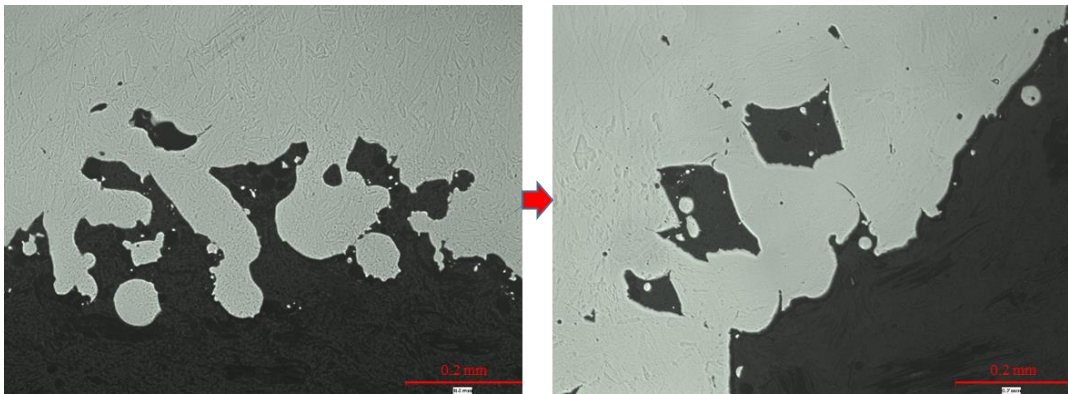


**Figure 4.16 :** 12 mm unit cell near surface defects are changing from open to surface to enclosed as the build orientation changes.

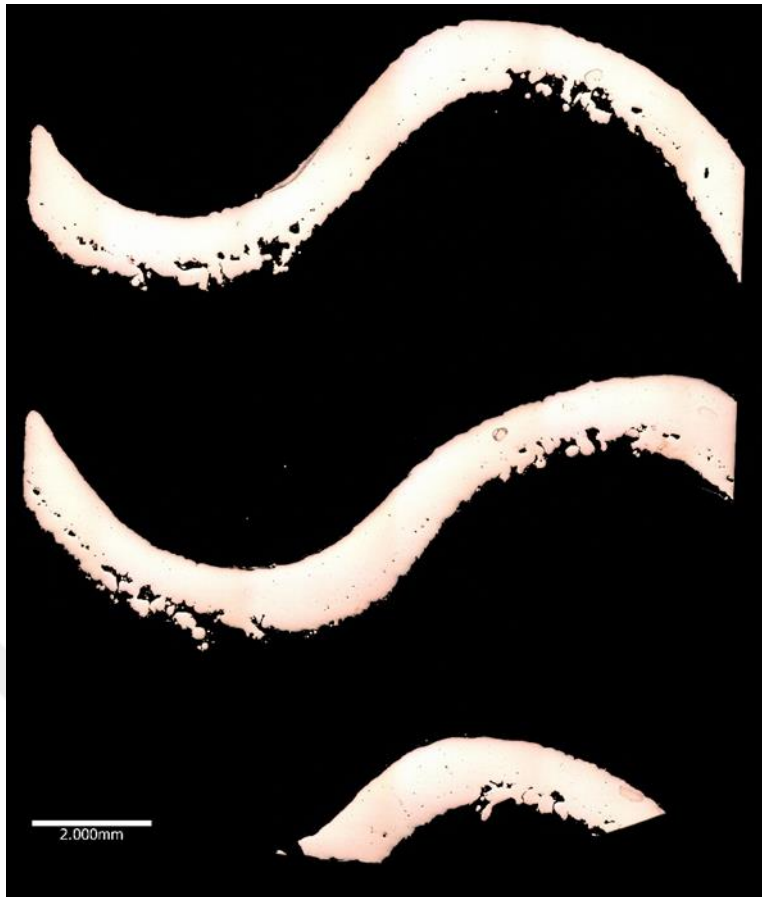


**Figure 4.17** : 12 mm unit cell perpendicular cross-section.

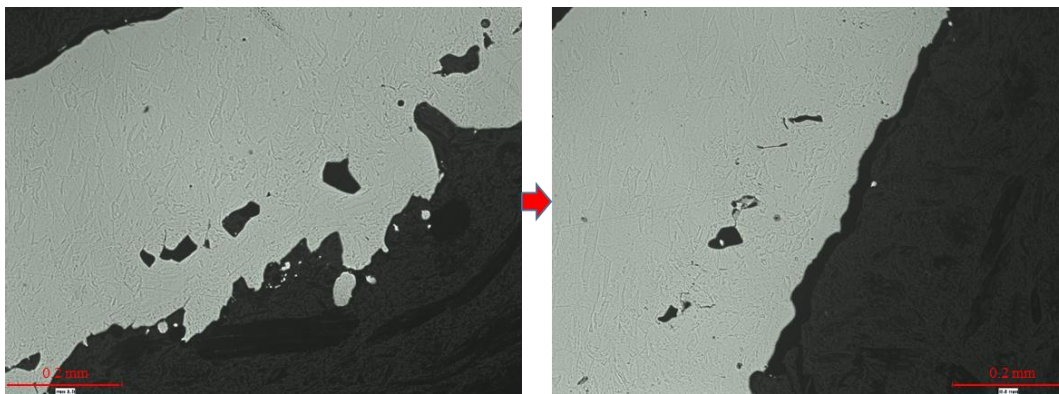


**Figure 4.18** : 12 mm unit cell near surface defects size decrement in overhang areas as the build orientation changes.

## 4.2 Surface Topology and Quality

The topological data gathered from the scanning of up facing, down facing and side facing surfaces are best fitted with the CAD geometry in GOM software. Because of the complexity of DG structure, no datum points or lines could be used as a reference

to make correlation with the CAD geometry. This also points out another difficulty of examining the lattice structures non-destructively.

Since the side, down and top surfaces of DG specimens experience the effects of gravity differently, best fitting approaches must be adopted accordingly. For up facing surfaces, the surface morphology is relatively good and there are more data points in the extracted .stl files which potentially align correctly with the CAD geometries. In these areas, edges are excluded from the best fit operation and rest of the surfaces is chosen only. This approach also eliminates the possible misalignments of the acute height increment defects on the edges.

In side facing surfaces, overhang surfaces in the down facing areas becomes visible. Therefore, only the relatively vertical surfaces and up facing areas of the edges are used to best fit the structures. The most problematic side is the down facing side for all specimens. Edges cannot be used because of the residues of broken supports and the majority of the visible surfaces are heavily misaligned from the CAD geometry because of down facing surface characteristics. Therefore, small areas in every unit cell with the highest verticality is selected for best fitting. Following the best fitting, well aligned edges, support residues and down facing surface overhangs represented an acceptable sanity check for this approach.

In Alicona InfiniteFocus<sup>®</sup> software, inspection utility is employed for color mapping. Following the best fitting, this utility simply measures the closest distance between the .stl data file and CAD geometry and assigns color codes for varying values. This utility significantly helps to make structural examination and allows to see the distortion tendency for each specimen. For the ease of comparison, all the color codes are set to the same interval of 0.15-0.15  $\mu\text{m}$ . It must be remarked that the best fitting a point cloud to a CAD geometry results in an approximate geometrical accuracy. Therefore, measurement output data of this analysis should not be regarded as a high precision reading since in best fitting no datum is used as a reference. Using reference areas in all unit cells through the scanned face increases the accuracy of the measurement by dissipating the best fitting error into the whole surface morph.

#### 4.2.1 3 mm unit cell specimen

Because of the excessively high visible roughness on the side and down facing surfaces of 3 and 4 mm unit cell size specimens, only up facing surfaces are scanned. In the 3 mm specimen as seen in Figure 4.19, In this specimen, a denser structure and a higher structural homogeneity are interpreted as the cause of lesser distortion. In local regions especially near the edges, dark blue areas represent surface profile dropdowns. This can be correlated with the droop formations on the overhang surfaces as observed in the cross-section of Figure 4.1 and can be considered as evidence that the down facing surface quality affects the upper surface profile for thin features.

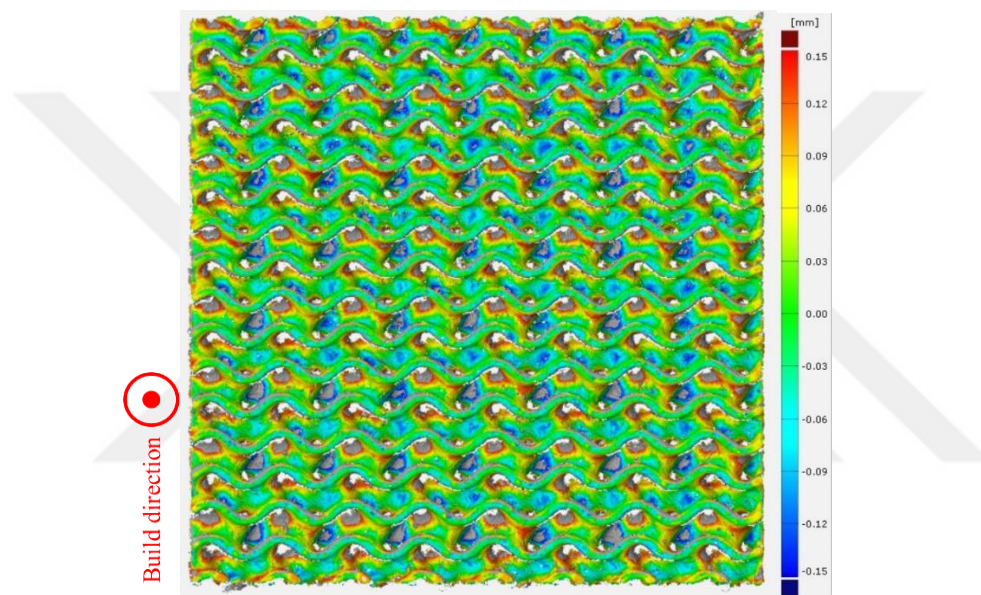
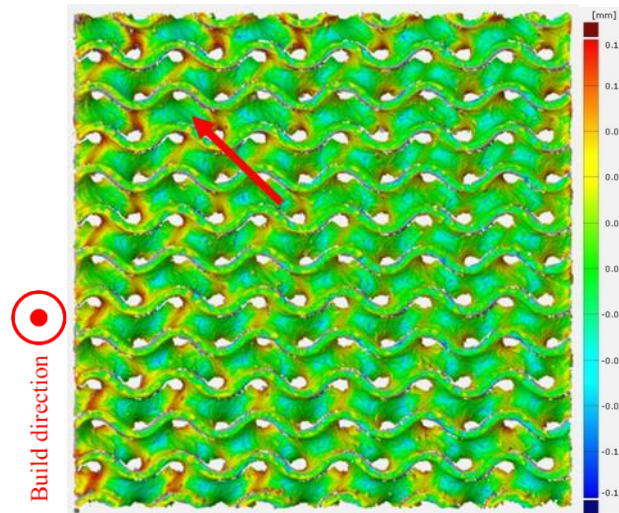


Figure 4.19 : 3 mm unit cell top surface profile.

#### 4.2.2 4 mm unit cell specimen

In Figure 4.20, 4 mm unit cell size specimen shows a better surface profile than 3 mm unit cell size specimen. This profile advancement is evaluated as the result of the better quality down facing surface characteristics of 4 mm unit cell size specimen. There is a visible height increment increasing towards the upper left corner of the side caused by distortion.



**Figure 4.20** : 4 mm unit cell top surface profile.

### 4.2.3 6 mm unit cell specimen

In Figure 4.21, the results of the up facing side of 6 mm specimen is shown. Dark blue areas are the mostly negative angled surfaces of DG. These areas show profile drop downs because of lack of self-supporting of the structure. Most of the outward edges are warm colored. This represents an evidence of acute height increment caused by the laser melting process. Increasingly becoming denser red color towards the upper right corner is the evidence of distortion in this direction.

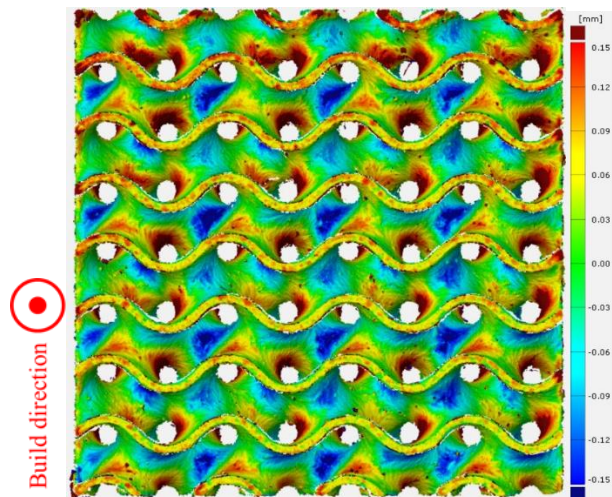


**Figure 4.21** : 6 mm unit cell specimen top surface profile.

In Figure 4.22, down facing morphology is shown of 6 mm unit cell size sample. In the edges, residues of the supports are visible. The areas which are completely horizontal exhibits a very defected hangover profile. In Figure 4.23, higher resolution

micro scanning image can be seen. Color mapping is performed by the software embedded in the computer of Alicona and a relative reference is used to measure the local height differences which can be seen in the same image. The down facing surface roughness visibly aligns with the cross-section images. Besides the heavily overhang and bumpy areas, less horizontal regions show a significant profile misalignment as it can be seen in dark red areas in Figure 4.22. It can be assumed that the material density in these regions are not as desired. Since this is the reverse side of the up facing surface, the distortion pattern observed in up facing surface is also observed however with the reverse color codes. The distorted upper left corner can be seen in a denser blue color.

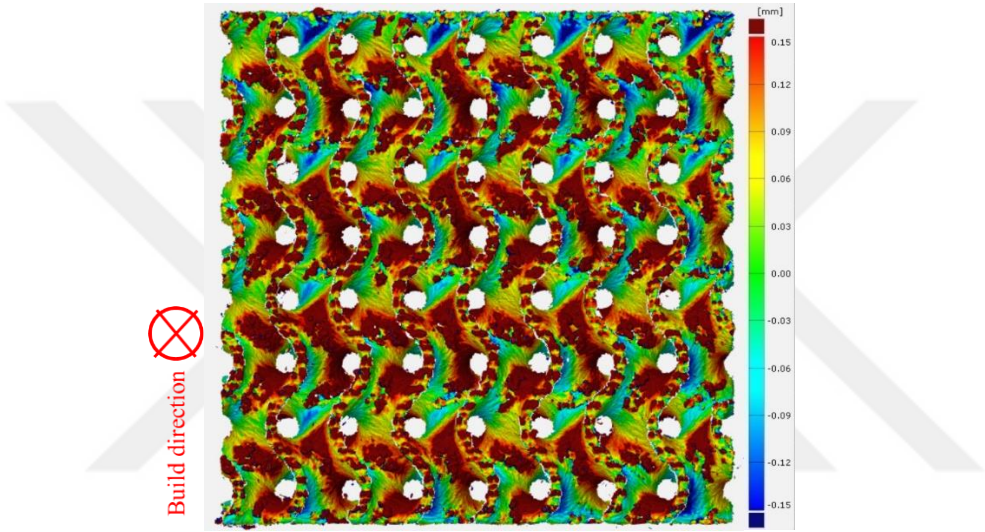


**Figure 4.22 :** 6 mm unit cell specimen down facing surface profile.

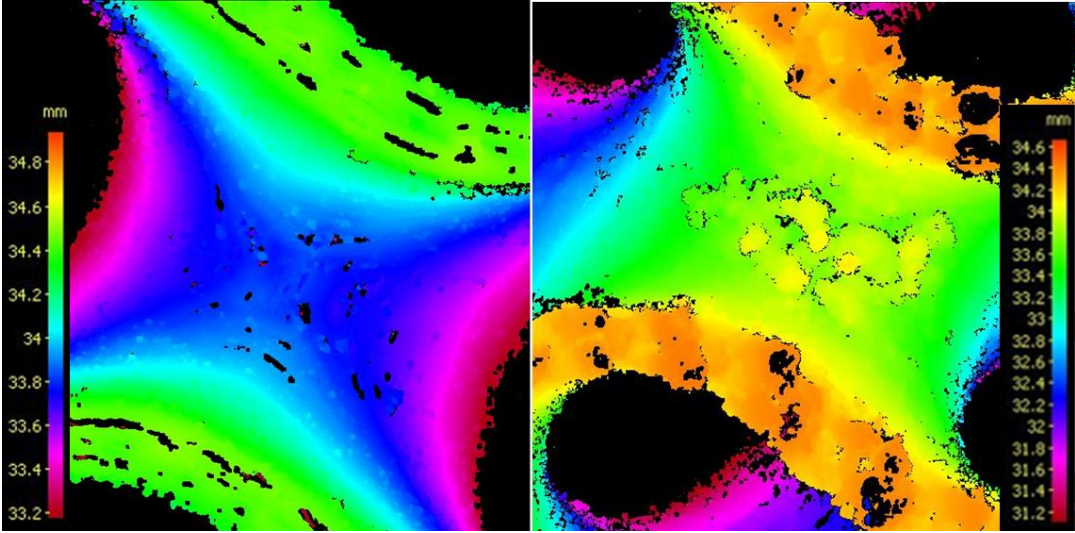


**Figure 4.23 :** 6 mm up facing (left) and down facing (right) areas micro scanning.

Side facing surface profile analysis of 6 mm unit cell size specimen can be seen in Figure 4.24. Bumps in the down facing regions and near the edges are visible. There is also a slight distortion visible with increasing denser blue regions on two sides of the image. This distortion may also have affected the up and down faces' profiles. However, such distortion is not observed in those analysis.

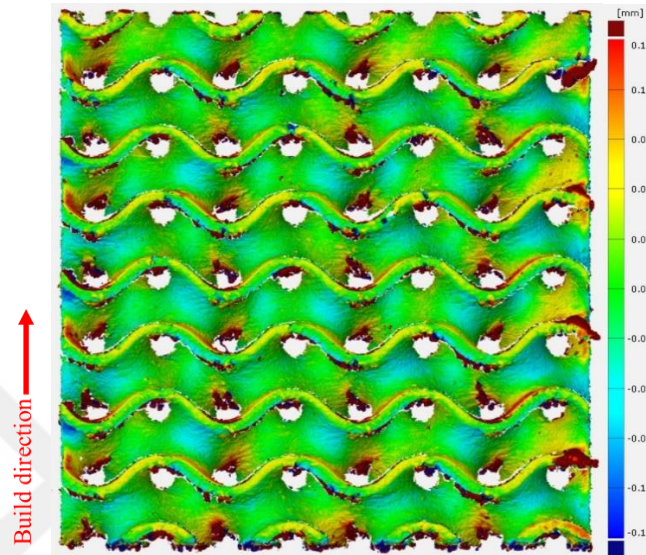


**Figure 4.24 :** 6 mm unit cell specimen side facing surface profile.

#### 4.2.4 8 mm unit cell specimen

In Figure 4.25, top surface profile of 8 mm unit cell size specimen can be observed. It can be seen that as the unit cell size gets larger, there are more blue spots in the most horizontal regions of the up facing surfaces. This means that the down facing areas of the same regions start causing the up facing region profile drop downs. This is an expected result of using bigger unit cell sizes with higher arc diameters. Furthermore, on the two sides of the specimen, distortion is observed via the increasingly yellow colors.

In Figure 4.26, down facing bumps can be observed. At the most down facing area of each unit cell, there is a less dropped down region among the dark red mapped bumps. It is also visible that in the down facing surface, the distortion in the sides is more clear.

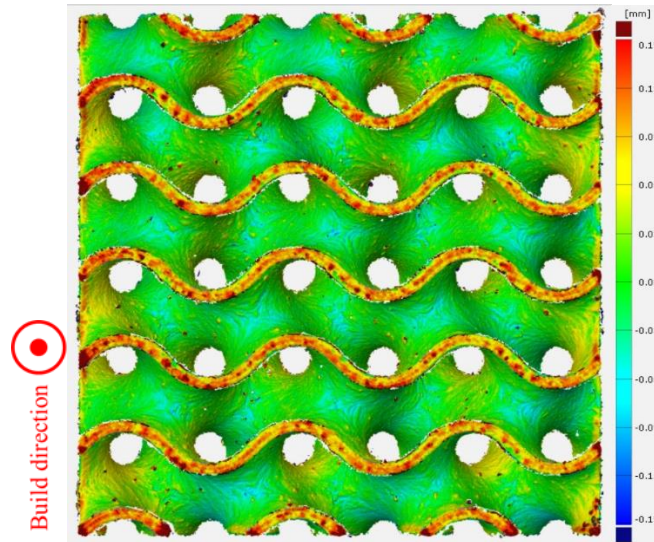


**Figure 4.25 :** 8 mm unit cell specimen top surface profile.

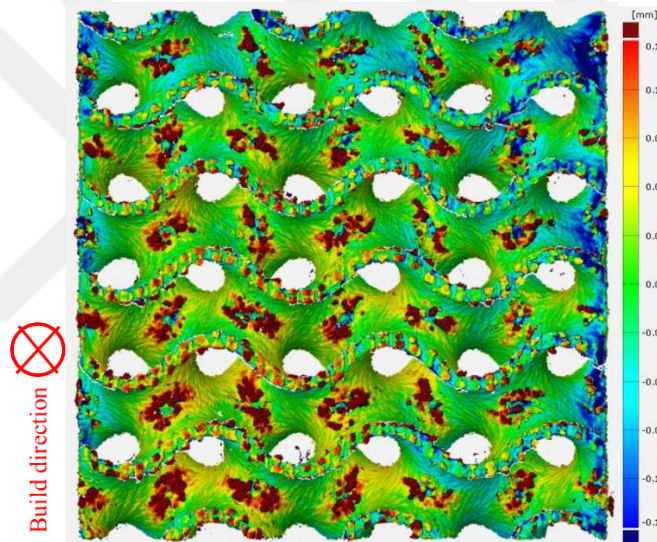


**Figure 4.26 :** 8 mm unit cell specimen down facing surface profile.

Down facing and up facing surface characteristics are also observable in detail in Figure 4.27.

Side facing surface in Figure 4.28 shows a similar pattern as of 6 mm unit cell size specimen's side surface. It can be said that the magnitude of the surface profile mismatch increases with the increasing unit cell size.

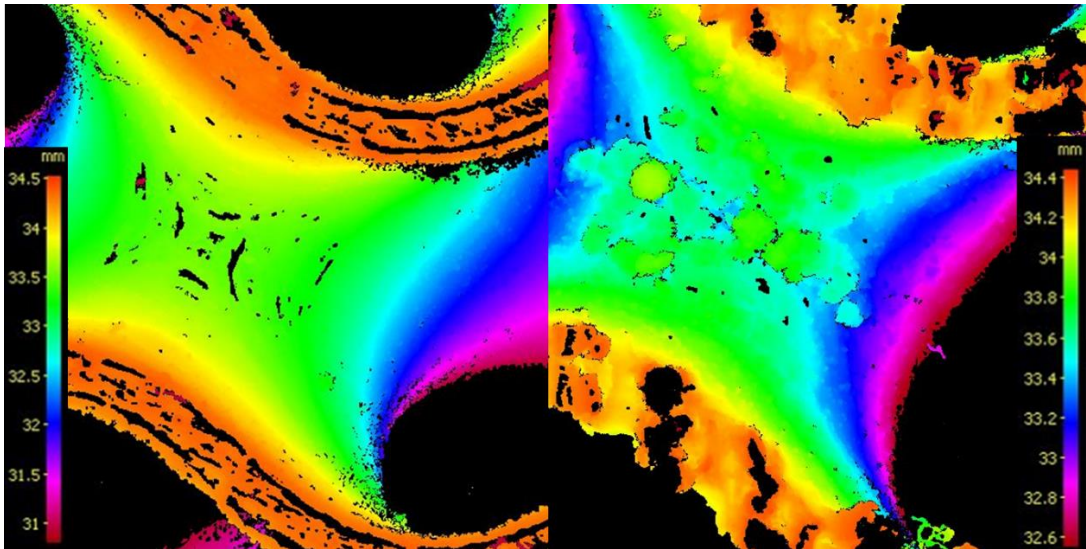


**Figure 4.27 :** 8 mm up facing (left) and down facing (right) areas micro scanning.

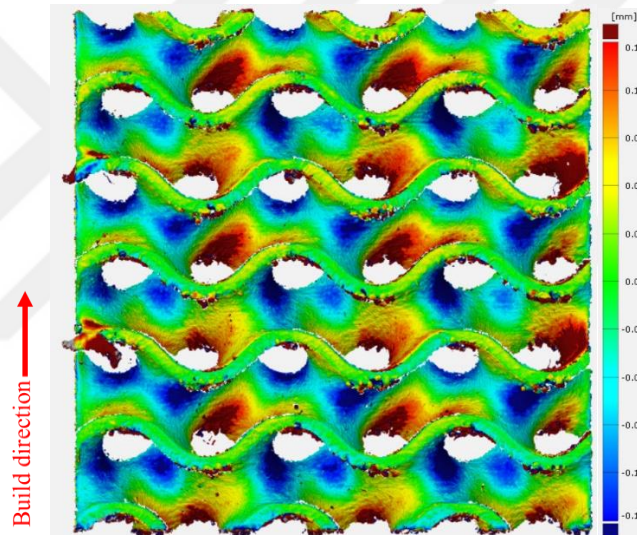


**Figure 4.28 :** 8 mm unit cell specimen side facing surface profile.

#### 4.2.5 12 mm unit cell

In Figure 4.29, 12 mm unit cell specimen up facing areas shows even a larger surface drop down and can be seen as the blue areas on the image. Due to the AM process, unsupported regions drop down and this increases with larger arc diameters in such geometries. It is well observed that one handicap of using larger unit cell sizes is having a more distorted surface profile.

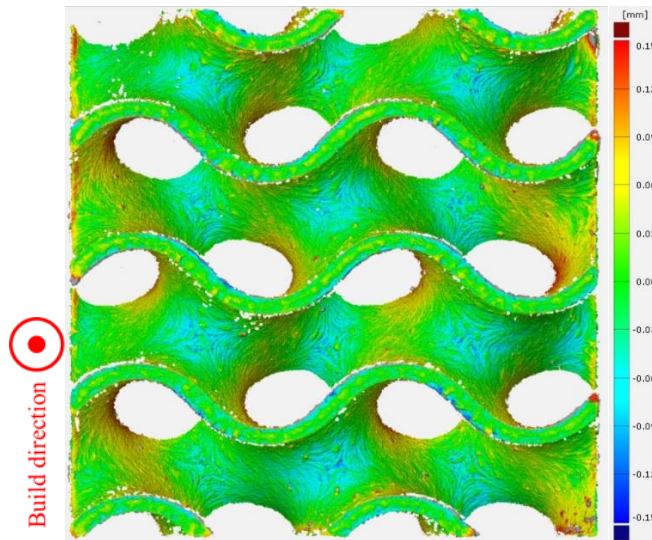


**Figure 4.29** : 12 mm unit cell specimen up facing surface profile.

Same comment can be made for the down facing area in Figure 4.30. Bumps are observed in even larger quantities and the effect is more severe in the down facing surfaces.

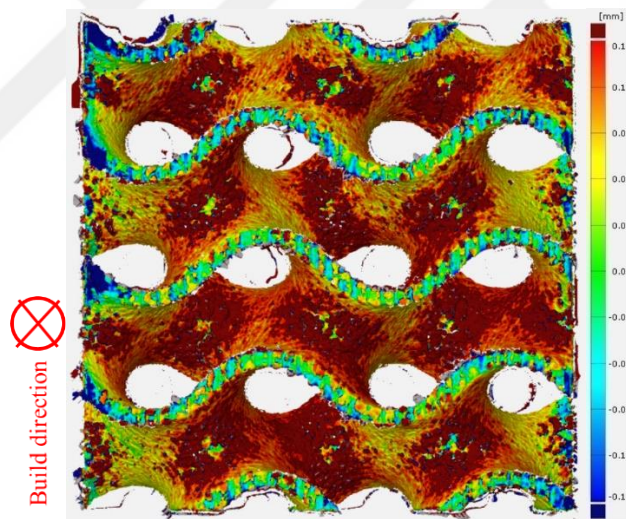


**Figure 4.30** : 12 mm unit cell specimen down facing surface profile.

Down facing and up facing surface characteristics are also observable in detail in Figure 4.31

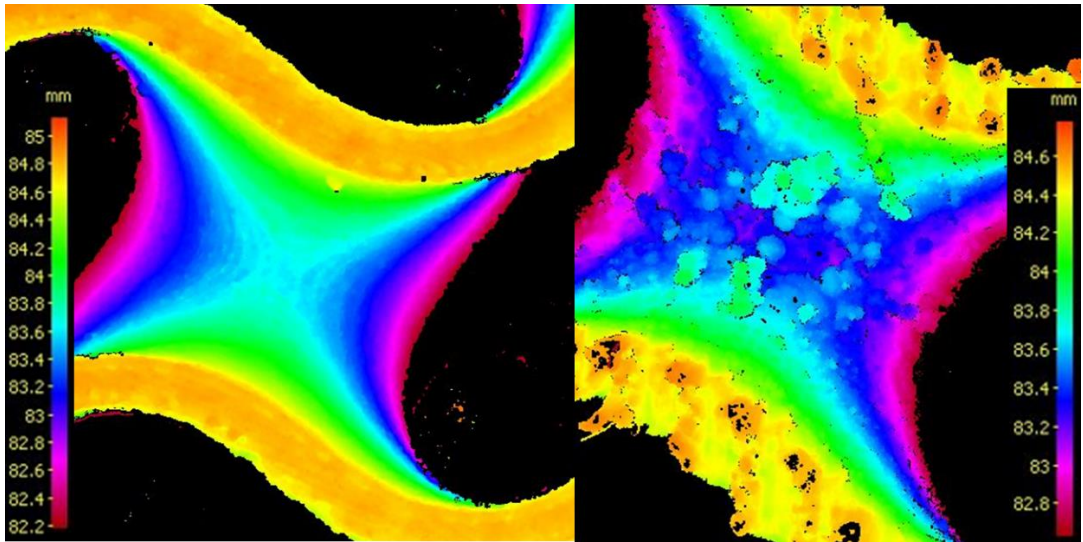


**Figure 4.31** : 12 mm up facing (left) and down facing (right) areas micro scanning.

In Figure 4.32, surface and edge mismatch profile matches the mismatch profile of 6 and 8 mm unit cell size specimens.

Geometrical measurements given in this section can be leveraged for designing DG lattice structures with surface offsets to compensate the manufacturing defects. Moreover, the quality difference of the surfaces in different regions represents lesser material property areas. This handicap can be included to stress modelling of DG structures in design assessments.

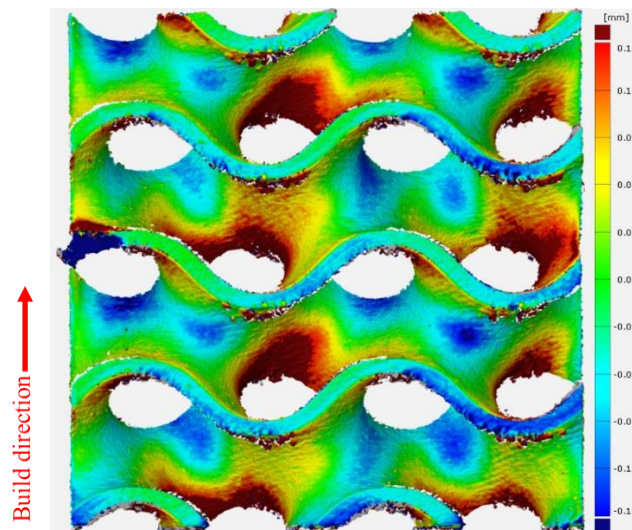


**Figure 4.32** : 12 mm unit cell specimen side facing surface profile.

SEM micrographs of top surface 12 mm unit cell specimen is shared in Figure 4.33 and Figure 4.34. In Figure 4.33, edge of the top surface is focused. Right bottom side of the edge has an overhang down facing surface underneath and it caused the indicated near the surface defects. Position of these defects aligns with the metallographically seen near the surface defects. Resolution of the surface is also visible in this micrograph. Powder residues also as called as satellite powder particles are observed. These satellite powders are denser in the layer interfaces or laser hatch overlaps. Main caused of this is regarded as the heat escape from the melt pool concentrates in the overlap regions of laser passes.

In Figure 4.34, upper surface region of 12 mm unit cell specimen can be seen with a higher magnification level. The paths seen in this micrograph are each laser travel trajectories in the surface and since these trajectories have a curved travel path, it is concluded that each of the path is of a different layer. There are pockets filled with unmelted powder observed in the surface as they are indicated in the image. These pockets are caused by the lack of fusion in between the layers. Since this part of the 12 mm unit cell specimen is also found to have surface profile drops in Figure 4.29, lack of fusions are concluded to be caused by the effect of overhang area under the observed surface. It is also clearly visible in this image that the satellite powders are concentrated in the overlap regions. There are also ripple like patterns are observes in the laser paths. These ripples are caused by the molten metal and the distinctive shape is given by the moving laser beam.

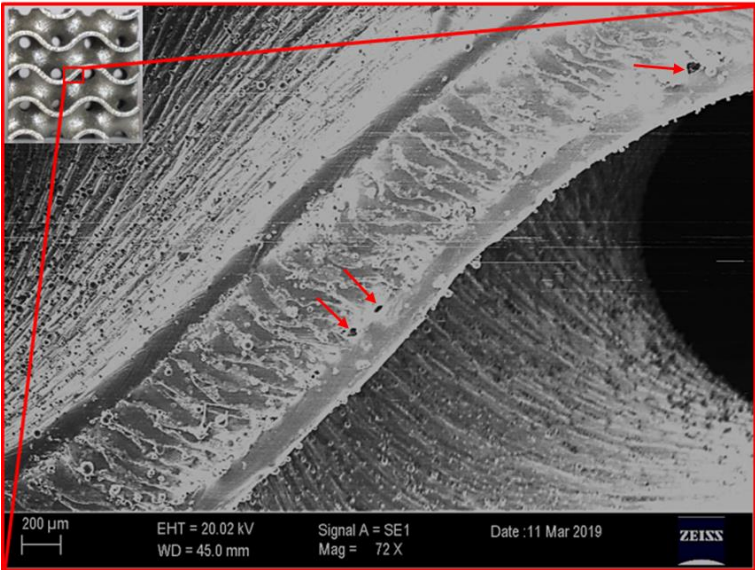


**Figure 4.33 :** SEM micrograph of 12 mm unit cell size specimen.

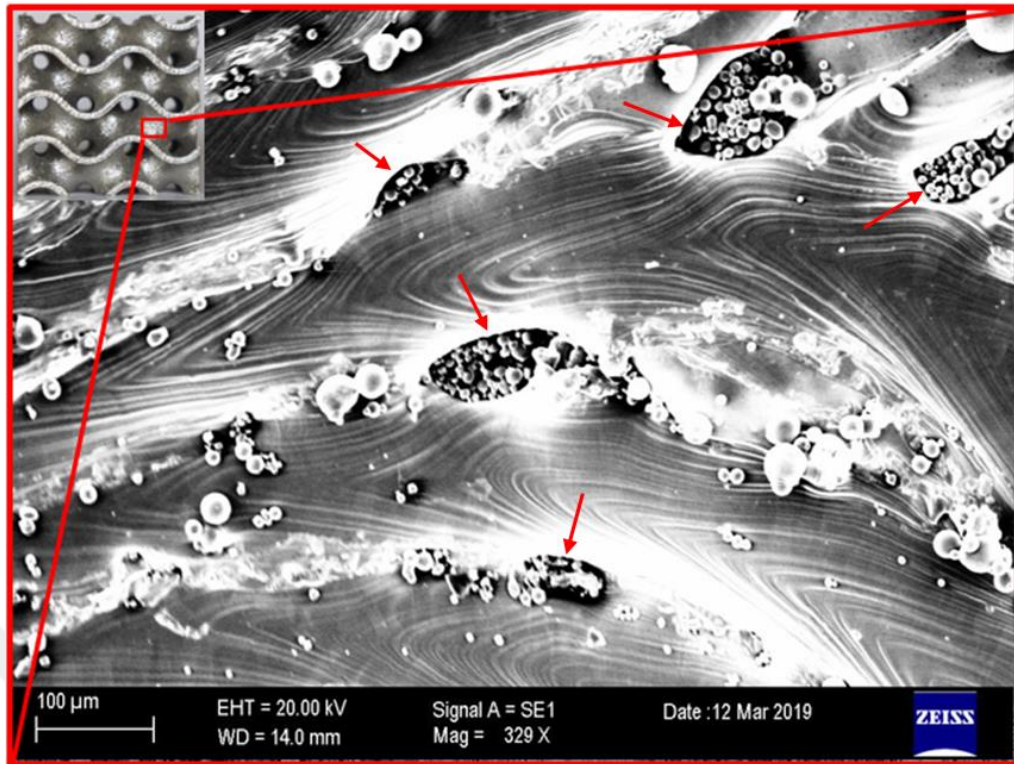


**Figure 4.34 :** Higher magnification SEM micrograph showing unmelted powder residues inside surface voids.

### 4.3 Compression Testing

According to Gibson and Ashby, cellular solids with relative densities lower than 0.3 exhibit bending or stretching dominated compressive collapse behavior. These structures have been regarded as an interconnected network of beams. The theoretical background for beam network fails to explain higher density cellular solids and they are regarded as porous solids (Gibson, L. J., Ashby, 1997). The relative density of the samples of this study, being less than 0.3, fits in the first description.

There are three main phases of compressive deformation in low density cellular solids. As shown in Figure 4.35, the first phase is the linear elastic region where under compressive loading the units of the cellular structure start to be bent elastically until it yields. The second phase represents the plateau region. The character of the curve in this region largely depends on the ductile-brittle characteristics of the material that the lattice structure consists of. If the material has a brittle character, the weakest points undergo fast fracture layer by layer. Therefore, the resulting curve shows a fluctuating behavior. With a ductile material, a long collapse plateau is expected since the whole

structure stretches simultaneously. The third phase is densification. In this phase, the cellular elements in the structure start to make physical contact with each other and stress output starts increasing asymptotically. Beginning of this phase is regarded as the energy absorption limit of the structure. Especially in applications in need of impact resistance such as personal protective equipment, packaging and armors, densification in higher strain level is desired. After this point, structure's ability to transform the energy of compressive loading into plastic deformation decreases and the energy is started to be transferred to the other side of the structure. These three phases in plastic and brittle cellular structures can be seen in Figure 4.35.

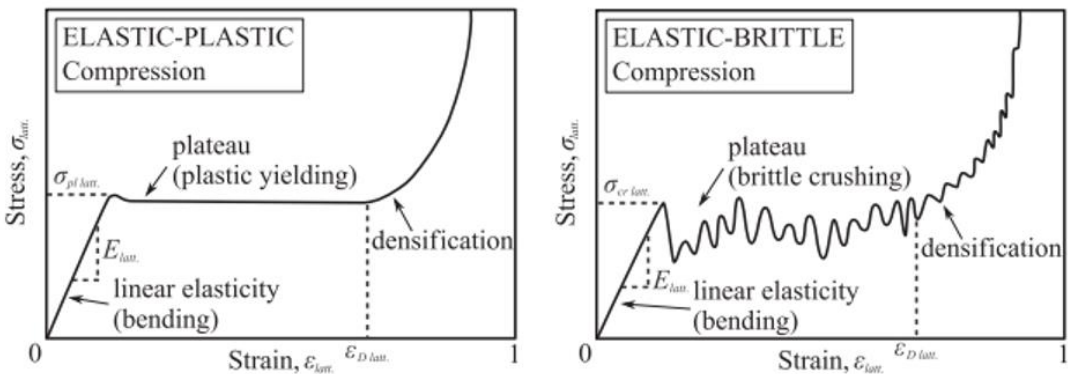


**Figure 4.35** : Plastic and brittle compressive deformation behavior of cellular solids (I Maskery et al., 2016).

The resulting compressive stress-strain curves of all specimens are demonstrated in Figure 4.37. As it was mentioned in the previous section, the sharpest points as indicated in Figure 4.36 in the structure tend to be distorted because of the heterogeneous thermal distribution during the process. When these acute points contact the platen of the test device, it causes the machine to read false stress values. In order to compensate this problem, all curves are plotted with strain values corrected by required offsets and overlapping of the same unit cell size specimen compression curves is enabled. Three replicates for each unit cell size specimen showed an excellent similarity as a proof of process repeatability.

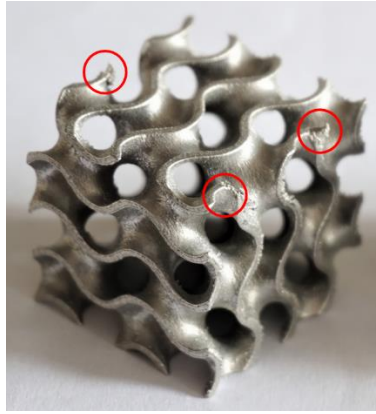


**Figure 4.36 :** Sharp points in the specimens.

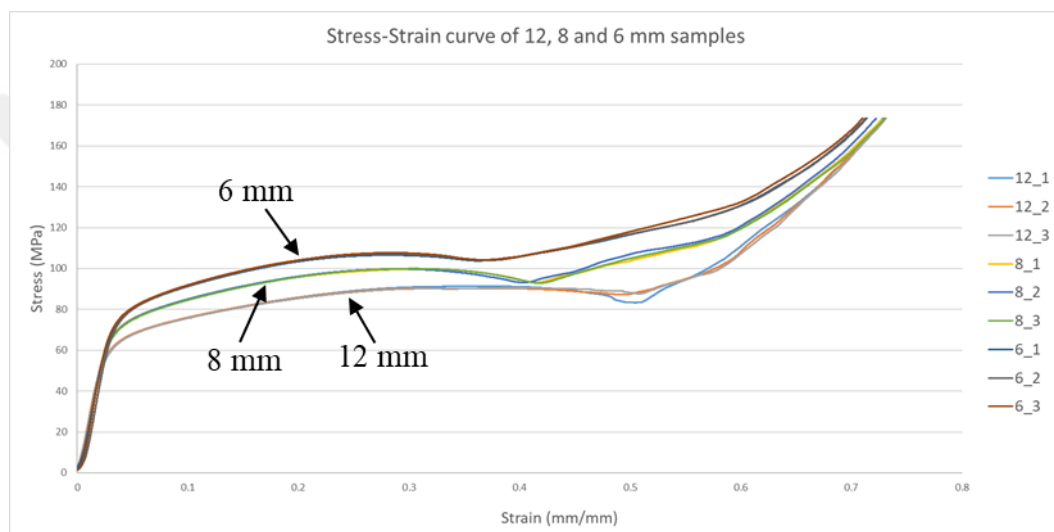


**Figure 4.37 :** Compressive stress-strain curves of 12, 8 and 6 mm unit cell specimens with three replicates for each case.

Aforementioned three compression phases of cellular solids can be well observed in Figure 4.37. The initial stage ends with yielding and the 0.2% yield value alongside with the modulus of elasticity is calculated for each different unit cell size specimen in Excel. It can be seen that yield stress points increase as the unit cell size gets smaller (see Table 4.2). In the second phase, there is no rapid fluctuation observed in the curves. This behavior aligns with the expected result since HS188 is well-known for its ductility with elongation values reported as high as 55% at tensile fracture point.

During the second phase, all curves show lowered rate of increasing stress level up the highest point. This point can be seen as the ultimate point that the material yields. As it can be seen in the exemplary image of 8 mm unit cell specimen in Figure 4.38, in all specimens there are cracks near the edges. These cracks have been initiated in the free

end edges of the structure and propagated towards the internal sections. The existence of the cracks is the evidence of stress relief in the structure. At the highest stress points, which in this case the free edges, the stress exceeds the ultimate yield stress point of HS188. The strain value of which the stress relief starts shifts higher with bigger unitcell sizes. As it can also be seen in the plot given in Figure 4.37 that the highest stress points in the plateau region for each curve is as the following: 6 mm, 8 mm and 12 mm unit cell sizes for 0.27, 0.31 and 0.38 strain rates, respectively. This result can be explained by bigger radii of gyroid surfaces in bigger unit cell sizes, the relative density error caused during the manufacturing of the specimens, better surface quality and material integrity of bigger unit cell size specimens as shown in previous section.

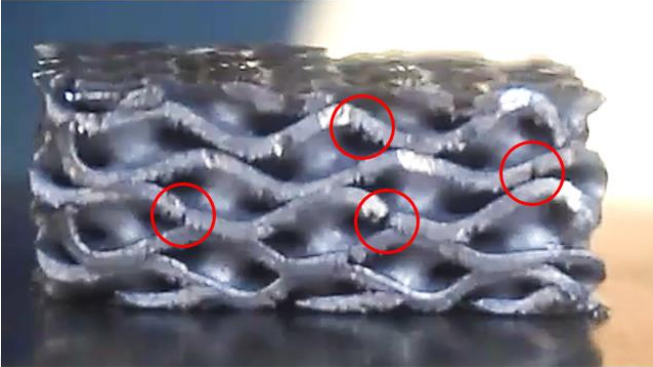


**Figure 4.38 :** 8mm unit cell specimen after compression test with cracks marked.

After the stress relief point, a short amount of strain increment is required before the structure gets into the densification phase. Another result of the ductility of HS188 is that densification starts shortly after the stress level reaches its ultimate point. During the densification, sheets compromising the DG structure make contact and bending of the elements becomes less effective. From there on, the material is plastically compressed. Slightly sharper changing angles in densification phase is interpreted to be caused by friction in between the surfaces. Areas under the curves (W) until the onset of densification as seen in Figure 4.39 are calculated in Excel.

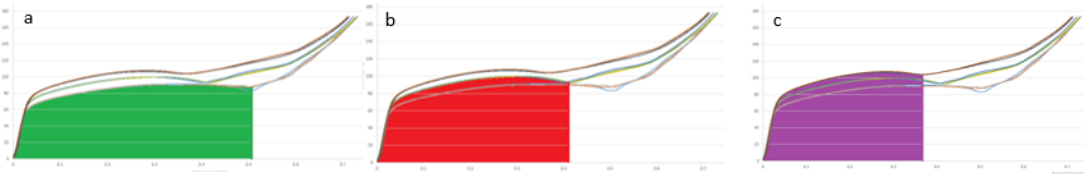


**Figure 4.39 :** Areas under the curve until densification strain: a) 12 mm unit cell, b) 8 mm unit cell, c) 6 mm unit cell.

The area values have been normalized per Equation 4.1.

$$\frac{W}{V_{latt.}} = W_v \quad (4.1)$$

$W_v$  values have been plotted against strain values. Resulting plot can be seen in Figure 4.40. A slight decrease in the slopes can be observed separately for each unit cell size and these slope changes occur at the strain ratios which the crack initiation and densification starts.

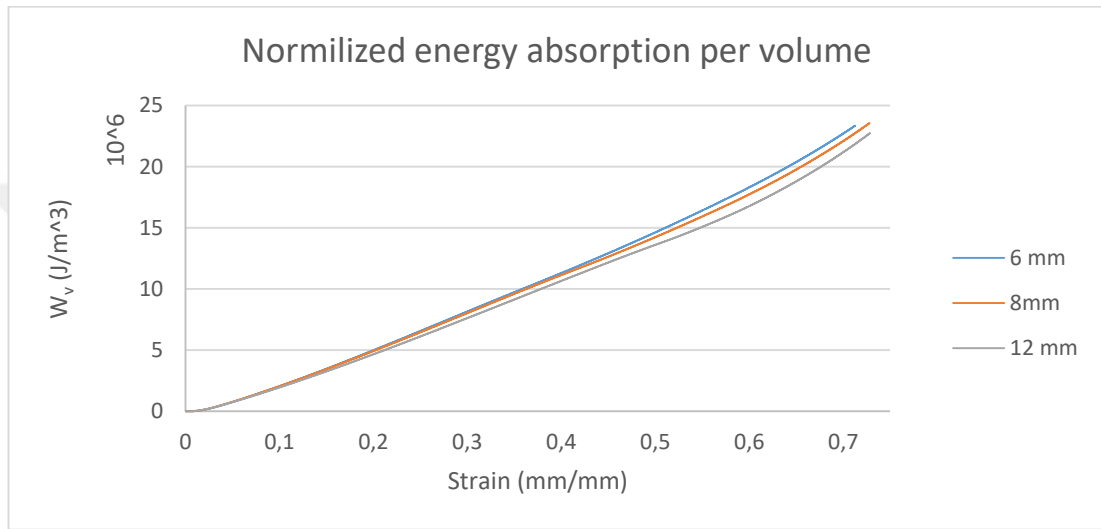


**Figure 4.40** : Normalized energy absorption per volume.

The cumulative energy absorption values accompanied by the densification strain values are given in Table . Together with Figure 4.40, calculated values are normalized by the solid volume of each structure. This means that the effect of density difference is eliminated. It is concluded that in additively manufactured DG structures comprised of HS188 higher unit cell size acts as a better impact absorbent structure.

**Table 4.1** : Strain and energy absorption values for 6, 8 and 12 mm specimens.

Unit cell size (mm)	% strain @ densification	Absorbed energy MJ/m <sup>3</sup>
6	35	111.84
8	41	115.90
12	50	123.85

In the plot of Figure 4.41, the absorbed energy is plotted against stress readings for each specimen, both are normalized by the Young’s modulus of the material. This approach has been proposed for making comparison in between different cellular structures with different design parameters such as unit cell size, material and design by Ashby *et al.* (Gibson, L. J., Ashby, 1997) and the same approach has been used to evaluate DG structures in the studies of Maskary *et al.* (I. Maskery, Aboulkhair, et al., 2017; I. Maskery, Sturm, et al., 2017; I Maskery et al., 2016; Ian Maskery et al., 2016). The resulting plot can be used to select the most convenient lattice structure for the system requirements of the various applications. The structure with the highest energy absorption value without reaching a specific stress threshold can be chosen accordingly.

Following the same approach, the result of this study shows that the 12 mm specimen shows the highest amount of energy absorption per volume with the lowest stress compared to the other two specimens. Onset of yielding and the plastic deformation plateau is visible in the plot. Another significant interpretation is that the higher unit cell size DG specimens exhibit a higher stress drop following to crack initiation phase.

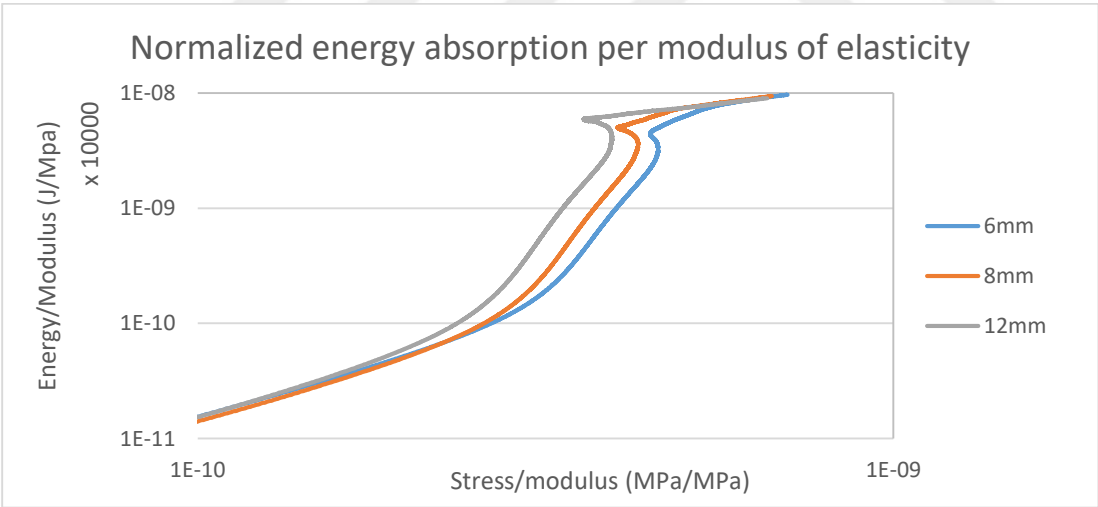


**Figure 4.41 :** Normalized energy absorption per modulus of elasticity.

A bigger unit cell sized specimen absorbs a higher energy before densification. In the study of Ashby *et al.*, there is a proportion between the relative density of the cellular structure and the energy absorption as it is seen in Figure 4.42. They claim that the relative density of any cellular structure can and should be optimized accordingly to the energy absorption required (Gibson, L. J., Ashby, 1997). In this study, resulting

energy absorption value is influenced by both the difference in actual relative density of the manufactured specimens and unit cell size of DG structure.

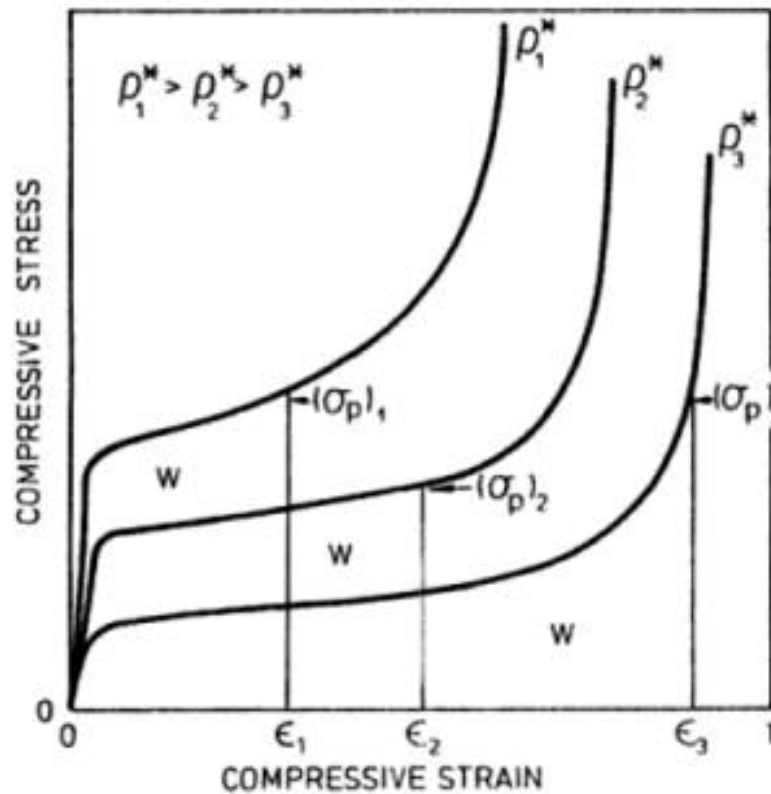


**Figure 4.42 :** The relative density dependency of energy absorption in the ductile cellular structures (Gibson, L. J., Ashby, 1997).

Ashby’s work also shows the compression behavior of conventionally manufactured stochastic ductile foam metals in comparison to the fully dense elastic solids (see Figure 4.43). Regarding the similarity of HS188 DG compression test results obtained in this study, it can be claimed that combination of DG unit cell design with HS188 material promises a high potential for energy absorption required applications.

The compression tests were recorded with a digital video camera and the timing of the recorded video was correlated to the strain values recorded by the test machine. In Figure 4.44, Figure 4.45 and Figure 4.46 the pictures taken from the recorded videos can be seen. Pictures marked with “a” and “b” in all the figures are from initial and plastic yielding plateau phases. The strain rate in the pictures “c” are the same for each specimen with different unit cell sizes and they are of the same compression curve’s strain rate at densification.

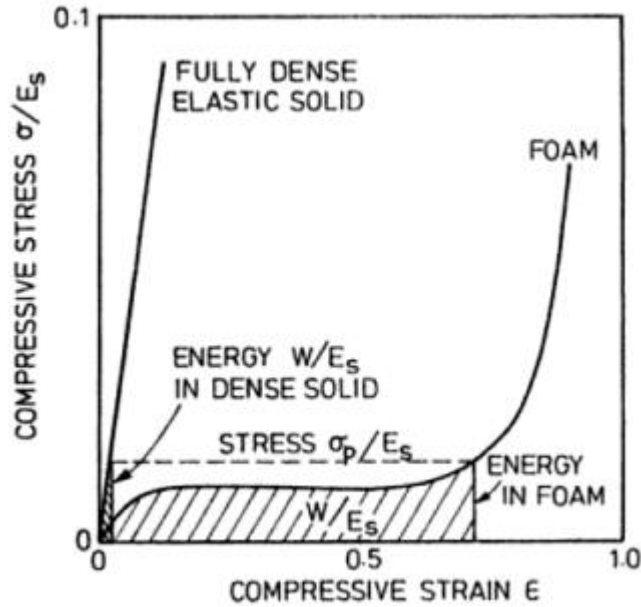


**Figure 4.43 :** Compressive stress-strain behavior comparison of elastic solids and foams(Gibson, L. J., Ashby, 1997).

In all of the specimens, ductile behavior is apparent. Until the strain reaches the stress relief point, no crack initiations are observed. Cracks initiate as the stress-strain curve reaches the highest stress point in the plateau region and propagates until the densification strain. Following the completion of the test, cracks in the crashed samples are examined by SEM. As it can be seen in Figure 4.47, the fracture shows ductile characteristics because of the slow propagation rate, width of the fracture and fracture surface morphology. Since the cracks in all specimens show similar characteristics, only one SEM image is shown from the 12 mm unit cell size specimen.

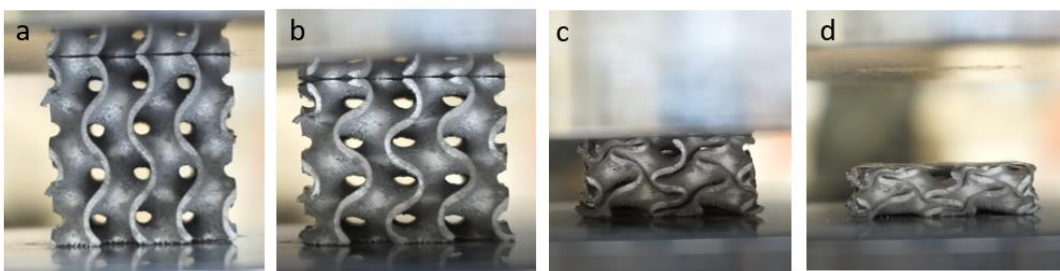


**Figure 4.44 :** 12 mm unit cell size compression test footage with strain values: a) 0, b) 0.2, c) 0.5, d) 0.7 before spring back.

A considerable observation from the test footage is the barreling of the specimens. In 8 and 6 mm specimens barreling can be seen in “c” pictures in Figure 4.45 and Figure 4.46. It starts in earlier strains of plastic yielding phase and it is higher in smaller unit

cell size specimens. However, in 12 mm unit cell size specimen almost no barreling is apparent at any strain level. There are two possible explanations for this phenomenon: First one is the specimen size is insufficient to observe barreling in higher unit cell size structures. In example, if the specimen cube's size would be 48 mm in all dimensions instead of 24 mm, barreling might have been observed. Second explanation is that crushing behavior changes as the unit cell size becomes larger.

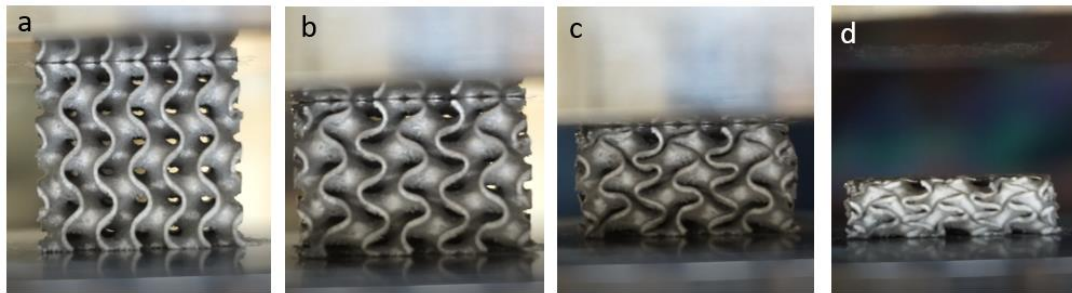


**Figure 4.45** : 8 mm unit cell size compression test footage with strain values: a) 0, b)0.2, c) 0.41, d) 0.7 before spring back.

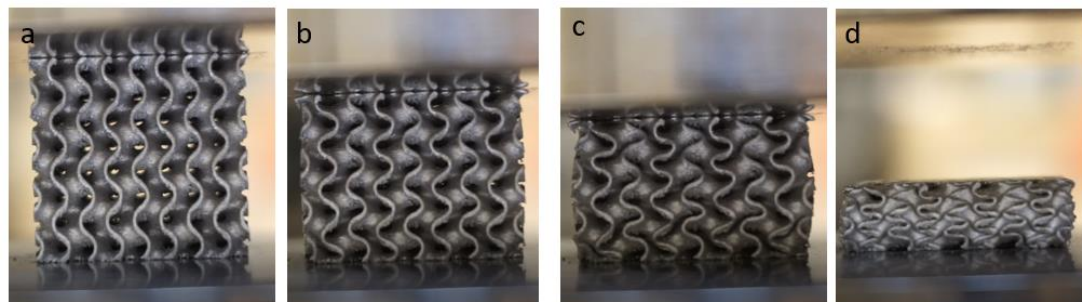


**Figure 4.46** : 6 mm unit cell size compression test footage with strain values: a) 0 b)0.2, c) 0.35, d) 0.7 before spring back.

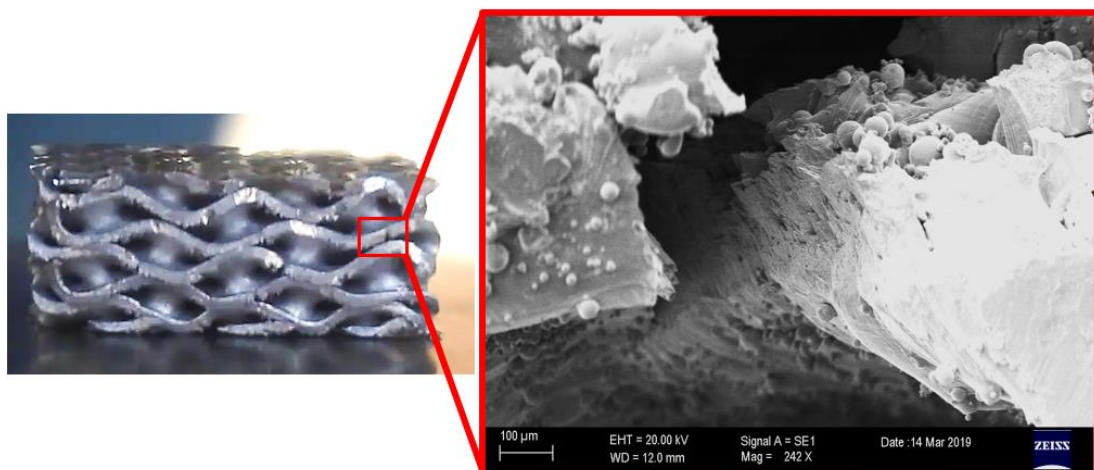


**Figure 4.47** : SEM image of a crack near the edges after compression test.



**Figure 4.48 :** Crushed DG specimens. From left to right: 12 mm, 8 mm and 6 mm.

Calculation approach of modulus of elasticity can be seen in Figure 4.49, Figure 4.50 and Figure 4.51. Calculated results can be seen in Table 4.24.2.

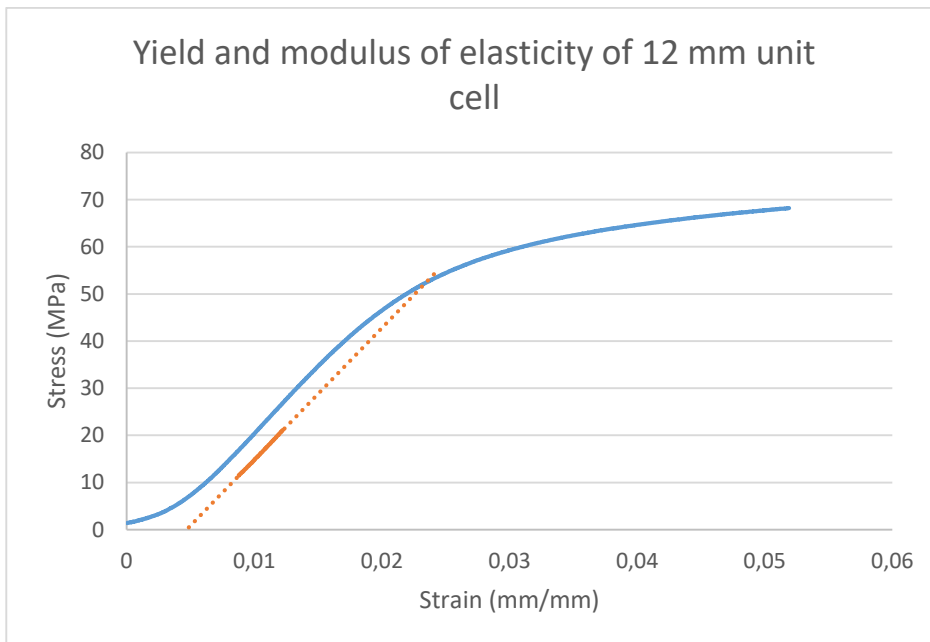


**Figure 4.49 :** Yield and modulus of elasticity of 12 mm unit cell specimen.

According to Ashby *et al.* (Gibson, L. J., Ashby, 1997), there are three main parameters effecting the mechanical behavior of cellular structures: relative density, material that the structure is comprised of and the geometry of the structure. The latter parameter can also be regarded as the effect of distribution of material over the design space. Considering the specimens of this study, design space can be expressed as the  $24 \text{ mm}^3$  volume and the different unit cell geometries can be regarded as the material positioning strategies inside that volume.

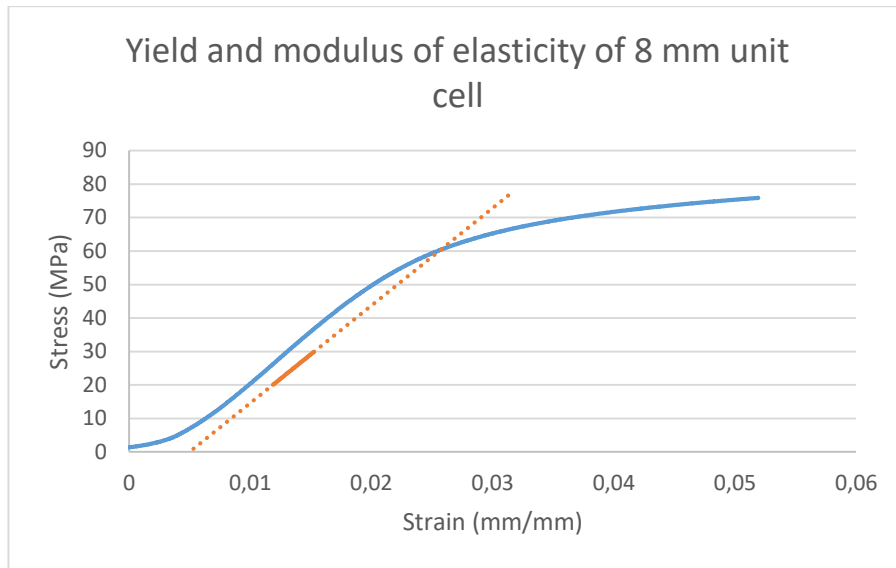


**Figure 4.50** : Yield and modulus of elasticity of 8 mm unit cell specimen.

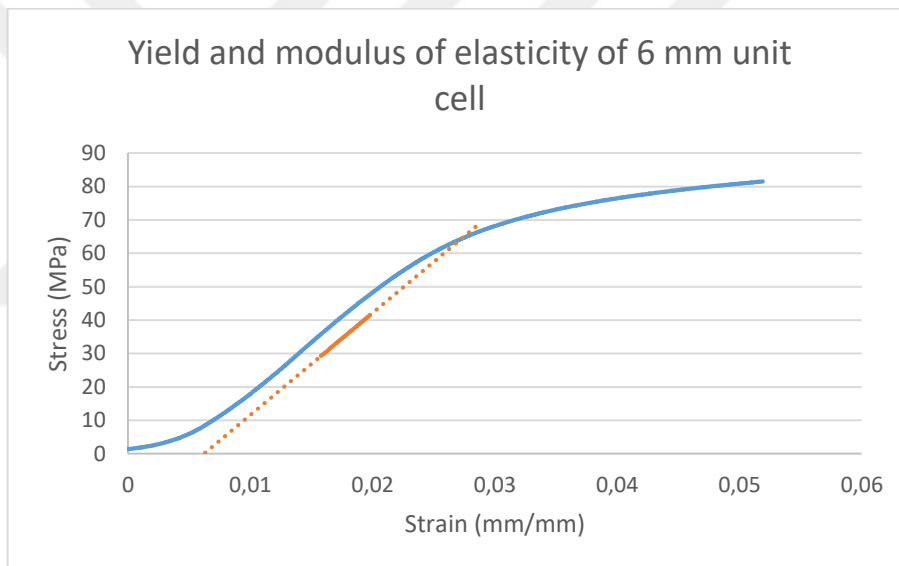


**Figure 4.51** : Yield and modulus of elasticity of 6 mm unit cell specimen.

**Table 4.2** : Yield stress and Modulus of elasticity for each unit cell size specimen.

Unit cell size (mm)	Yield stress (MPa)	Modulus of elasticity (GPa)
6	67.3	2.902+-0.15
8	60.1	3.043+-0.1
12	51.4	2.77+-0.1

Equation 4.2 and Equation 4.3 were proposed by Ashby *et al.* to empirically interpret the relationship between modulus of elasticity, compressive yield strength and the relative density of cellular structures:

$$\frac{E_{latt.}}{E_{sol.}} = C_1 \left( \frac{\rho_{latt.}}{\rho_{sol.}} \right)^n \quad (4.2)$$

$$\frac{\sigma_{pl. latt.}}{\sigma_{y sol.}} = C_5 \left( \frac{\rho_{latt.}}{\rho_{sol.}} \right)^m \quad (4.3)$$

Prefactors  $C_1$  and  $C_5$  represents the geometry of the structures and were found to be in between the range 0.1 to 4.0 and 0.1 to 1, respectively. Exponentials  $n$  and  $m$  are defined to be  $\sim 2$  and  $\sim 1.5$ . These equations and value ranges are exclusive for bending dominated lattice structures such as DG (Gibson, L. J., Ashby, 1997; I. Maskery, Aboulkhair, et al., 2017; I. Maskery, Sturm, et al., 2017; I Maskery et al., 2016).

$\sigma_{y sol.}$ ,  $\rho_{sol.}$  and  $E_{sol.}$  values are assigned as 460 MPa, 8.98 g/cm<sup>3</sup> and 232 GPa. Once the  $n$  and  $m$  values are set to be constants as 2 and 1.5 respectively and remaining variables are used as is by the test results, resulting  $C_1$  and  $C_5$  values can be found in Table 4.3.

**Table 4.3 :**  $C_1$  and  $C_5$  values.

Unit cell size (mm)	C1 Value	C5 value
12	0.25	1.10
8	0.25	1.20
6	0.21	1.23

Found  $C_1$  values are all lies under the expected interval, however  $C_5$  value is off the upper boundary 1.0.

## 5. CONCLUSION

- Modelling approach for basic surface modelling in Unigraphics 12 is tried and resulting geometry is found to be incorrect.
- By using the theoretical formula for gyroid surface model, surface is generated in Matlab and exported in triangulated format successfully.
- For obtaining 20% volume fraction, empirical formula is documented. This formula can be used for designing double gyroid unit cells with varying sizes and wall thicknesses while keeping the volume fraction the same.
- There is a difference found in between the weights of modelled and manufactured specimens. It is assumed that the difference is mainly caused by the wall thickness. It is observed that during manufacturing, specimens are built with a larger wall thickness. The differences are found to be directly proportional to surface area change in different unit cell size specimens.
- Differently offsetted DG models which have decreased wall thickness is modeled to compensate the weight difference for each specific unit cell size specimens.
- Using the offsetted models, specimens with 6, 8 and 12 mm unit cell sizes are successfully manufactured with the volume fractions of 22%, 23% and 24%; respectively.
- Overhang regions in double gyroid model is found to be challenging to build.
- Build defects in overhang areas are identified. In 3 and 4 mm unit cell size specimens, smaller unit cell size had large dropped down regions especially in overhang areas.
- In 6, 8 and 12 mm unit cell sizes, material integrity is found to become worse as the unit cell size increases. Cause of the worsening is explained by the non-supported area increment in bigger unit cell sizes.
- In 12 mm unit cell specimen, open to surface void regions are examined in the most overhang areas.

- In all unit cell size specimens, near the surface voids are interpreted as lack of fusions in overhanging regions caused by the gravity acting on the melt pool.
- In superimposed micro 3d scanned surface models, it is observed that 6, 8 and 12 mm unit cell size specimens experienced distortion. It is concluded that the distortion is mainly caused by the residual stresses which occurred during the manufacturing.
- It is seen in the scanned surface data that 12 mm unit cell size specimen is the worse by the means of overhang regions. Bumps with significant sizes are observed in the worst overhanging regions.
- Overhang regions has an effect on the upper surface in their region. In scanned surfaces, it is observed that as the unit cell size becomes larger, misalignment in the upper surface profile in the overhang regions becomes larger.
- Comparing the cut-up images and scanned surface models, it is concluded that in the overhang regions voids mainly caused by lack of fusion are existent.
- SEM micrographs show that in the up facing surfaces of 12 mm unit cell size specimens, there are dropped down defects in between the layers contour laser passes in the forms of voids. In these void defects, unmelted and partially sintered powder particles are observed. Position of these void regions in the surface are coherent with the previous findings about the misalignment of the upper surfaces in overhang regions.
- Effects of thermal distortion and sticking out sharp corners of specimens have postponed the stress-strain curves
- In the resulting stress-strain curves of compression tests on specimens, each repetitive curve showed excellent overlapping until the ultimate stress value. After the ultimate stress is reached, curves followed a similar but more scattered path. Increment in the scattering of the curves are interpreted as the effect of randomness of disintegration of the structure under higher strain ratios.
- All the resulting stress-strain curves showed an elastic-plastic compression curve characteristic since stress level plateaued without any sharp and repetitive changes.
- The area under the stress-strain curve is calculated up to the densification strain value and normalized by the volume of solid material in each specimen to

obtain energy absorption value per volume. 6, 8 and 12 mm unit cell specimens are able to absorb 112, 116 and 124 MJ/m<sup>3</sup> of energy respectively, prior to densification. It is concluded that bigger unit cell size results in better energy absorption characteristics.

- 6, 8 and 12 mm unit cell size specimens yielded in 67.3, 60.3 and 51.4 MPa stress values. Smaller unit cell sizes yield in higher values than larger unit cell sizes.
- Densification started in 6, 8 and 12 mm unit cell size specimens at 35%, 41% and 50% strain ratios, respectively. Densification strain increases as the unit cell size becomes larger.
- In the video images of the compression testing, it is observed that the cracks propagate after the ultimate stress value is reached. After that point, stress levels start descending and propagation of the cracks are visible through the images.
- It has been observed that the cracks initiate from the down facing surfaces and propagates through the upper face and inner regions as the strain ratio increases. Low surface quality is found to be the reason of crack initiation.



## REFERENCES

- A, P. T. R. S. (2006). The properties of foams and lattices, 15–30. <https://doi.org/10.1098/rsta.2005.1678>
- Abu Al-Rub, Rashid Kamel, Al-Ketan, O. G. (2016). Catalytic Converter Substrates Comprising Triply Periodic Minimal Surfaces.
- Abueidda, D. W., Bakir, M., Al-rub, R. K. A., Bergström, J. S., Sobh, N. A., & Jasiuk, I. (2017). Mechanical properties of 3D printed polymeric cellular materials with triply periodic minimal surface architectures. *Materials & Design*, 122, 255–267. <https://doi.org/10.1016/j.matdes.2017.03.018>
- Abueidda, D. W., Jasiuk, I., & Sobh, N. A. (2018). Acoustic band gaps and elastic stiffness of PMMA cellular solids based on triply periodic minimal surfaces. *Materials & Design*. <https://doi.org/10.1016/j.matdes.2018.02.032>
- Adedeji, A. (2013). *Topology Optimization for Additive Manufacturing*. SFF Symposium 2011.
- Al-ketan, O., Rezgui, R., Rowshan, R., Du, H., Fang, N. X., & Al-rub, R. K. A. (2018). Microarchitected Stretching-Dominated Mechanical Metamaterials with Minimal Surface Topologies, 1800029, 1–15. <https://doi.org/10.1002/adem.201800029>
- Al-ketan, O., Rowshan, R., & Al-rub, R. K. A. (2018). Topology-mechanical property relationship of 3D printed strut , skeletal , and sheet based periodic metallic cellular materials. *Additive Manufacturing*, 19, 167–183. <https://doi.org/10.1016/j.addma.2017.12.006>
- Al-Saedi, D. S. J., Masood, S. H., Faizan-Ur-Rab, M., Alomarah, A., & Ponnusamy, P. (2018). Mechanical properties and energy absorption capability of functionally graded F2BCC lattice fabricated by SLM. *Materials and Design*, 144, 32–44. <https://doi.org/10.1016/j.matdes.2018.01.059>
- Almsherqi, Z., Margadant, F., & Deng, Y. (2012). A look through “lens” cubic mitochondria. *Interface Focus*, 2(5), 539–545. <https://doi.org/10.1098/rsfs.2011.0120>
- Apeleo Zubiri, B., Kelly, S. T., Schröder-Turk, G. E., Klatt, M. A., Fischer, M. G., Spiecker, E., Steiner, U. (2017). Butterfly gyroid nanostructures as a time-frozen glimpse of intracellular membrane development. *Science Advances*, 3(4), e1603119. <https://doi.org/10.1126/sciadv.1603119>
- Axel S. Herrmann, Pierre C. Zahlen, I. Z. (2005). Sandwich Structures Technology in Commercial Aviation, 13–26.
- Bauer, J., Meza, L. R., Schaedler, T. A., Schwaiger, R., Zheng, X., & Valdevit, L. (2017). Nanolattices: An Emerging Class of Mechanical Metamaterials, 1701850, 1–26. <https://doi.org/10.1002/adma.201701850>

- Beharic, A., Rodriguez Egui, R., & Yang, L.** (2018). Drop-weight impact characteristics of additively manufactured sandwich structures with different cellular designs. *Materials and Design*, *145*, 122–134. <https://doi.org/10.1016/j.matdes.2018.02.066>
- Bonacuse, P. J.** (2016). Elevated Temperature Axial and Torsional Fatigue Behavior of, *117*.
- Chen, H., & Thornton, K.** (2009). Multifunctionality of three-dimensional self-assembled composite structure. *Scripta Materialia*, *61*(1), 52–55. <https://doi.org/10.1016/j.scriptamat.2009.03.006>
- Chen, L., Zhang, J., Du, B., Zhou, H., Liu, H., Guo, Y., Fang, D.** (2018). Dynamic crushing behavior and energy absorption of graded lattice cylindrical structure under axial impact load. *Thin-Walled Structures*, *127*(August 2017), 333–343. <https://doi.org/10.1016/j.tws.2017.10.048>
- Choy, S. Y., Sun, C. N., Leong, K. F., & Wei, J.** (2017). Compressive properties of functionally graded lattice structures manufactured by selective laser melting. *Materials and Design*, *131*(March), 112–120. <https://doi.org/10.1016/j.matdes.2017.06.006>
- Delpero, T., Bergamini, A., Ermanni, P., & Kochmann, D. M.** (2014). 3D Auxetic Microlattices with Independently Controllable Acoustic Band Gaps and Quasi-Static Elastic Moduli, (4), 357–363. <https://doi.org/10.1002/adem.201300264>
- Dieler, C., Schröder-Turk, G. E., Winter, B., Spiecker, E., Butz, B., & Mecke, K.** (2015). Coexistence of both gyroid chiralities in individual butterfly wing scales of *Callophrys rubi*. *Proceedings of the National Academy of Sciences*, *112*(42), 12911–12916. <https://doi.org/10.1073/pnas.1511354112>
- Driessen, A. M.** (2016). Overhang constraint in topology optimization for additive manufacturing: a density gradient based approach, 1–85. Retrieved from <https://repository.tudelft.nl/islandora/object/uuid:f95235fc-4e81-48d2-9e2b-ba03d3c734d5%0Ahttp://repository.tudelft.nl/islandora/object/uuid%3Af95235fc-4e81-48d2-9e2b-ba03d3c734d5?collection=education>
- Du, Y., Li, H., Luo, Z., & Tian, Q.** (2017). Topological design optimization of lattice structures to maximize shear stiffness. *Advances in Engineering Software*, *112*, 211–221. <https://doi.org/10.1016/j.advengsoft.2017.04.011>
- Dumas, M., Terriault, P., & Brailovski, V.** (2017). Modelling and characterization of a porosity graded lattice structure for additively manufactured biomaterials. *Materials and Design*, *121*, 383–392. <https://doi.org/10.1016/j.matdes.2017.02.021>
- Farid, S., Shirazi, S., Gharekhani, S., & Mehrali, M.** (n.d.). A review on powder-based additive manufacturing for tissue engineering : selective laser sintering and inkjet 3D printing. *Science and Technology of Advanced Materials*, *16*(3), 1–20. <https://doi.org/10.1088/1468-6996/16/3/033502>
- Ferro, C. G., Varetti, S., De Pasquale, G., & Maggiore, P.** (2018). Lattice structured impact absorber with embedded anti-icing system for aircraft wings fabricated with additive SLM process. *Materials Today Communications*, *15*(February), 185–189. <https://doi.org/10.1016/j.mtcomm.2018.03.007>

- Fleck, N. A., Deshpande, V. S., & Ashby, M. F.** (2010). Micro-architected materials: Past, present and future. *Proceedings of the Royal Society A: Mathematical, Physical and Engineering Sciences*, 466(2121), 2495–2516. <https://doi.org/10.1098/rspa.2010.0215>
- Frazier, W. E.** (2014). Metal Additive Manufacturing : A Review, 23(June), 1917–1928. <https://doi.org/10.1007/s11665-014-0958-z>
- Galusha, J. W., Richey, L. R., Gardner, J. S., Cha, J. N., & Bartl, M. H.** (2020). Discovery of a diamond-based photonic crystal structure in beetle scales, 2–5. <https://doi.org/10.1103/PhysRevE.77.050904>
- Gao, W., Zhang, Y., Ramanujan, D., Ramani, K., Chen, Y., Williams, C. B., ... Zavattieri, P. D.** (2015). Computer-Aided Design The status , challenges , and future of additive manufacturing in engineering. *Computer-Aided Design*, 69, 65–89. <https://doi.org/10.1016/j.cad.2015.04.001>
- Gaynor, A. T.** (2015). Topology Optimization Algorithms for Additive Manufacturing. *The Johns Hopkins University*, 188.
- Giannitelli, S. M., Accoto, D., Trombetta, M., & Rainer, A.** (2013). Current trends in the design of scaffolds for computer-aided tissue engineering. *ACTA BIOMATERIALIA*. <https://doi.org/10.1016/j.actbio.2013.10.024>
- Gibson, L. J., Ashby, M. F.** (1997). *Cellular Solids Structure and Properties* (Second Edi). Cambridge Solid State Science Series.
- Gümrük, R., Mines, R. A. W., & Karadeniz, S.** (2013). Mechanical behaviours of stainless steel micro-lattice structures under different loading conditions. *Materials Science & Engineering A*, 586, 392–406. <https://doi.org/10.1016/j.msea.2013.07.070>
- Han, S. C., Choi, J. M., Liu, G., & Kang, K.** (2017). A microscopic shell structure with schwarz's D-Surface. *Scientific Reports*, 7(1), 1–8. <https://doi.org/10.1038/s41598-017-13618-3>
- Han, S. C., Lee, J. W., & Kang, K.** (2015). COMMUNICATION A New Type of Low Density Material : Shellular, 5506–5511. <https://doi.org/10.1002/adma.201501546>
- Hanzl, P., Zetková, I., & Daňa, M.** (2017). Advanced lattice support structures for metal additive manufacturing. *Manufacturing Technology*, 17(6), 853–857. <https://doi.org/10.1016/j.jmatprotec.2013.01.020>
- Harris, J. A., Winter, R. E., & McShane, G. J.** (2017). Impact response of additively manufactured metallic hybrid lattice materials. *International Journal of Impact Engineering*, 104, 177–191. <https://doi.org/10.1016/j.ijimpeng.2017.02.007>
- Herzog, D., Seyda, V., Wycisk, E., & Emmelmann, C.** (2016). Additive manufacturing of metals. *Acta Materialia*, 117, 371–392. <https://doi.org/10.1016/j.actamat.2016.07.019>
- Jasiuk, I., Abueidda, D. W., Kozuch, C., Pang, S., Su, F. Y., & Mckittrick, J.** (2018). An Overview on Additive Manufacturing of Polymers. *JOM*. <https://doi.org/10.1007/s11837-017-2730-y>

- Jung, Y., & Torquato, S.** (2005). Fluid permeabilities of triply periodic minimal surfaces, 1–8. <https://doi.org/10.1103/PhysRevE.72.056319>
- Kadkhodapour, J.** (2016). Additive manufacturing and mechanical characterization of graded porosity scaffolds designed based on triply periodic minimal surface architectures. *Journal of the Mechanical Behavior of Biomedical Materials*. <https://doi.org/10.1016/j.jmbbm.2016.05.027>
- Kao, Y. T., Amin, A. R., Payne, N., Wang, J., & Tai, B. L.** (2018). Low-velocity impact response of 3D-printed lattice structure with foam reinforcement. *Composite Structures*, *192*(February), 93–100. <https://doi.org/10.1016/j.compstruct.2018.02.042>
- Kapfer, S. C., Hyde, S. T., Mecke, K., Arns, C. H., & Schröder-turk, G. E.** (2011). Minimal surface scaffold designs for tissue engineering. *Biomaterials*, *32*(29), 6875–6882. <https://doi.org/10.1016/j.biomaterials.2011.06.012>
- Khan, K. A., & Al-rub, R. K. A.** (2017). Time Dependent response of Architected Neovius Foams. *International Journal of Mechanical Sciences*. <https://doi.org/10.1016/j.ijmecsci.2017.03.017>
- Khan, K. A., & Al-rub, R. K. A.** (2018). Viscoelastic properties of architected foams based on the Schoen IWP triply periodic minimal surface Viscoelastic properties of architected foams based on the Schoen. *Mechanics of Advanced Materials and Structures*, *0*(0), 1–14. <https://doi.org/10.1080/15376494.2018.1538470>
- Khan, K. A., Al-rub, R. K. A., & Asce, M.** (2018). Modeling Time and Frequency Domain Viscoelastic Behavior of Architected Foams, *144*(6), 1–15. [https://doi.org/10.1061/\(ASCE\)EM.1943-7889.0001448](https://doi.org/10.1061/(ASCE)EM.1943-7889.0001448).
- Klarstrom, D. L.** (1993). Wrought Cobalt-Base Superalloys, *2*(August), 523–530.
- Lee, D., Khan, K. A., & Jasiuk, I.** (2016). Effective conductivities and elastic moduli of novel foams with triply periodic minimal surfaces. *Mechanics of Materials*. <https://doi.org/10.1016/j.mechmat.2016.01.004>
- Lee, M. G., Lee, J. W., Han, S. C., & Kang, K.** (2016). Mechanical analyses of “Shellular” , an ultralow-density material. *Acta Materialia*, *103*, 595–607. <https://doi.org/10.1016/j.actamat.2015.10.040>
- Lee, W., Kang, D., Song, J., Moon, J. H., & Kim, D.** (2016). Controlled Unusual Stiffness of Mechanical Metamaterials. *Nature Publishing Group*, (December 2015), 1–7. <https://doi.org/10.1038/srep20312>
- Li, D., Liao, W., Dai, N., Dong, G., Tang, Y., & Xie, Y. M.** (2018). Optimal design and modeling of gyroid-based functionally graded cellular structures for additive manufacturing. *Computer-Aided Design*. <https://doi.org/10.1016/j.cad.2018.06.003>
- Luzzati, V., Spegt, P. A.** (1967). Polymorphism of Lipids. *Nature Publishing Group*.
- Maskery, I., Aboulkhair, N. T., Aremu, A. O., Tuck, C. J., & Ashcroft, I. A.** (2017). Compressive failure modes and energy absorption in additively manufactured double gyroid lattices. *Additive Manufacturing*, *16*, 24–29. <https://doi.org/10.1016/j.addma.2017.04.003>

- Maskery, I., Aboulkhair, N. T., Aremu, A. O., Tuck, C. J., Ashcroft, I. A., Wildman, R. D., & Hague, R. J. M.** (2016). mechanical property evaluation of graded density Al-Si10-Mg lattice structures manufactured by selective laser melting. *Materials Science & Engineering A*, 670, 264–274. <https://doi.org/10.1016/j.msea.2016.06.013>
- Maskery, I., Hussey, A., Panesar, A., Aremu, A., Tuck, C., Ashcroft, I., & Hague, R.** (2016). An investigation into reinforced and functionally graded lattice structures. <https://doi.org/10.1177/0021955X16639035>
- Maskery, I., Sturm, L., Aremu, A. O., Panesar, A., Williams, C. B., Tuck, C. J., ... Hague, R. J. M.** (2017). Insights into the mechanical properties of several triply periodic minimal surface lattice structures made by polymer additive manufacturing. *Polymer (United Kingdom)*. <https://doi.org/10.1016/j.polymer.2017.11.049>
- McMillan, M., Jurg, M., Leary, M., & Brandt, M.** (2015). Programmatic Lattice Generation for Additive Manufacture. *Procedia Technology*, 20(July), 178–184. <https://doi.org/10.1016/j.protcy.2015.07.029>
- Melchels, F. P. W., Bertoldi, K., Gabbriellini, R., Velders, A. H., Feijen, J., & Grijpma, D. W.** (2010). Mathematically defined tissue engineering scaffold architectures prepared by stereolithography. *Biomaterials*, 31(27), 6909–6916. <https://doi.org/10.1016/j.biomaterials.2010.05.068>
- Michielsen, K., & Stavenga, D. G.** (2008). Gyroid cuticular structures in butterfly wing scales: Biological photonic crystals. *Journal of the Royal Society Interface*, 5(18), 85–94. <https://doi.org/10.1098/rsif.2007.1065>
- Mohsenizadeh, M., Gasbarri, F., Munther, M., Beheshti, A., & Davami, K.** (2018). Additively-manufactured lightweight Metamaterials for energy absorption. *Materials and Design*, 139, 521–530. <https://doi.org/10.1016/j.matdes.2017.11.037>
- Monkova, K., Monka, P., Zetkova, I., Hanzl, P., & Mandulak, D.** (2017). Three Approaches to the Gyroid Structure Modelling as a Base of Lightweight Component Produced by Additive Technology, (Cmsam), 124–129.
- Odabasi, A., N. Unlu, G.Goller, E.S. Kayali, M. N. E.** (2013). Materials Science & Engineering A Assessment of the effects of heat input on microstructure and mechanical properties in laser beam welded Haynes 188 undermatched joints, 559, 731–741. <https://doi.org/10.1016/j.msea.2012.09.017>
- Panesar, A., Abdi, M., Hickman, D., & Ashcroft, I.** (2018). Strategies for functionally graded lattice structures derived using topology optimisation for Additive Manufacturing. *Additive Manufacturing*, 19, 81–94. <https://doi.org/10.1016/j.addma.2017.11.008>
- Park, J., & Lee, J.** (2017). Unusually high ratio of shear modulus to Young ' s modulus in a nano-structured gyroid metamaterial. *Scientific Reports*, (August), 1–8. <https://doi.org/10.1038/s41598-017-10978-8>
- Rae, K. B. S., Castelli, M. G., & Ellis, J. R.** (1995). On The Low Cycle Fatigue Deformation Of Haynes 188 Superalloy In The Dynamic Strain Aging Regime, 33(6), 1005–1012.

- Rahman Rashid, R. A., Mallavarapu, J., Palanisamy, S., & Masood, S. H.** (2017). A comparative study of flexural properties of additively manufactured aluminium lattice structures. *Materials Today: Proceedings*, 4(8), 8597–8604. <https://doi.org/10.1016/j.matpr.2017.07.207>
- Rashed, M. G., Ashraf, M., Mines, R. A. W., & Hazell, P. J.** (2016). Metallic Microlattice Materials: A current state of the art on manufacturing, mechanical properties and applications. *JMADE*. <https://doi.org/10.1016/j.matdes.2016.01.146>
- Rashid Abu Al-Rub, O. A.-K.** (2017). Interpenetrating Phase Composite Structures Including Triply Periodic Minimal Surfaces and Methods of Forming the Same.
- Rossi, M.** (2017). Form is matter. New surface structures by digital design tools.
- Rothman, M. F., Zordan, R. D., Muzyka, D. R.** (1984). Role of Refractory Elements in Cobalt-Base Alloys. In *Role of Refractory Elements in Cobalt-Base Alloys*. Rio de Janeiro.
- Rupani, S. V.** (2017). Design , Modelling and Manufacturing aspects of Honeycomb Sandwich Structures : A Review, (May). <https://doi.org/10.1712/ijdsr.17013>
- Ryan, R. C.** (2014). Minimal Surface Area Mass and Heat Transfer Packing.
- Schoen, A. H.** (1970). *Triply Periodic Minimal Surface without Self-Intersections*. Cambridge.
- Schoen, A. H.** (2012). Reflections concerning triply-periodic minimal surfaces, (May), 658–668.
- Science, M., Issn, F., & Publications, T. T.** (2007). Thermal Applications of Cellular Lattice Structures Haydn N.G. Wadley, 242–247. <https://doi.org/10.4028/www.scientific.net/MSF.539-543.242>
- Seifi, H., Rezaee Javan, A., Xu, S., Zhao, Y., & Xie, Y. M.** (2018). Design optimization and additive manufacturing of nodes in gridshell structures. *Engineering Structures*, 160(June 2017), 161–170. <https://doi.org/10.1016/j.engstruct.2018.01.036>
- Slaughter, V. B.** (2011). Method of Using Minimal Surfaces and Minimal skeletons to Make Heat Exchanger Components.
- Stanković, T., Mueller, J., & Shea, K.** (2017). The effect of anisotropy on the optimization of additively manufactured lattice structures. *Additive Manufacturing*, 17, 67–76. <https://doi.org/10.1016/j.addma.2017.07.004>
- Sun, F., Lai, C., & Fan, H.** (2016). In-plane compression behavior and energy absorption of hierarchical triangular lattice structures. *Materials and Design*, 100, 280–290. <https://doi.org/10.1016/j.matdes.2016.03.023>
- Tang, Y., Kurtz, A., & Zhao, Y. F.** (2015). Bidirectional Evolutionary Structural Optimization (BESO) based design method for lattice structure to be fabricated by additive manufacturing. *CAD Computer Aided Design*, 69, 91–101. <https://doi.org/10.1016/j.cad.2015.06.001>

- Tanlak, N., De Lange, D. F., & Van Paepegem, W.** (2017). Numerical prediction of the printable density range of lattice structures for additive manufacturing. *Materials and Design*, *133*, 549–558. <https://doi.org/10.1016/j.matdes.2017.08.007>
- Terriault, P., & Brailovski, V.** (2018). Modeling and simulation of large, conformal, porosity-graded and lightweight lattice structures made by additive manufacturing. *Finite Elements in Analysis and Design*, *138*(August 2017), 1–11. <https://doi.org/10.1016/j.finel.2017.09.005>
- Torquato, S., Donev, A., & A, P. R. S. L.** (2004). Minimal surfaces and multifunctionality, 1849–1856. <https://doi.org/10.1098/rspa.2003.1269>
- Ullah, I., Elambasseril, J., Brandt, M., & Feih, S.** (2014). Performance of bio-inspired Kagome truss core structures under compression and shear loading. *COMPOSITE STRUCTURE*, *118*, 294–302. <https://doi.org/10.1016/j.compstruct.2014.07.036>
- Vaezi, M., Seitz, H., & Yang, S.** (2013). A review on 3D micro-additive manufacturing technologies, 1721–1754. <https://doi.org/10.1007/s00170-012-4605-2>
- Wadley, H. N. G., Dharmasena, K. P., He, M. Y., McMeeking, R. M., Evans, A. G., Bui-Thanh, T., & Radovitzky, R.** (2010). An active concept for limiting injuries caused by air blasts. *International Journal of Impact Engineering*, *37*(3), 317–323. <https://doi.org/10.1016/j.ijimpeng.2009.06.006>
- Wadley, H. N. G., & Queheillalt, D. T.** (2009). Thermal Applications of Cellular Lattice Structures. *Materials Science Forum*, *539–543*, 242–247. <https://doi.org/10.4028/www.scientific.net/msf.539-543.242>
- Wang, L., Lau, J., Thomas, E. L., & Boyce, M. C.** (2011). Co-Continuous Composite Materials for Stiffness , Strength , and Energy Dissipation, 1524–1529. <https://doi.org/10.1002/adma.201003956>
- Wang, Y., Zhang, L., Daynes, S., Zhang, H., Feih, S., & Wang, M. Y.** (2018). Design of graded lattice structure with optimized mesostructures for additive manufacturing. *Materials and Design*, *142*, 114–123. <https://doi.org/10.1016/j.matdes.2018.01.011>
- Wen, T., Tian, J., & Lu, T. J.** (2006). Forced convection in metallic honeycomb structures, *49*, 3313–3324. <https://doi.org/10.1016/j.ijheatmasstransfer.2006.03.024>
- Werner, M., & Pieranski, P.** (2017). Mechanical properties of ceramic structures based on Triply Periodic Minimal Surface ( TPMS ) processed by 3D printing  
Mechanical properties of ceramic structures based on Triply Periodic Minimal Surface ( TPMS ) processed by 3D printing.
- Xiong, B. J., Mines, R., Ghosh, R., Vaziri, A., Ma, L., Ohrndorf, A., Christ, P. H.** (2015). Advanced Micro-Lattice Materials \*\*, 1–12. <https://doi.org/10.1002/adem.201400471>

- Yan, C., Hao, L., Hussein, A., Young, P., & Huang, J.** (2015). Microstructure and mechanical properties of aluminium alloy cellular lattice structures manufactured by direct metal laser sintering. *Materials Science & Engineering A*, 628, 238–246. <https://doi.org/10.1016/j.msea.2015.01.063>
- Yang, S., Lee, H. G., & Kim, J.** (2010). A phase-field approach for minimizing the area of triply periodic surfaces with volume constraint. *Computer Physics Communications*, 181(6), 1037–1046. <https://doi.org/10.1016/j.cpc.2010.02.010>
- Yilbas, B. S., & Akthar, S.** (2011). Laser welding of Haynes 188 alloy sheet : thermal stress analysis, 115–124. <https://doi.org/10.1007/s00170-011-3181-1>
- Yoo, D.** (2014). Advanced Porous Scaffold Design using Multi-Void Triply Periodic Minimal Surface Models with High Surface Area to Volume Ratios, 15(8), 1657–1666. <https://doi.org/10.1007/s12541-014-0516-5>
- Zargarian, A., Esfahanian, M., Kadkhodapour, J., & Ziaei-Rad, S.** (2016). Numerical simulation of the fatigue behavior of additive manufactured titanium porous lattice structures. *Materials Science and Engineering C*, 60, 339–347. <https://doi.org/10.1016/j.msec.2015.11.054>
- Zhang, A. L., Feih, S., & Daynes, S.** (2018). Energy absorption characteristics of metallic triply periodic minimal surface sheet structures under compressive loading. *Additive Manufacturing*. <https://doi.org/10.1016/j.addma.2018.08.007>
- Url-1** <<https://www.indiamart.com>>, date retrieved 12.03.2019.
- Url-2** <<http://www.coleoptera-atlas.com>>, date retrieved 03.03.2019.
- Url-3** <<http://www.icons101.com>>, date retrieved 03.03.2019.
- Url-4** <<https://www.haynesintl.com>>, date retrieved 03.03.2019.
- Url-5** <<http://www.keiththomsonbooks.com>>, date retrieved 05.03.2019.
- Url-6** <<https://www.3ders.org>>, date retrieved 05.03.2019.
- Url-7** <<https://www.ge.com>>, date retrieved 17.03.2019.
- Url-8** <<https://www.tctmagazine.com>>, date retrieved 19.03.2019.
- Url-9** <<http://trends.directindustry.com>>, date retrieved 19.03.2019.
- Url-10** <<https://www.struers.com>>, date retrieved 20.03.2019.
- Url-11** <<https://www.struers.com>>, date retrieved 20.03.2019.
- Url-12** <<https://www.struers.com>>, date retrieved 20.03.2019.
- Url-13** <<http://www.shimadzu.com.br>>, date retrieved 20.03.2019.
- Url-14** <<https://www.nikonmetrology.com>>, date retrieved 20.03.2019.
- Url-15** <<https://www.alicon.com>>, date retrieved 20.03.2019.

## CURRICULUM VITAE

**Name Surname** : Barış KAVAS  
**Place and Date of Birth** : İstanbul / 15.06.1993  
**E-Mail** : kavasbaris@gmail.com



## EDUCATION

- **Bachelor of Science** : 2011-2016, Istanbul Technical University, Faculty of Chemical and Metallurgical Engineering, Metallurgical and Materials Engineering
- **Master of Science** : 2016-2019, Istanbul Technical University, Faculty of Chemical and Metallurgical Engineering, Materials Engineering

## PROFESSIONAL EXPERIENCE AND REWARDS:

- 2018-Present, General Electric Aviation –Turkey Technology Center., Lead Additive Manufacturing Engineer – Emerging Technologies, Kocaeli, Turkey
  - Turkey Technology Center Young Engineer Award (2018)
- 2016-2018, General Electric Aviation –Turkey Technology Center., Edison Engineering Development Program, Kocaeli, Turkey
  - LM6000 Cold Section Airfoil Design Engineer
  - Airfoils Materials Application Engineer
  - Additive Manufacturing Engineer
- 2015, Helmholtz-Zentrum Geesthacht, Zentrum Für Material, Magnesium Innovation Center, Research Intern, Hamburg, Germany
- 2014-2016, General Electric Aviation –Turkey Technology Center., Additive Manufacturing Intern, Kocaeli, Turkey

## PUBLICATIONS AND PRESENTATIONS:

- **Kavas, B., Yasa E., Sönmez, Ş.**, “Compressive Strength Testing and Characterization of Double Gyroid Lattice Structure Produced by Direct Metal Laser Melting”, 4<sup>th</sup> Workshop on Metal Additive Manufacturing (2019), Leuven, Belgium.